ABSTRACT

Title of Dissertation: Development and Application of Solid-Liquid Lattice Boltzmann Model for Phase Change Material in Heat Exchanger

Dongyu Chen
Doctor of Philosophy, 2022

Dissertation Directed by: Professor Reinhard Radermacher
Professor Amir Riaz
Department of Mechanical Engineering

Phase change materials (PCMs) are widely used in thermal energy storage systems, as they can absorb and release a large amount of heat during the phase change process. Numerical simulations can be used for parametric studies and analysis of the thermal performance of the PCM heat exchanger (HX) to produce an optimal design. Among various numerical methods, the lattice Boltzmann method (LBM), a mesoscopic approach that considers the molecular interactions at relatively low computation costs, offers certain key advantages in simulating the phase change process compared with the conventional Navier-Stokes-based (NS-based) methods. Moreover, LBM is ideal for parallel computing, by which numerical analysis can be efficiently performed. Therefore, a comprehensive solid-liquid phase change model is developed based on LBM which is capable of accurately and efficiently simulating the process of convective PCM phase change with and without porous media in both Cartesian and axisymmetric domains. Double distribution functions (DDF)

coupled with a multi-relaxation-time (MRT) scheme are utilized in the LBM formulation for the simulation of the fluid flow and the temperature field. A differential scanning calorimetry (DSC) correlated equation is applied in LBM to model enthalpy, by which the solid-liquid interface can be automatically tracked. The source term in the MRT scheme is modified to eliminate numerical errors at high Rayleigh numbers. Moreover, the conjugate thermal model is adopted for the consideration of heat transfer fluid (HTF) flow and conducting fins. The new model is verified and validated by various case studies. The results indicate that the new model can successfully predict the process of PCM phase change with errors confined to less than 10%. Parametric studies are then performed using the validated model to quantitatively evaluate the effect of convection on PCM melting, from which the acceleration rates (a_c) of PCM melting and the threshold Rayleigh numbers (Ra_{dc}) at various aspect ratios are defined and quantified. Furthermore, PCM melting in porous cylindrical HX is also investigated. The results indicate that the acceleration of melting could reach 95% compared to that in pure PCM at 60% energy storage. Moreover, the negative effect of uneven temperature distributions on thermal performance of the HX caused by convection is quantified and analyzed. A modified cylindrical HX that offsets this negative effect by varying the geometry is also evaluated. The results indicate that the modified geometry can successfully enhance heat transfer and balance the uneven temperature distributions.

Development and Application of Solid-Liquid Lattice Boltzmann Model for Phase Change Material in Heat Exchanger

by

Dongyu Chen

Dissertation submitted to the Faculty of the Graduate School of the
University of Maryland, College Park in partial fulfillment
of the requirements for the degree of
Doctor of Philosophy
2022

Advisory Committee:
Professor Reinhard Radermacher, Chair/Advisor
Professor Amir Riaz, Co-Advisor
Professor Vikrant C. Aute
Professor Jelena Srebric
Professor Siddhartha Das
Professor Bao Yang
Professor Peter B. Sunderland

Acknowledgments

I owe my gratitude to all the people who have offered me invaluable help in my Ph.D. study, which has made this dissertation possible.

Firstly, I would like to thank my advisor, Professor Reinhard Radermacher, for providing me the opportunity to work and study with many outstanding scholars over the past six years at CEEE. His high-level insights always inspire me and encourage me to explore deeper research areas. Thanks to his trust and encouragement when I was finding research directions, I was able to propose and then complete my Ph.D. dissertation.

I would also like to thank my co-advisors, Professor Amir Riaz and Professor Vikrant C. Aute, for offering me their professional guidance, expert knowledge, timely support, and critical computational resources for my research, without whom, this dissertation would have been lack of solid foundation and practical significance. And sincere thanks are given to my committee members, Professor Jelena Srebric, Professor Siddhartha Das, Professor Bao Yang, and Professor Peter B. Sunderland, for sparing their time reviewing my research work and offering precious suggestions.

Besides, I would like to thank Prof. Yunho Hwang, who offered me the opportunity to work in EEHP group during the first two and a half years of my graduate study. The experience of conducting experiments in the lab is also valuable to me, which is a workout for both my body and mind.

Second, I would like to express my gratitude to Professor Yaling He, for providing me with long-term advice and encouraging me to pursue this Ph.D. degree. And special thanks are due to Dr.Zixiang Tong and Dr.Dong Li, for sharing with me their professional knowledge and invaluable experience accumulated in the practice of programming and computing, which helped me start-off.

I would also like to acknowledge the help and support from my fellows and colleagues, Zhenyuan Mei, Lei Gao, Tianyue Qiu, and Ransisi Huang. I would miss the days that we were together for working, studying and dining. Special thanks are given to Long Huang and his wife, who offered me the accommodations when I first arrived in Maryland, and my senior colleagues, Tao Cao and Xiaojie Lin, who helped me a lot when I initiated my graduate life at CEEE.

Lastly, my deepest thanks are given to my wife, Yiyuan Qiao, for her constant support and understanding, and my dear son, Leon(Keliang) Chen, who was born during my Ph.D. study, the best gift in my life. I would also thank my mother and father, who have always stood by me and guided me through my career. I would have not accomplished this dissertation without their support.

Table of Contents

List of Tables

List of Figures

List of Abbreviations

CO_2	Carbon dioxide
CFD	Computational fluid dynamics
DDF	Double distribution function
DNS	Direct numerical simulation
DPD	Dissipative particle dynamics
DSMC	Direct simulation Monte Carlo
DSC	Differential scanning calorimetry
FDM	Finite difference method
FVM	Finite volume method
FEN	Finite element method
GHG	Greenhouse gas
HX	Heat exchanger
HTF	Heat transfer fluid
HPC	High performance computing
HVAC&R	Heating, ventilation, air conditioning, and refrigeration
LBM	Lattice Boltzmann method
LB	Lattice Boltzmann
LBGK	Lattice BGK
LES	Large eddy simulation
LHTES	Latent heat thermal energy storage
MPI	Message passing interface
MSMPI	Microsoft MPI
MRT	Multi-relaxation-time
MD	Molecular dynamics
MCHX	Microchannel HX
NS-based	Navier-Stokes-based
PCM	Phase change material
PU	Partial unit
RANS	Reynolds-averaged Navier-Stokes
REV	Representative elementary volume
SHTES	Sensible heat thermal energy storage
SRT	Single-relaxation-time

List of Symbols

Scalars

A	aspect ratio
a_c	acceleration rate of PCM melting
b	thickness
C	inertial coefficient
c	lattice speed
c_s	lattice sound speed in flow field
c_{sT}	lattice sound speed in temperature field
c_p	specific heat capacity at constant pressure
d_p	diameter of pores
η	energy storage ratio
f_l	liquid fraction
g	gravitational acceleration
h	enthalpy
K	permeability
k	thermal conductivity
L	characteristic length
L_a	latent heat
N_{fin}	number of fins in HX
P	fluid pressure
T	temperature
T_0	reference temperature
ΔT_{glide}	temperature glide of PCM
t	time
t_{fin}	fin spacing
R	gap of annulus in radius
r_i	inner wall radius of annulus
r_o	outer wall radius of annulus
r_{fin}	fin radius
U	lid velocity in x direction (2D and 3D)
u_c	characteristic velocity
V	lid velocity in y direction (only 3D)
v	kinematic viscosity

x	length in horizontal direction (2D Cartesian)
y	length in vertical direction (2D Cartesian)
r	length in radial direction (2D axisymmetric)
z	length in axial direction (2D axisymmetric)
α	thermal diffusivity
β	thermal expansion coefficient
δ_x	discrete space step in LBM
δ_t	discrete time step in LBM
ϕ	porosity of embedded porous media
ρ	density
τ	relaxation time
ω	weight coefficient
Da	Darcy number
Fo	Fourier number
Ra	Rayleigh number
Ra_{dc}	threshold Rayleigh number
Ste	Stefan number
Pr	Prandtl number
Re	Reynolds number
J	viscosity ratio
λ	thermal diffusivity ratio
θ	dimensionless temperature
Z	dimensionless height

Vectors

$\mathbf{e}$	discrete velocity vector
$\mathbf{F}$	total external force
$\mathbf{F}_v$	external force term in LBM
$\mathbf{F}_m$	external force term of LBM in moment space
$\mathbf{f}$	density distribution functions
$\mathbf{G}$	gravity
$\mathbf{g}$	temperature distribution functions
$\mathbf{H}$	correction term in D2Q5 thermal MRT-LBM
$\mathbf{\Psi}$	source term in D2Q5 thermal MRT-LBM
$\mathbf{m}$	density distribution vector in moment space
$\mathbf{n}$	temperature distribution vector in moment space
$\mathbf{Q}_m$	source term in moment space
$\mathbf{u}$	velocity vector

$\mathbf{v}$	temporal velocity

Matrices

$\mathbf{I}$	identity matrix
$\mathbf{M}$	transition matrix for flow field
$\mathbf{N}$	transition matrix for temperature field
$\mathbf{S}$	relaxation matrix

Subscripts

e	effective value
fin	fin
g	LBM for temperature field
i	ith component in the vector
int	initial
l	liquid PCM
$latent$	latent
pcm	PCM
p, m	porous media
s	solid PCM
$sensible$	sensible
ref	reference value
v	LBM for flow field
x	horizontal direction (2D Cartesian)
y	vertical direction (2D Cartesian)
r	radial direction (2D axisymmetric)
z	axial direction (2D axisymmetric)

Superscripts

eq	equilibrium distribution functions or moment vector
T	transpose of the matrix
$*$	post-collision distribution functions or moment vector
-1	inverse of the matrix

Chapter 1: Introduction

1.1 Motivation

With the rapid growth of the human population and economy, the demand for energy has increased dramatically over the past few decades. The ensuing huge energy consumption results in the massive emission of carbon dioxide (CO_2) and the production of other harmful substances, which contributes to global warming and environmental pollution. The greenhouse gas (GHG) emissions are expected to increase by 50% by 2050, of which mainly 70% comes from the contribution of energy-related CO_2 emissions [13]. In response to these issues, an agreement was adopted by 196 parties (countries) at the 21st United Nations Conference of the Parties in Paris on 12th December 2015, also well-known as the Paris Agreement [14]. The goal of this agreement is to limit global warming to below 2 degrees Celsius, compared to pre-industrial levels. Following the guiding principles of the Paris Agreement, many countries have pledged to achieve carbon neutrality (net-zero CO_2 emissions) by 2050 or 2060 [15]. The United States has set the goal to reduce GHG emissions by 50-52% from 2005 levels by 2030 and achieve net-zero emissions by 2050 according to the Federal Sustainability Plan [16]. China has announced a long-term plan aiming to mitigate carbon emissions by 60-65% and reach peak

emissions by 2030, then achieve carbon neutrality before 2060 [17]. The European Commission has also proposed to reduce the GHS emissions by at least 55% by 2030 and no net emissions of GHG by 2050 [18]. It is obvious that the achievement of those ambitious goals relies on the supporting energy policies, where (1) the shift from fossil fuel to renewable energy, (2) improving energy efficiency, and (3) ensuring energy security are widely emphasized by various countries and districts [19, 20].

Many developed techniques in thermal applications can be adopted to address the issues mentioned above. Among them, the thermal energy storage system is one of the most useful and attractive tools, as it can efficiently store (1) the renewable energy such as solar energy and geothermal energy, (2) the low-grade waste heat, or (3) the electricity at night with low price [19], and then release the stored energy when needed, which can balance the mismatch between energy demand and supply in time, space and intensity dimensions. Therefore, the thermal energy storage system can efficiently utilize renewable energy, recover industrial waste heat, and balance the energy intensity on time scales, which can improve the efficiency and security of the overall energy system.

Generally, there are two types of thermal energy storage systems: sensible heat thermal energy storage (SHTES) system and latent heat thermal energy storage (LHTES) system. LHTES system utilizes phase change material (PCM) to store the energy, which enables the system to absorb and release a large amount of heat with little temperature variation by the phase change process of PCM. Therefore LHTES system has higher energy densities with more stable temperatures during the energy storage process compared with the SHTES system. The PCM heat exchanger (HX)

is the component utilized in the LHTES system to contain PCM and perform heat transfer between the PCM and the working fluid. The performance of the PCM HX directly affects the efficiency of the LHTES system, improving the heat transfer performance of the PCM HX is therefore of primary importance for improving the efficiency of the LHTES system, which consequently benefits the overall energy system.

To better study the PCM HX performance, both experimental and numerical studies are necessary. Numerical studies are relatively more adept at quantitatively analyzing the PCM HX and performing numerous parametric studies that can guide the design and optimization of the PCM HX.

This dissertation focuses on the numerical studies of the PCM HX to provide insights into the physical mechanisms and the basis of the PCM HX design.

1.2 Literature Review

1.2.1 Latent Heat Thermal Energy Storage (LHTES) System

Owing to the features of LHTES mentioned in Section 1.1, LHTES system has been widely applied in many fields such as the building [21, 22], solar energy system [23, 24], heating and cooling system [25, 26], electronic cooling system [27], and heat recovery system [28]. Latent heat storage can be achieved through either solid-liquid phase change, or liquid–gas phase change. Although liquid-gas phase change has higher latent heat than solid-liquid phase change, its application is not realistic as the thermal storage in gas phase requires large volumes or high pressures,

which makes the system complex and impractical [29]. Therefore, solid–liquid phase change is commonly adopted for latent heat storage.

Both experimental and numerical investigations for LHTES system have increased substantially in the past two decades. Most studies have been conducted on the melting or solidification process of the PCM heat exchanger (HX) at the component level [30,31], while a few studies focus on the overall performance at the system level [32–34]. The main differences between these two levels with respect to the numerical analysis of LHTES system are that:

1. The system-level study establishes an entire LHTES system and evaluates the performance of the PCM based on it. Consequently, to be consistent with other parts of the system and the computational efficiency of the entire model, its PCM HX part should be simplified, such as the neglect of the natural convection and the effect of the porous media.

2. The component-level study looks at the PCM HX itself in detail and usually considers the complexity of the thermal flow. Its PCM HX model is usually more detailed and therefore more accurate compared with the model of the HX component in the system-level model.

In this dissertation, simulation is conducted at the component level for solid-liquid LHTES system by using the CFD method to reveal the basic physical mechanisms and evaluate the performance of the PCM HX.

1.2.2 PCM Heat Exchanger (HX)

As introduced in Section 1.1, the PCM HX is the component that transfers heat between the PCM and the working fluid. There are several methods to enhance heat transfer in PCM HX, such as increasing the heat transfer area by fins [35] or capsules [36] and increasing the effective conductivity by porous media, e.g., nanoparticles [37], metal foam [38] and graphite [39]. Unlike nanoparticles which can move with the liquid flow of PCM, metal foam and graphite embedded in PCM HX are fixed structures.

Among those different configurations of the HX, the basic shapes of the HX can be rectangular, cylindrical, spherical or other more complicated shapes. According to the experimental and numerical studies, as well as the practical PCM HX prototypes, the cylindrical container is one of the common shapes [40].

Therefore, the research in this dissertation focuses more on the PCM melting in a cylindrical HX, where the natural convection of the liquid PCM. Moreover, the PCM HX enhanced by fins, embedded porous media and modified geometries are also considered in this dissertation.

1.2.3 Phase Change Material (PCM)

The types of PCM can be categorized as organic, inorganic, and eutectic [21], where organic PCMs can be further divided as fatty acids, paraffin, and non-paraffin [41], while inorganic materials include the salt hydrate and metallics. Different types of PCM behave differently in terms of thermal, kinetic, and chemical properties.

For the PCM used in the LHTES system, high latent heat, high thermal conductivity, good thermal stability, and low weight with compact size are recommended. In that regard, paraffin and fatty acids are widely chosen as the PCM in the HX owing to their high latent heat with stable thermal properties, excellent performance in thermal cycles, and low weight with high compactness. In this dissertation, the PCM properties used in the simulation are mainly based on paraffin wax.

PCM	Melting temperature (°C)	Latent heat (kJ/kg)
RT35	35	157
RT35 HC	35	240
PT37	37	210
Capric acid	36	152

Table 1.1: Selected PCMs for Melting Temperatures between 35 °Cand 37 °C

The melting temperature is one of the key properties of the PCM, which plays an important role in PCM selection for a specific operating condition. For instance, if the PCM HX is used as a condenser in a cooling cycle, the efficiency of the system increases as the melting temperature of the PCM decreases. However, the melting temperature should be at least higher than the ambient temperature for practical use. Thus, the desired melting temperature range of PCM for the condenser is confined, and is recommended to be around 35 to 37 °C. Table 1.1 lists four PCMs that satisfy this operating condition. Among them, the enthalpy equations of RT35, RT35 HC, and PT37 are modeled from differential scanning calorimetry (DSC) test data in this dissertation since they are used in the experiments for the validations. The detailed thermal physical properties for these three PCMs can be found in

Chapter 5.

The thermal physical properties of the PCM in HX can be used to determine the Rayleigh number (Ra), which measures the thermal convection over the thermal conduction in the PCM liquid zone. The definitions of critical dimensionless numbers including Ra are provided in Section 2.7. For the paraffin wax and fatty acids, their thermal properties are very similar and do not vary much among the PCMs at different melting temperatures. Therefore, after reviewing numerous properties for these two substances at different melting temperatures, the properties that are required for calculating the Rayleigh numbers are actually within a certain range, such as the specific heat c_p ($1.41 - 3.26\ kJ/(kg\ K)$), thermal conductivity k ($0.14 - 0.51\ W/(m\ K)$), density ρ ($750 - 1580\ kg/m^3$), fluid viscosity v_l ($1.0 - 9.0\ mm^2/s$) and thermal expansion coefficient β ($0.0001 - 0.02\ K^{-1}$), where the differences between the solid and liquid phases have been considered in those ranges. For the HX with a given size and temperature difference between the inlet temperature of HTF flow and the melting temperature of the PCM, the range of potential Rayleigh numbers can be determined for paraffin wax and fatty acids. Based on the size of the HX and temperature settings studied in this dissertation, such as $R = r_o - r_i$ ($10 - 100\ mm$) and ΔT ($10 - 20$ °C), the Rayleigh numbers of the PCM HX could be roughly between 18 and 1.4×10^8 if choosing radius gap R as the characteristic length, which indicates that natural convection in the PCM HX could be qualitatively very different over the range of Rayleigh numbers covered in this study.

1.2.4 Lattice Boltzmann Method (LBM)

Computational fluid dynamics (CFD) can be divided into three broad categories: macroscopic, mesoscopic, and microscopic approaches. Macroscopic approaches such as the Reynolds-averaged Navier-Stokes (RANS) method, large eddy simulation (LES), and direct numerical simulation (DNS) are based on the assumption of continuum and solve Navier-Stokes (NS) equations to simulate fluid flow. The macroscopic approach is obviously not well suited for the physical problems where molecular interactions are important.

The microscopic approaches such as molecular dynamics (MD), direct simulation Monte Carlo (DSMC), and dissipative particle dynamics (DPD), are developed to simulate the microscale problems where the continuum assumption breaks down [42]. However, the microscopic approaches consider the motion of every molecule, which leads to a massive computational cost. Therefore, the lattice Boltzmann method (LBM), a mesoscopic approach based on the Boltzmann equation, has an advantage as it serves as a bridge to combine microscopic physics with macroscopic properties at a reasonable computation cost. The three categories of the CFD methods are summarized in Table 1.2.

Physical scale	Numerical simulation methods	Theory basis
Macroscopic	RANS, LES and DNS	NS equations
Mesoscopic	LBM	Discrete Boltzmann equation
Microscopic	MD, DSMC and DPD	Particle dynamics

Table 1.2: Numerical Simulation Methods.

Among various numerical methods, LBM is an attractive and promising approach to simulate the fluid flow and heat transfer process. Unlike the conventional CFD method which solves the Navier-Stokes (NS) equations, LBM solves the Boltzmann equations in discrete form. Moreover, LBM is an explicit method of second-order accuracy with the ability to use molecular motions for determining macroscopic properties. Owing to these features, LBM can have several advantages compared with the conventional CFD method in terms of the computation costs, parallel computing, and the multiphase flow with phase change [43].

In this dissertation, the model for PCM HX is developed based on LBM instead of the convection CFD methods.

1.2.5 Numerical Modeling of PCM HX

Generally, the numerical modeling of PCM HX can be deconstructed as one algorithm solving the flow field in the liquid PCM zone, one algorithm solving the temperature field across the entire PCM domain and one algorithm to treat the interface between the solid and liquid. In some conduction-dominated cases, convection can be neglected and thus no algorithm for fluid flow is needed. However, for the common PCM HX, where the Rayleigh number is usually above 10^4, convection should be considered, and thus both flow and temperature field should be modeled.

The modeling of the PCM with respect to energy conservation and transport can be categorized by whether the latent heat is treated as a source term or modeled as variable specific heat capacity. The former approach is named as the enthalpy

method and the latter is called the effective heat capacity method [44]. For the numerical model based on LBM, since the specific heat capacity usually can not be varied in LBM, the most commonly adopted LBM for solid-liquid phase change is based on the enthalpy method, which is denoted as the enthalpy-based LBM.

1.2.5.1 Conventional CFD Model

For conventional CFD methods, they can be characterized by the discretization methods as finite difference method (FDM), finite volume method (FVM), and finite element method (FEM). Each of the methods can be used to simulate the PCM phase change. The simulation can either be conducted through commercial software or from self-developed programming. A detailed summary of the self-developed numerical models can be found in the literature from Al-abidi et al. [44], where most studies simulate the cylindrical HX, and a few of the studies focus on the rectangles and spheres. For the simulation using commercial software, two examples are given below, one in 2D and one in 3D.

Longeon et al. [4] studied the annular PCM storage as shown in Fig. 1.1 both numerically and experimentally, where a 2D axisymmetric model was established using the commercial CFD software Fluent. The results indicated that the charging directions and convection heat transfer together affect the PCM melting front.

Youssef et al. [7] developed a 3D CFD model using ANSYS Fluent software for the PCM HX with spiral-wired tubes as shown in Fig. 1.2 and validated the model with the experimental results.

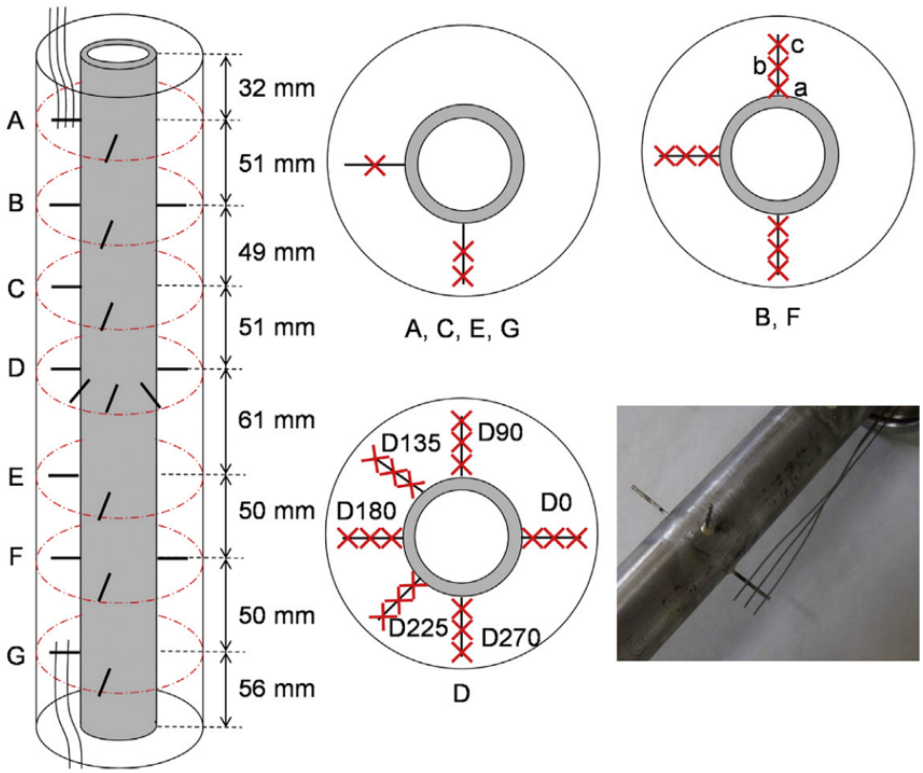

Figure 1.1: Annular PCM HX [4].

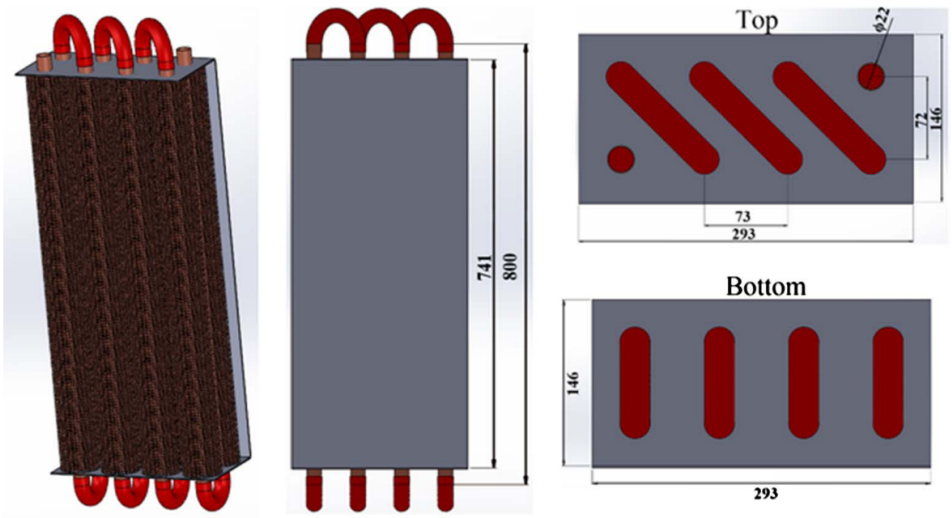

Figure 1.2: PCM HX with spiral-wired tubes [7].

In this dissertation, the numerical results from convectional CFD methods can be utilized to verify the developed lattice Boltzmann model.

1.2.5.2 Solid-Liquid Lattice Boltzmann Model

Over the past two decades, many lattice Boltzmann (LB) models have been developed for solid-liquid phase change. Generally, the existing solid-liquid LBM can be classified into two categories based on the treatments of the phase interface [9]: (1) phase-field LBM, which distinguishes the phase interface by introducing an order parameter [45,46], and (2) enthalpy-based LBM, which distinguishes the phase interface by solving the liquid fraction [47–49]. For the PCM phase change problem where the microscopic effects and solid-phase motion can be neglected, enthalpy-based LBM is commonly adopted due to its simplicity and effectiveness [50]. As for the consideration of the porous media, it can be either modeled at the pore-scale or the representative elementary volume (REV) scale. The REV-scale approach ignores the detailed geometry of the porous media and therefore is unable to solve the detailed local information of the flow and heat transfer in the pores [9]. However, for the simulation of the PCM HX, where the actual physical size is usually much larger than the pore size, modeling the porous media at the REV scale is more efficient.

Among the recent developments and studies of the enthalpy-based lattice Boltzmann methods, Huang et al. [47] developed a total enthalpy-based LB model to treat the latent-heat source term, which can avoid the iteration steps in solving the energy equation. Liu and He [51] developed a double multi-relaxation-time (MRT) LB model for PCM melting in porous media at the REV scale. Gao et al. [48] utilized an enthalpy-based MRT-LB model at the REV scale to simulate the

conjugate heat transfer problem, such as the porous PCM melting with conduction fins. Ren et al. [52] utilized enthalpy-based immersed boundary LBM to simulate PCM melting at pore-scale, where the detailed geometry of the porous media was modeled. These studies have laid a solid foundation for investigating PCM phase change with porous media using the enthalpy-based LBM. However, these models need to be extended to 3D for simulating the convective PCM phase change in cylindrical HX. In that regard, the axisymmetric LB model stands out as it simplifies the computation of the thermal flow in cylindrical HX from 3D to 2D, and thereby saves considerable computation costs. In recent years, several axisymmetric LB models were developed for simulating the thermal flow and phase change. For example, Li et al. [49] proposed an enthalpy-based axisymmetric LB model for solid-liquid phase change and validated their model by the experimental data from a PCM solidification case. Wang et al. [53] developed a non-orthogonal double MRT-LB model for axisymmetric thermal flow with porous media. Liu et al. [43] further modified this model for simulating incompressible thermal flow. Recently, Dai et al. [8] developed a new lattice Boltzmann model that follows the predictor-corrector step instead of the streaming-collision step in traditional LBM and studied a partially heated rectangular PCM storage container as shown in Fig. 1.3, where optimal heat source locations can be determined from their simulation results under varied conditions such as the heat source length and Rayleigh numbers.

However, some of these axisymmetric models only simulate the porous thermal flow without phase change, while the models that simulate the phase change usually do not consider the porous media. In other words, axisymmetric LB models that

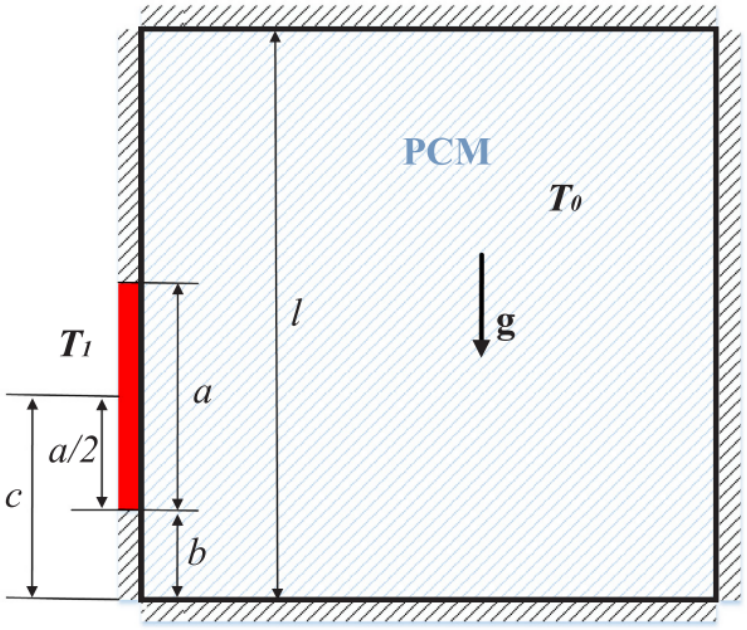

Figure 1.3: Partially heated PCM container [8].

consider PCM in porous media are limited and need to be further investigated.

Moreover, the enthalpy-based LBM in literature always model the enthalpy by step and linear functions, which can be inaccurate for the specific PCM. The commonly adopted DSC correlated enthalpy equations in convectional CFD methods has not been applied to LBM.

Moreover, the simulations of PCM phase change using LBM, as reported in the literature, usually do not consider the heat transfer fluid (HTF) flow, and the temperature or the heat flux settings on the boundaries are often held constant which is not consistent with the PCM heat transfer with the HTF. The enthalpy-based LBM that simulates the PCM phase change with fins is also limited. In that regard, the conjugate heat transfer schemes for the HTF flow and conducting fins as well as their adaptions to LBM, require further investigations.

In this dissertation, a comprehensive enthalpy-based lattice Boltzmann model is developed for the solid-liquid phase change to address the issues mentioned in this section.

1.2.6 Parallel LBM Scheme

Almost all the LBM articles highlight the advantage of LBM in developing the parallel computing scheme. Owing to its explicit streaming process and local collision process, LBM is ideally suited for parallel computing using high performance computing (HPC) resources. This is essential for performing parametric studies of PCM HX efficiently. The general method to develop the parallel LBM is introduced by Körner et al. [54].

Among all the articles that mention the benefits of applying LBM, the literature that talks about the development of the parallel LBM for the solid-liquid model is very limited. Moreover, the literature that carries out the analysis of the parallel scheme for the solid-liquid LBM is even less.

In this dissertation, the parallel LBM scheme is developed for solid-liquid LBM and scaling analyses are performed by utilizing HPC resources.

1.2.7 Numerical Study of Thermal Convective PCM Phase Change

The analysis of the convection effect on PCM phase change mainly refers to the PCM melting, as the convection effect is extremely limited in solidification cases. Following the discussion in Section 1.2.3, the Rayleigh numbers can vary over a

wide range. In some cases, the Rayleigh numbers of the PCM HX could reach 1×10^8 or even higher. In fact, the simulation of thermal convective flow and PCM melting in the literature is rare for Rayleigh number beyond 1×10^6. Such a high Rayleigh number indicates an overwhelming convective heat transfer in the liquid region over the heat conduction. But unlike the single-phase convective thermal flow, such strong nature convection is also limited by the solid phase. Given the fact that most of the numerical studies focus on the situations where either conduction and convection are balanced or conduction is dominant, the behavior of thermal flow at high Rayleigh numbers during the PCM phase change needs to be further investigated. Moreover, the effect of such a convective flow on the PCM phase change and HX performance also needs to be investigated.

In terms of the numerical models, a high Rayleigh number flow often leads to an increase in numerical errors for a constant grid size. The flow field could also become unstable and fluctuate, which further increases the difficulty to handle such a case. Thus, a robust numerical treatment needs to be developed to address this issue in order to analyze high Rayleigh number flows both accurately and efficiently.

Moreover, as discussed in Section 1.2.3, Rayleigh number flows are expected for a wide range of practical problems. Thus, a robust and efficient numerical method is required for a comprehensive parametric study over a wide range of Rayleigh numbers. The parametric studies of PCM HX at various Rayleigh numbers in the literature are limited because of the limited availability of suitable numerical methods.

In this dissertation, the parallel LBM scheme is integrated with the developed

solid-liquid lattice Boltzmann model to perform parametric studies of PCM HX under various Rayleigh numbers and geometries.

1.2.8 Literature Review Summary

The applications and studies of LHTES, the common shape and enhancement of PCM HX, categories of PCMs, and the detailed properties of paraffin wax and fatty acids are reviewed and briefly introduced in Section 1.2.1, Section 1.2.2, and 1.2.3 respectively. An estimation of the Rayleigh number, for a common PCM HX ($R = 30\ mm$) using paraffin wax or fatty acids under a reasonable temperature difference ($\Delta T = 15\ ^{\circ}\text{C}$), is provided as $1 \times 10^4 - 5 \times 10^8$ in Section 1.2.3.

Section 1.2.4 reviews general LBM and its comparison to the convectional NS-based CFD methods, indicating why choosing LBM for modeling PCM HX is often preferable over other methods.

After that, a detailed review is introduced in Section 1.2.5 of the numerical models of PCM HX. For the solid-liquid LBM, the axisymmetric LB models based on the enthalpy method have advantages of simulating circular structures such as the cylindrical HX. However, some of these axisymmetric models only simulate the porous thermal flow without phase change, while models that simulate the phase change normally do not consider porous media. In other words, axisymmetric LB models that consider both porous thermal flow and PCM phase change are limited and need to be further investigated. Moreover, the enthalpy-based LBM in the literature always models enthalpy by step and linear functions, which can be inaccurate

for some PCMs. And the commonly adopted DSC correlated enthalpy equations in convectional CFD methods have not been applied to LBM. Moreover, the conjugate heat transfer schemes for HTF flow and conducting fins as well as their adaptions to LBM require further investigations.

Section 1.2.6 briefly introduces the parallel LBM scheme, mentioning that both the development and analysis of the parallel scheme for solid-liquid LBM are extremely limited, which requires further investigations.

As for the numerical studies of PCM HX, the validations of the numerical models with experimental results for some cases such as the porous PCM melting in cylindrical HX are limited. Few studies discuss the evaluations of the PCM HX under various Rayleigh numbers and HX geometries, including the parametric studies and performance analysis. Section 1.2.7 further points out that the simulation of the PCM HX at high Rayleigh numbers ($Ra > 1 \times 10^6$) requires further studies and the solid-liquid models should also be modified to minimize the numerical errors caused by the flow and heat transfer at high Rayleigh numbers.

1.3 Research Gaps

According to the summary of literature review, The research gaps for the numerical studies of the PCM HX based on LBM can be divided into three categories: (A) Lack of development of LBM for practical PCM HX, (B) Requirements for accuracy and efficiency of the numerical methods in solving the convective solid-liquid phase change and (C) Insufficient parametric studies and analyses of PCM HX. The

details are listed as follows:

A. Lack of development of LBM for practical PCM HX

A.1. No lattice Boltzmann models applying DSC correlated enthalpy equations to the enthalpy-updating scheme were available prior to this study, thus restricting the accuracy of the simulation for specific PCM

A.2. The consideration of the HTF flow and the conjugate heat transfer with fins in solid-liquid LBM was limited, motivating the need for further developments and validations

A.3. No lattice Boltzmann models solving the PCM phase change with the porous media in axisymmetric coordinates were available prior to this study, which motivated further developments and validations of LBM.

B. Requirements for accuracy and efficiency of the numerical models in solving the convective solid-liquid phase change

B.1. Numerical errors increase for strong thermal convective flow ($Ra > 10^6$), which is difficult to solve for both convectional CFD methods and LBM. especially for higher Ra flow ($Ra > 10^8$)

B.2. Limited parallel schemes are reported to be developed for solid-liquid phase change models in the literature, while the parallel computing in fact is essential to efficiently perform the parametric studies of PCM HX

C. Insufficient parametric studies and analyses of PCM HX

C.1. Numerical studies of thermal behavior of the convective PCM phase change at various Rayleigh numbers and geometries need to be further investigated

C.2. Further evaluations of the PCM HX including the parametric studies and performance analyses are required for the design of the PCM HX

1.4 Research Objectives

In this section, the objectives for this research are proposed to fill the summarized gaps in Section 1.3. Overall, this research aims to (A) Develop a solid-liquid lattice Boltzmann model for PCM HX, (B) Improve the accuracy and efficiency of the developed model, and (C) Perform the parametric studies for PCM HX based on the developed model. From the simulation results, the basic physical mechanisms of the solid-liquid phase change can be revealed and the analysis of the PCM HX can be performed. The corresponding objectives of this research are as follows:

A. Develop a comprehensive solid-liquid lattice Boltzmann model for PCM HX

A.1. Model the enthalpy based on DSC correlated equations and couple with the lattice Boltzmann model

A.2. Develop a conjugate heat transfer model to consider the HTF flow and conducting fins and couple with the lattice Boltzmann model

A.3. Develop an enthalpy-based DDF-MRT lattice Boltzmann model that is capable of solving porous PCM phase change both in Cartesian and axisymmetric coordinates

B. Improve the accuracy and efficiency of the developed model

B.1. Improve the lattice Boltzmann model to accurately solve PCM melting at high Rayleigh numbers (Ra $> 10^6$)

B.2. Improve the lattice Boltzmann model to efficiently perform parametric studies of PCM HX by applying the parallel scheme

C. Perform parametric studies and analyses of PCM HX under various Rayleigh numbers, HX geometries, and enhancements

C.1. Perform parametric studies to quantify the natural convection effect on PCM melting

C.2. Evaluate the thermal performance of PCM HX under various Rayleigh numbers, HX geometries, and enhancements

1.5 Dissertation Overview

Objectives	Chapters	Sections
A	2, 3, 4, 5	–
A1	2, 4	2.5, 2.6, 4.4.1
A2	2, 4	2.4, 4.4.3, 4.5
A3	2, 3 4	2.6, 3.1, 4.3, 4.4
B	4, 5	–
B1	4	4.3, 4.4.2
B2	4, 5	4.6, 5.3
C	6	–
C1	6	6.1
C2	6	6.2, 6.3

Table 1.3: Dissertation Overview

In the following chapters, the research described in this dissertation is introduced in three main parts: (1) Development of solid-liquid LBM (Chapter 2, Chapter 3, and Chapter 4), (2) Numerical verifications and validations of the developed model (Chapter 5), and (3) parametric studies of the PCM HX (Chapter 6). Then the conclusions and future work are discussed in Chapter 7, and the contributions of the dissertation are provided in Chapter 8.

Categorizing the following chapters based on the research objectives, the index of the chapters can be listed in Table 1.3

Chapter 2: Macroscopic Governing Equations for PCM HX

Macroscopic governing equations are needed for the lattice Boltzmann models. Solving the lattice Boltzmann equations is equivalent to solving the corresponding macroscopic governing equations. Therefore, establishing valid macroscopic equations is the first step in developing a specific lattice Boltzmann model.

In this chapter, the macroscopic governing equations for PCM HX are introduced for both Cartesian coordinates (Section 2.1) and axisymmetric coordinates (Section 2.2). Section 2.3 introduces the governing equations for the porous PCM and Section 2.4 gives the additional treatment for the conducting fins in the PCM HX. It is worth noting that the macroscopic governing equations from these four sections are based on the enthalpy method, where the enthalpy equations are required to complete the governing equations. In fact, the listed governing equations can also represent the thermal convective flow without phase change by simply setting the enthalpy $h = c_p T$ (Section 2.5). The enthalpy equations for simulating the solid-liquid phase change are introduced in Section 2.5. To better couple the DSC correlated enthalpy equations in Section 2.5.2 with the governing equations, a modified energy equation is proposed in Section 2.6 which is more comprehensive in solving various heat transfer cases of the PCM HX. Besides, several critical di-

mensionless parameters are listed in Section 2.7. Additionally, this chapter does not talk about the boundary and phase interface settings, since they are treated in the lattice Boltzmann method, which are introduced in Chapter 4.

2.1 Pure PCM in Cartesian Coordinates

For a general PCM container in Cartesian Coordinates (x, y), the flow particle within the liquid PCM zone that has velocity $\mathbf{u} = (u_x, u_y)$ is subjected to the gravity $\mathbf{G} = (0, G_y)$. For the thermal convective flow in the liquid zone, where the driven force is not drastic, it is reasonable to assume the fluid flow is laminar and incompressible. In terms of the energy aspect, the heat transfer is conducted through the whole container, including both the liquid and the solid PCM that has temperature T and constant specific heat capacity c_p as their thermal properties. The energy equation based on total enthalpy is adopted for PCM melting. Based on the assumptions above, the macroscopic governing equations can be described as follows [47]:

$$\nabla \cdot \mathbf{u} = 0, \tag{2.1}$$

$$\frac{\partial \mathbf{u}}{\partial t} + (\mathbf{u} \cdot \nabla)\mathbf{u} = -\frac{1}{\rho_l}\nabla P + v_l \nabla^2 \mathbf{u} + \mathbf{G}, \tag{2.2}$$

$$\frac{\partial h}{\partial t} + \nabla \cdot (c_p T \mathbf{u}) = \nabla \cdot (\alpha \nabla (c_p T)), \tag{2.3}$$

where ρ_l is the mean fluid density, P is the fluid pressure, T is the temperature, h is the enthalpy, v_l is the kinematic viscosity of liquid PCM, α is the thermal diffusivity which can be different between solid and liquid phases.

Based on the Boussinesq approximation, the density difference due to the temperature variation is combined with the gravitational constant for the calculation of the buoyancy force, while this density difference can be ignored for the calculation of other terms in the governing equations under the assumption of incompressible flow. If the Boussinesq approximation is used for modeling the buoyancy force, then $\mathbf{G} = (0, G_y)$ can be further described as

$$\mathbf{G} = (0, g\beta(T - T_0)), \tag{2.4}$$

where g is the gravitational acceleration, β is the thermal expansion coefficient that describes the volume changes of the liquid PCM due to the temperature difference, and T_0 is the reference temperature.

2.2 Pure PCM in Axisymmetric Coordinates

The macroscopic governing equations in Cartesian coordinates can be readily converted to axisymmetric coordinates under the same assumptions. The governing equations are as follows [49]:

$$\frac{1}{r}\frac{\partial(ru_r)}{\partial r} + \frac{\partial u_z}{\partial z} = 0, \tag{2.5}$$

$$\frac{\partial u_r}{\partial t}+\frac{1}{r}\frac{\partial(ru_ru_r)}{\partial r}+\frac{\partial(u_zu_r)}{\partial z}=-\frac{1}{\rho_l}\frac{\partial(P)}{\partial r}+v_l\left[\frac{1}{r}\frac{\partial}{\partial r}(r\frac{\partial u_r}{\partial r})+\frac{\partial^2 u_r}{\partial z^2}-\frac{u_r}{r^2}\right], \quad (2.6)$$

$$\frac{\partial u_z}{\partial t}+\frac{1}{r}\frac{\partial(ru_zu_r)}{\partial r}+\frac{\partial(u_zu_z)}{\partial z}=-\frac{1}{\rho_0}\frac{\partial(P)}{\partial z}+v_l\left[\frac{1}{r}\frac{\partial}{\partial r}(r\frac{\partial u_z}{\partial r})+\frac{\partial^2 u_z}{\partial z^2}\right]+G_z, \quad (2.7)$$

$$\frac{\partial h}{\partial t}+\frac{\partial(c_pTu_r)}{\partial r}+\frac{\partial(c_pTu_z)}{\partial z}=\alpha\left[\frac{\partial^2(c_pT)}{\partial r^2}+\frac{\partial^2(c_pT)}{\partial z^2}+\frac{1}{r}\frac{\partial(c_pT)}{\partial r}\right]-\frac{c_pTu_r}{r}, \quad (2.8)$$

where u_r and u_z are the components of the velocity $\mathbf{u}$ in the radial (r) and the axial (z) directions respectively, G_z is the component of $\mathbf{G}$ in the axial direction and its expression is exactly the same as Eq. (2.4) in Cartesian coordinates. It is worth noting that unlike the Cartesian governing equations (2.1 - 2.3) which are in the vector form, the axisymmetric governing equations are expanded into both radial and axial directions so that they can be clearly demonstrated.

2.3 PCM with Porous Media

By means of adding the porous media with high thermal conductivity, heat transfer in PCM HX is enhanced at the expense of reduced maximum energy storage. From the basic assumptions of pure PCM, additional assumptions are made to

model the interactions between the PCM and the porous media. First, the porous media considered in this dissertation is fixed in PCM HX which enables the liquid PCM to flow through. It is assumed that both the porous media and the PCM are isotropic and homogeneous, and viscous heat dissipation is neglected. Based on the REV-scale approach, the porosity of porous media ϕ is defined as the ratio of the volume of the void space to the total volume of PCM HX. Within the liquid PCM zone, the flow is subjected to the total external force $\mathbf{F} = (F_r, F_z)$ including gravity and the drag force exerted by the porous media. The effect of the external force on the solid PCM, however, can be neglected since the solid PCM and the porous media are assumed to be rigid without any motion. Following the above assumptions, the Brinkman-Forchheimer extended Darcy approach is utilized to model the momentum equation and account for the non-linearity of the fluid flow within the porous media. For the energy aspect, the total enthalpy-based energy equation is adopted with the local thermal equilibrium assumption for PCM melting, which means that the temperatures of the porous media and the PCM are consistent at one location. Moreover, an effective thermal conductivity is introduced to represent the overall thermal conductivity of the combination of PCM and porous media at the REV scale.

Based on all the assumptions from previous sections in this chapter, the macroscopic governing equations at the REV scale for porous PCM can then be expressed as follows [48, 51]:

$$\nabla \cdot \mathbf{u} = 0, \tag{2.9}$$

$$\frac{\partial \mathbf{u}}{\partial t} + (\mathbf{u} \cdot \nabla)(\frac{\mathbf{u}}{\phi}) = -\frac{1}{\rho_l}\nabla(\phi P) + v_e \nabla^2 \mathbf{u} + \mathbf{F}, \tag{2.10}$$

$$\frac{\partial h}{\partial t} + \nabla \cdot (c_p T \mathbf{u}) = \nabla \cdot (\alpha_e \nabla (c_p T)), \tag{2.11}$$

where ϕ is the porosity of the porous media, v_e is the effective fluid kinematic viscosity, α_e is the effective thermal diffusivity, and total external force $\mathbf{F} = (F_x, F_y)$. is defined as

$$\mathbf{F} = -\frac{\phi v_e}{K}\mathbf{u} - \frac{\phi C}{\sqrt{K}}|\mathbf{u}|\mathbf{u} + \phi \mathbf{G}, \tag{2.12}$$

where K is the permeability, C is the inertial coefficient which is a function of the geometry of the porous media [55] and $|\mathbf{u}|$ is calculated as $|\mathbf{u}| = \sqrt{u_x^2 + u_y^2}$. The first and second terms on the right-hand side in Eq. (2.12) represent the first (Darcy's term) and second (Forchheimer's extension) order drag forces between the fluid and the porous structures which are used to account for the effect of the porous media to the fluid flow in the liquid zone. The third term on the right-hand side in Eq. (2.12) represents the buoyancy force where the Boussinesq approximation is applied, therefore $\mathbf{G} = (0, G_y)$ has the same expression as Eq. (2.4).

For axisymmetric coordinates, the governing equations are [43, 49]:

$$\frac{1}{r}\frac{\partial (r u_r)}{\partial r} + \frac{\partial u_z}{\partial z} = 0, \tag{2.13}$$

$$\frac{\partial u_r}{\partial t} + \frac{1}{r\phi}\frac{\partial (r u_r u_r)}{\partial r} + \frac{1}{\phi}\frac{\partial (u_z u_r)}{\partial z} = -\frac{1}{\rho_l}\frac{\partial (\phi P)}{\partial r} + v_e \left[\frac{1}{r}\frac{\partial}{\partial r}(r\frac{\partial u_r}{\partial r}) + \frac{\partial^2 u_r}{\partial z^2} - \frac{u_r}{r^2}\right] + F_r, \quad (2.14)$$

$$\frac{\partial u_z}{\partial t} + \frac{1}{r\phi}\frac{\partial (r u_z u_r)}{\partial r} + \frac{1}{\phi}\frac{\partial (u_z u_z)}{\partial z} = -\frac{1}{\rho_0}\frac{\partial (\phi P)}{\partial z} + v_e \left[\frac{1}{r}\frac{\partial}{\partial r}(r\frac{\partial u_z}{\partial r}) + \frac{\partial^2 u_z}{\partial z^2}\right] + F_z, \quad (2.15)$$

$$\frac{\partial h}{\partial t} + \frac{\partial (c_p T u_r)}{\partial r} + \frac{\partial (c_p T u_z)}{\partial z} = \alpha_e \left[\frac{\partial^2 (c_p T)}{\partial r^2} + \frac{\partial^2 (c_p T)}{\partial z^2} + \frac{1}{r}\frac{\partial (c_p T)}{\partial r}\right] - \frac{c_p T u_r}{r}, \quad (2.16)$$

where total external force $\mathbf{F} = (F_r, F_z)$ has the same form with Eq. (2.12) but in the radial (r) and the axial (z) directions.

The above governing equations still have the terms that need to be further defined and modeled, which are the inertial coefficient C, the permeability K, and the effective thermal diffusivity α_e. The effective viscosity can be set equal to the kinematic viscosity of liquid PCM v_l because the viscosity of liquid PCM can be assumed to be independent of the properties of porous media.

The inertial coefficient C is modeled based on a correlation [56], and the permeability K can be calculated from the Kozeny-Carman equation [55], as shown in

the following equations:

$$C = \frac{1.75}{\sqrt{150\phi^3}}, \tag{2.17}$$

$$K = \frac{\phi^3 d_p^2}{150(1-\phi)^2}, \tag{2.18}$$

where d_p is the mean diameter of the equivalent spherical pores for the porous media.

The effective thermal diffusivity is defined as $\alpha_e = k_e/(\rho_l c_p)$, where k_e is the effective thermal conductivity. The effective thermal conductivity is not only determined by the thermal conductivities of the PCM and the porous media, but also dependent on the structure of the porous media and the volume fraction of the PCM. Many models have been developed to evaluate the effective thermal conductivity for various porosity ranges. Taking the high porosity range ($\phi \geqslant 0.9$) for instance, an analytical model based on the tetradecahedron cells can be adopted, which was proposed by Yang et. al [57]. Assuming the porosity ϕ of the porous media is known, the equation to calculate the effective thermal conductivity is given by

$$\frac{k_e}{k_{p,m}} = \frac{1-\phi}{\left(1-e+\frac{3e}{2a}\right)\left[3(1-e)+1.5ae\right]} + \frac{k_f}{k_{p,m}}\phi, \tag{2.19}$$

where $k_{p,m}$ is the thermal conductivity of the porous media, k_f is the thermal conductivity of the PCM, a and e are the two dimensionless parameters that are related to the structure of the porous media. By setting $a = 1.5$ and $e = 0.3$, the results from Yang et. al indicated that the correlated effective thermal conductivity k_e in the high porosity range ($\phi \geqslant 0.9$) had a good agreement with the experimental data [57]. Other models developed to describe the effective thermal conductivity

were also summarized in [57], where the models for other porosity ranges could be found.

2.4 PCM with Conducting Fins

Unlike the temperature-based method, the thermal transport of conducting fins needs to be treated separately from that of the PCM that is modeled using the enthalpy-based method. This is because the enthalpy equation for modeling the PCM is different than that for modeling the fins. Such an inconsistency can only be resolved by applying two versions of the thermal governing equation simultaneously. Therefore, in addition to the same governing equations for the PCM and the porous media (Eq. (2.1) - Eq. (2.3)), the thermal governing equations for conducting fins are represented as

$$\frac{\partial h_{fin}}{\partial t} = \nabla \cdot (\alpha_{fin} \nabla c_{p,fin} T), \tag{2.20}$$

where h_{fin} is the fin enthalpy defined as $h_{fin} = c_{p,fin} T$, and α_{fin} is the thermal diffusivity of fins calculated as $\alpha_e = k_{fin} / (\rho_f c_{p,fin})$, where k_{fin}, ρ_{fin} and $c_{p,fin}$ are the thermal conductivity, density and specific heat of conducting fins respectively.

Additionally, if the governing equation of fins is expanded in axisymmetric coordinates (r, z), Eq. (2.20) turns out to be

$$\frac{\partial h_{fin}}{\partial t} = \alpha_{fin} \left[\frac{\partial^2 (c_{p,fin} T)}{\partial r^2} + \frac{\partial^2 (c_{p,fin} T)}{\partial z^2} + \frac{1}{r} \frac{\partial (c_{p,fin} T)}{\partial r} \right], \tag{2.21}$$

2.5 Enthalpy Equations

For conducting fins mentioned in Section 2.4, the enthalpy can be simply defined as $h_{fin} = c_{p,fin}T$. However, it becomes more complicated for the PCM, especially with the porous media. In order to elaborate the enthalpy modeling more concisely, the enthalpy equations introduced in this section consider both the PCM and the porous media. The weight of each component in the equations is adjusted by the porosity ϕ of the porous media at the REV scale. So the enthalpy equations can be simply reduced to describe the pure PCM by setting $\phi = 1$. In solid-liquid LBM, the most adopted enthalpy equations are based on the step and Linear functions, which are introduced in Section 2.5.1. For better accuracy of the enthalpy modeling, the enthalpy equations based on the DSC test data of the PCM are first introduced into LBM and the details are demonstrated in Section 2.5.2

2.5.1 Enthalpy Modeling Based on Step and Linear Functions

For porous PCM, the local temperatures among the liquid PCM, the solid PCM and the porous media remain the same under the local thermal equilibrium assumption. Thereby the heat transfer process of the porous PCM can be described by the governing equations mentioned above, where the local temperature is represented as T for all the components. The corresponding enthalpy h in the governing equation can be then divided into the sensible enthalpy and the latent enthalpy, as

shown in the equation below:

$$h = h_{sensible} + h_{latent}. \tag{2.22}$$

The general method followed in LBM to describe the enthalpy is by defining enthalpy h as a linear function of the temperature and the liquid fraction of the PCM [51]. Based on this method, the sensible enthalpy and the latent enthalpy can be expressed as

$$\begin{aligned} h_{sensible} &= h_{pcm} + h_{p,m} \\ &= \phi \left[f_l c_{p,l} + (1 - f_l) \frac{\rho_s}{\rho_l} c_{p,s} \right] T + (1 - \phi) \frac{\rho_m}{\rho_l} c_{p,m} T, \end{aligned} \tag{2.23}$$

$$h_{latent} = \phi f_l L_a, \tag{2.24}$$

where h_{pcm} is the sensible enthalpy of the PCM, $h_{p,m}$ is the sensible enthalpy of the porous media, $c_{p,l}$, $c_{p,s}$ and $c_{p,m}$ are the specific heat at constant pressure for the liquid PCM, solid PCM and the porous media respectively, ρ_s and ρ_m are the mean densities of the solid PCM and the porous media respectively and f_l is the liquid fraction of the PCM defined as,

$$f_l = \begin{cases} 0, & h \leqslant h_s, \\ \frac{h_{pcm} - h_s}{h_l - h_s}, & h_s < h < h_l, \\ 1, & h \geqslant h_l, \end{cases} \tag{2.25}$$

where h_s is the enthalpy at the temperature T_s when the PCM starts to melt, and h_l is the enthalpy at the temperature T_l when the PCM fully turns into liquid. The difference between T_s and T_l is also known as the temperature glide of the PCM ($\Delta T_{glide} = T_l - T_s$). Given the fact that the phase transition of PCM is gradual, it is hard to distinguish clear temperature points when the PCM begins and ends the phase transition. Therefore, the temperature glide is always a manually set parameter, and its value can even be different in the literature for the same PCM. In the enthalpy modeling based on the step and linear functions, different temperature glide settings can lead to different enthalpy profiles and thus affect the accuracy of the enthalpy model. Based on the author's modeling experience, the temperature glide setting needs to be adjusted in order to obtain the best match of the enthalpy profile, and this value is always slightly different from the specified temperature glide from the PCM manufacturer or the settings from the literature.

In the case that the sensible enthalpy of the porous media is extremely small compared with that of the PCM, the second term $h_{p,m}$ in Eq. (2.23) can be neglected. Moreover, as the porosity ϕ of the porous media approaches unity, the enthalpy equations (2.23) and (2.24) reduce to the equations for the pure PCM, and all the macroscopic governing equations in Section 2.3 are simplified to the equations for the PCM without the porous media.

2.5.2 Enthalpy Modeling Based on DSC Test Data

For accurate modeling of enthalpy for a specific PCM, the step and linear functions have limitations because of their simplified relationship between enthalpy and temperature. Therefore a commonly used method in CFD based on the DSC test data of the PCM is introduced in LBM to describe the real enthalpy profile. The equation proposed by Buschle et al. [58] is adopted to do the curve fitting of the DSC test data, which is given by

$$h_{pcm} = La \left[\frac{\arctan\left((T - T_m)C_{mr}\right)}{\pi} + 0.5 \right] + (T - T_{int}) \frac{c_{p,l} + c_{p,s}}{2}, \tag{2.26}$$

where T_{int} is the initial temperature of the PCM and C_{mr} is the coefficient that can be determined based on the given DSC test data. And more importantly, all the parameters related to the PCM properties and temperature settings in Eq. (2.26) are only used to provide a good starting point to correlate the test data, they do not need to be exactly the same as the real values. A better match with the DSC test data can be achieved if these parameters are tuned to proper values.

One of the significant parameters of DSC test is scan rate which always leads to the delay in the measurement of heat flow, deforming the enthalpy profile of PCM. To minimize the error caused by the delay from DSC test, the calculated enthalpy profile from Eq. (2.26) is shifted from the DSC profile to match the actual enthalpy profile based on the melting temperature of PCM. For instance, Fig. 2.1 gives the enthalpy profile of PT37 from the DSC test at 1 K/min scan rate (green

line) and the correlated enthalpy profile calculated based on Eq. (2.26) (red line).

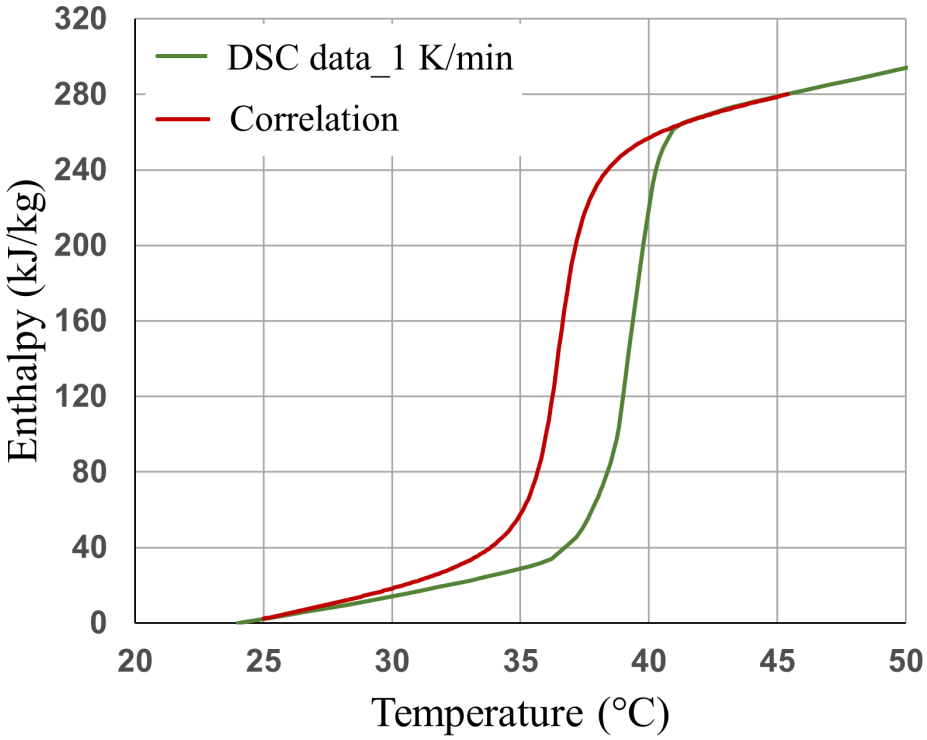

Figure 2.1: Enthalpy profile of PT37.

Once the correlated enthalpy in Eq. (2.26) of a specific PCM is utilized in LB models, the total enthalpy can be defined as

$$h = \phi h_{pcm} + (1 - \phi)\frac{\rho_m}{\rho_l} c_{p,m} T. \tag{2.27}$$

Since the enthalpy equation is correlated with the real DSC test data of the specific PCM, there is no need to determine a precise temperature glide for the enthalpy modeling, which is another advantage of this model compared with the model based on the step and linear functions in Section 2.5.1. And the temperature glide is then

only utilized to calculate the liquid fraction that determines the phases of the PCM in solid-liquid LBM, which does not require high precision of the temperature glide.

2.6 Modified Energy Equations for DSC Enthalpy Modeling

For the enthalpy modeling based on the step and linear functions, the latent enthalpy part is based on the liquid fraction f_l times the latent heat L_a, and thus the specific heat capacities c_p can be treated as constant both in the liquid and solid phases respectively. This simplification is not valid upon using the DSC correlated enthalpy equations because the specific heat capacity continues to vary as the temperature changes. Consequently, the corresponding solid-liquid LBM based on Eq. (2.3) and Eq. (2.11) are not sufficient to solve the PCM phase change accurately.

To address this issue, a modified macroscopic energy equation is proposed to account for the variable specific heat capacity. The enthalpy-based governing equations 2.3 and 2.11 are derived from the energy equation regarding the latent heat as a source term. This basic energy equation is given by [59]

$$\frac{\partial(c_pT)}{\partial t} + \nabla \cdot (c_pT\mathbf{u}) = \nabla \cdot (\frac{k}{\rho_l}\nabla T) - \frac{\partial(f_lL_a)}{\partial t} - \nabla \cdot (f_lL_a\mathbf{u}), \tag{2.28}$$

where the second and third terms on the right-hand side are the source term representing the latent heat. Combining the first term on the left-hand side with the second term on the right-hand side and defining the enthalpy as $h = c_pT + f_lL_a$, then the first term can be $(\frac{\partial h}{\partial t})$. If the third term on the right-hand side is further neglected and the thermal diffusivity based on constant c_p is applied, the same form

of Eq. (2.3) and Eq. (2.11) can be obtained.

For the modified energy equation, the third term on the right-hand side is not canceled, but combined with the second term on the left-hand side to form the term $\nabla\cdot(h\mathbf{u})$. Moreover, the basic solid-liquid LBM uses the thermal diffusivity defined as $\alpha = k/(\rho_l c_p)$ to calculate the relaxation parameter, which governs the heat transfer. This relaxation parameter should keep constant for one phase to maintain numerical stability. Therefore, the basic solid-liquid LBM is only effective for constant c_p. To address the variable specific heat capacity, a referenced specific heat capacity ($c_{p,ref}$) is utilized in the calculation of the thermal diffusivity [59]. This constant value can make the thermal diffusivity only dependent on the fixed thermal conductivity k for one phase. The choice of $c_{p,ref}$ is relatively arbitrary, but can not be larger than twice the minimum value of c_p between solid and liquid phases in order to maintain the numerical stability [48]. The value of $c_{p,ref}$ is recommended to be the harmonic mean of the specific heats between the solid and liquid phases [59]. It can also be adjusted to a lower value to maintain the numerical stability of solid-liquid LBM if the thermal conductivity is very small [60].

After the modifications above, the new macroscopic energy equation can be derived, which is given by

$$\frac{\partial h}{\partial t} + \nabla \cdot (h\mathbf{u}) = \nabla \cdot (\alpha_{ref} \nabla (c_{p,ref} T)), \tag{2.29}$$

where $\alpha_{ref} = k/(\rho_l c_{p,ref})$ is the thermal diffusivity based on the referenced specific heat capacity $c_{p,ref}$, where the thermal conductivity k can be set to k_e for the porous

PCM.

Although the enthalpy h in Eq. (2.29) is defined as $h = c_p T + f_l L_a$, the expression can be modified without changing the form of the energy equation. Therefore, the DSC correlated enthalpy equations (2.26 and 2.27) proposed in Section 2.5.2 can be directly applied to Eq. (2.29).

An expanded form of Eq. (2.29) in axisymmetric coordinates is also given here as

$$\frac{\partial h}{\partial t} + \frac{\partial (h u_r)}{\partial r} + \frac{\partial (h u_z)}{\partial z} = \alpha_{ref} \left[\frac{\partial^2 (c_{p,ref} T)}{\partial r^2} + \frac{\partial^2 (c_{p,ref} T)}{\partial z^2} + \frac{1}{r} \frac{\partial (c_{p,ref} T)}{\partial r} \right] - \frac{h u_r}{r}. \tag{2.30}$$

By substituting Eq. (2.29) and Eq. (2.30) into the governing equations from the previous sections (Section 2.1 - Section 2.4), the modified macroscopic governing equations are more comprehensive and can be utilized to describe the pure heat conduction, thermal convective flow and PCM phase change, with and without porous media, both in Cartesian coordinates and axisymmetric coordinates.

2.7 Critical Dimensionless Parameters

In addition to the porosity ϕ, the above macroscopic governing equations in this chapter are also characterized by several critical dimensionless parameters which

are defined s follows:

$$
\begin{aligned}
&\text{Rayleigh number} && Ra = \frac{g\beta(T_h - T_m)L^3}{v_l \alpha_l}, \\
&\text{Stefan number} && Ste = \frac{c_{p,l}(T_h - T_m)}{L_a}, \\
&\text{Darcy number} && Da = \frac{K}{L^2}, \\
&\text{Prandtl number} && Pr = \frac{v_l}{\alpha_l}, \\
&\text{Reynolds number} && Re = \frac{u_c L}{v_l}, \\
&\text{viscosity ratio} && J = \frac{v_e}{v_l}, \\
&\text{thermal diffusivity ratio} && \lambda = \frac{\alpha_e}{\alpha_l},
\end{aligned} \tag{2.31}
$$

where the subscript l denotes the properties of the liquid PCM, the subscript e denotes the effective properties, T_h is the highest temperature of the PCM, T_m is the melting temperature of the PCM, L_a is the latent heat of the PCM, L is the characteristic length and u_c is the characteristic velocity which is defined as $u_c = \sqrt{g\beta(T_h - T_m)L}$ for the convective thermal flow. The listed dimensionless parameters in Eq. (2.31) are the Rayleigh number (Ra), the Stefan number (Ste), the Darcy number (Da), the Prandtl number (Pr), the Reynolds number (Re), the viscosity ratio (J) and the thermal diffusivity ratio (λ) respectively.

For the convective thermal flow, the Rayleigh number (Ra) measures the thermal convection over the thermal conduction in the PCM liquid zone. When Ra is below a critical value (Ra_c), the flow convection effect can be neglected, and thus the heat transfer is dominated by the conduction heat transfer. If Ra exceeds Ra_c,

natural convection starts to affect the heat transfer. The convection heat transfer becomes more dominant as Ra continues to increase. By substituting the expression of Ra with the Reynolds number (Re), the Prandtl number (Pr) and the characteristic velocity u_c, Rayleigh number can also be represented as

$$\mathrm{Ra} = \mathrm{Re}^2 Pr, \tag{2.32}$$

where the Reynolds number (Re) with the characteristic velocity u_c measures the inertia force (buoyancy force in thermal convective flow) over viscous force, which can be utilized to determine whether the generated liquid flow is laminar or turbulent, and the Prandtl number (Pr) is defined as the ratio of momentum diffusivity to thermal diffusivity, which depends only on the fluid properties.

For the thermal convective flow and phase change, the flow velocity in the liquid zone is determined by the temperature difference and thermal expansion effect. In other words, the fluid flow is driven by the density difference caused by the uneven temperature field. The natural convection effect from the generated fluid flow in the liquid zone further influence the heat transfer and the temperature field. Such an interaction between fluid flow and heat transfer is better described by the Rayleigh number (Ra) rather than the Reynolds number (Re).

For the pure PCM, the Stefan number (Ste) is defined as the sensible heat over latent heat and can be calculated based on the thermal properties of the PCM. The lower value of the Stefan number (Ste) represents the stronger ability of energy storage. The Stefan number (Ste) is usually far less than one for the PCM with

large latent heat.

For the porous media, the Darcy number (Da) represents the permeability of the media over the cross-sectional area based on the characteristic length L. It indicates the ability of the flow to pass through the porous media. A lower value of the Darcy number (Da) leads to smaller generated thermal flow due to the presence of the porous media. In addition to the Darcy number, the viscosity ratio (J) and the thermal diffusivity ratio (λ) are also used to describe the fluid flow and heat transfer in the porous media at the REV scale. The viscosity ratio (J) is less important and usually set to unity for porous flow by assuming a constant viscosity of the fluid. While the thermal diffusivity ratio (λ) matters more because the effective thermal diffusivity α_e calculated based on the effective thermal conductivity k_e determines the overall heat transfer of the fluid with porous media.

For the porous PCM, the above dimensionless parameters govern the fluid flow and heat transfer in the liquid PCM zone. In the solid PCM zone, pure conduction heat transfer is considered and calculated based on the thermal diffusivity of solid phase ($\alpha_s = k_s/(\rho c_{p,s})$) for pure PCM and effective thermal diffusivity of solid phase ($\alpha_e = k_e/(\rho c_{p,s})$) for porous PCM respectively. It is worth noting that the difference in the thermal conductivities between the liquid and solid phases of the PCM is relatively small compared with the thermal conductivity of the enhanced porous media, which results in only a tiny variation of the calculated effective thermal conductivities between solid and liquid phase. Such a variation can be neglected, and therefore it is reasonable to assume $k_e = k_{e,l} = k_{e,s}$.

2.8 Chapter Summary

In this chapter, the detailed macroscopic governing equations of the convective thermal flow and phase change are introduced both in Cartesian and axisymmetric coordinates, with and without porous media (Section 2.1, Section 2.2 and Section 2.3). Moreover, the treatment of conducting fins is discussed in Section 2.4.

To complete the governing equations for the PCM phase change, the corresponding enthalpy equations are introduced in Section 2.5, including the modeling based on the step and linear functions in Section 2.5.1 and that based on the DSC test data of PCM in Section 2.5.1. Moreover, a modified macroscopic energy equation is then proposed in Section 2.6, which is developed to better work with the enthalpy modeling based on the DSC test data. Lastly, several critical dimensionless parameters that characterize the fluid flow and heat transfer in thermal convective phase change are introduced in Section 2.7.

Chapter 3: Single-Phase Lattice Boltzmann Models

The single-phase LBM is fundamental to the solid-liquid LBM. Chapter 2 introduces the macroscopic governing equations for PCM HX from which the lattice Boltzmann model is developed. Following that, this chapter talks about the single-phase lattice Boltzmann model both for fluid flow and heat transfer. In terms of the development of solid-liquid LBM, the general method is to simulate the liquid PCM zone by applying single-phase LBM for flow field, while the heat transfer side needs much more improvement from the single-phase thermal LBM than the flow side. Therefore, the focus is on the flow field in this chapter, and only a brief introduction of the single-phase thermal LBM is given in this chapter.

3.1 Single-Phase Lattice Boltzmann Models for Flow Field

In this section, the introduction of the basic lattice Boltzmann model for fluid flow is given in Section 3.1.1. Moreover, the external forcing scheme (Section 3.1.2), MRT scheme of the model (Section 3.1.3) and the development of the model in axisymmetric coordinates (Section 3.1.4) are also discussed.

3.1.1 Basic LBGK D2Q9 Lattice Boltzmann Model

The basic BGK LB model originated from the collision model proposed by Bhatnagar, Gross and Krook in 1954 [61]. In 1991, Chen et. al [62] proposed a single-relaxation-time (SRT) scheme to further simplify the collision process of the BGK model. In 1992, Qian et. al [63] developed a model based on the same theory and first named it as Lattice BGK (LBGK) model. LBGK model itself can only solve for fluid flow. However a number of models based on the LBGK model have been developed for heat transfer since then which are introduced later in Section 3.2.

The key feature of LBGK model is the replacement of the complicated collision term in the Boltzmann equation with a solvable BGK collision operator, followed by the discretization of the Boltzmann equation in both space and time. For a given lattice meshgrid of the fluid field in Cartesian coordinates as shown in Fig. 3.1, the discrete Boltzmann equation with the BGK collision operator is given as

$$\mathbf{f}(\mathbf{x}+\mathbf{e}\delta_t,t+\delta_t)-\mathbf{f}(\mathbf{x},t)=-\frac{1}{\tau_v}\left[\mathbf{f}(\mathbf{x},t)-\mathbf{f}^{eq}(\mathbf{x},t)\right], \tag{3.1}$$

where $\mathbf{f}(\mathbf{x},t)$ is the vector of the density distribution functions at a given location $\mathbf{x}=(x,y)$ and time t, $\mathbf{e}$ is the vector of the discrete velocities, τ_v is the relaxation time of the BGK collision operator, $\mathbf{f}^{eq}(\mathbf{x},t)$ is the corresponding equilibrium distribution functions.

For each grid point such as x_0 in Fig. 3.1, together with its neighboring points, form a basic lattice structure. The lattice structure can be either one dimensional,

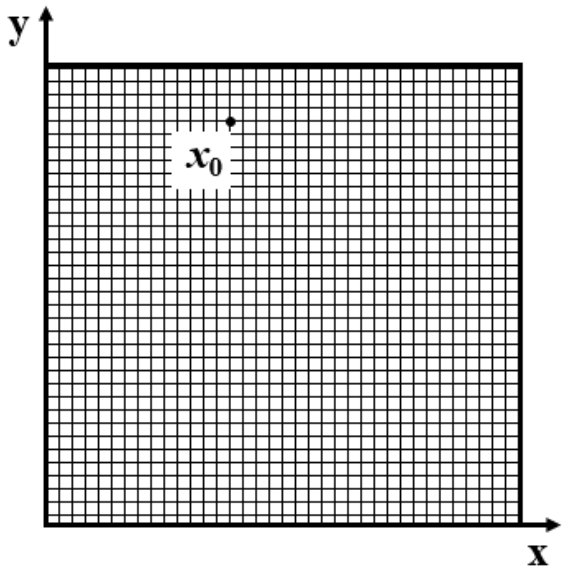

Figure 3.1: Lattice meshgrid in Cartesian coordinates.

two-dimensional or three-dimensional, and the lattice velocities starting from the center point must orient towards its nearby points, including the center point itself (representing the velocity of a group of particles that stay at the center point). It is obvious that the number of components of the velocity vector can not exceed the number of the points in the lattice structure. And other vectors such as the density distribution function, which represents the number of particles in each group that follow each corresponding velocity, should have the same number of the components as the velocity vector. Therefore, the lattice structure is the basis of the lattice Boltzmann model, which is characterized by its dimensions and the number of components in the velocity vector. Generally, the lattice structure can be named as $DmQn$, where m represents the space dimensions and n represents the number of the lattice velocities per lattice node. The model that has a $DmQn$ lattice structure is also called $DmQn$ lattice model. The formulation of $\mathbf{f}(\mathbf{x}, t)$, $\mathbf{f}^{eq}(\mathbf{x}, t)$, $\mathbf{e}$ can vary

for different lattice models. Taking the most commonly used two-dimensional lattice model D2Q9 as an example, the lattice structure with the velocity vector is shown in Fig. 3.2.

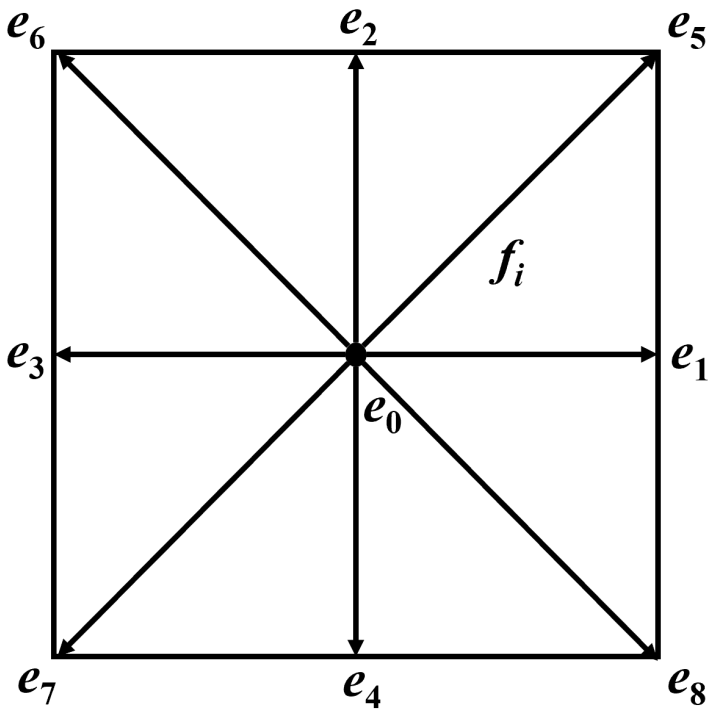

Figure 3.2: D2Q9 lattice structure.

The vector of the discrete velocities for D2Q9 $\mathbf{e} = \{e_i | i = 0, 1, ..., 8\}$ are given as

$$e_i = \begin{cases} (0,0), & i = 0, \\ c(cos[(i-1)\pi/2], sin[(i-1)pi/2]), & i = 1-4, \\ \sqrt{2}c(cos[(2i-9)\pi/4], sin[(2i-9)pi/4]), & i = 5-8, \end{cases} \tag{3.2}$$

where $c = \delta_x/\delta_t$ is the lattice speed and δ_x is the discrete lattice spacing in the x

direction. And the equilibrium distribution functions $\mathbf{f}^{eq}(\mathbf{x},t)$ for D2Q9 is given by

$$f_i^{eq} = \omega_i \rho \left[\frac{\mathbf{e}_i \cdot \mathbf{u}}{c_s^2} + \frac{(\mathbf{e}_i \cdot \mathbf{u})^2}{2\phi c_s^4} - \frac{|\mathbf{u}|^2}{2\phi c_s^2} \right], \tag{3.3}$$

where $c_s = c/\sqrt{3}$ is the lattice sound speed of the D2Q9 model, and ω_i is the weight coefficient of the D2Q9 model given by

$$\omega_i = \begin{cases} \frac{4}{9}, & i = 0, \\ \frac{1}{9}, & i = 1,2,3,4, \\ \frac{1}{36}, & i = 5,6,7,8. \end{cases} \tag{3.4}$$

The fluid evolution process described by Eq. (3.1) can be divided into two processes: the collision process and the streaming process. The collision process for a lattice node is completely local and does not require the values of distribution functions from its nearby nodes, which is given by

$$\mathbf{f}^*(\mathbf{x},t) = \mathbf{f}(\mathbf{x},t) - \frac{1}{\tau_v} \left[\mathbf{f}(\mathbf{x},t) - \mathbf{f}^{eq}(\mathbf{x},t) \right], \tag{3.5}$$

where $\mathbf{f}^*(\mathbf{x},t)$ denotes the redistributed functions at location $\mathbf{x} = (x,y)$ after the collision process. And the streaming process can be described as

$$\mathbf{f}(\mathbf{x} + \mathbf{e}\delta_t, t + \delta_t) = \mathbf{f}^*(\mathbf{x},t), \tag{3.6}$$

which means the redistributed functions $\mathbf{f}^*(\mathbf{x},t)$ are transferred from the current

lattice node to its nearby nods after one time step. According to the Eq. (3.6), the streaming process of the LB model is completely explicit for time steps.

The macroscopic fluid density ρ and velocity $\mathbf{u} = (u_x, u_y)$ can be recovered from the density distribution functions f_i through the statistical process. For D2Q9 lattice model, the calculations are given below:

$$\rho = \sum_{i=0}^{8} f_i, \tag{3.7}$$

$$\mathbf{u} = \frac{1}{\rho} \sum_{i=0}^{8} e_i f_i. \tag{3.8}$$

3.1.2 External Forcing Schemes

The basic LBGK model does not have the external force term. To extend the application of LBM, many forcing scheme have been devised to solve the fluid flow with external forces. Generally, the methods to account for the external force in LBM are either adding force terms to the collision process or shifting the velocity field [64]. In some proposed schemes, both methods are applied. In this section, two forcing schemes widely adopted in further developing the solid-liquid LBM are briefly introduced:

1. He et al. [65] devised a forcing scheme in which an external force term $\delta_t \mathbf{F}_v$ was added to the lattice Boltzmann equations, where δ_t is the discrete time

step and $\mathbf{F}_v$ is given by

$$\mathbf{F}_v = (1 - \frac{1}{2\tau_v}\frac{\mathbf{F}\cdot(\mathbf{e}-\mathbf{u})}{\rho c_s^2}\mathbf{f}^{eq}), \tag{3.9}$$

where $\mathbf{F}$ is the external force which can be expressed as Eq. (2.4) or Eq. (2.12) for thermal convective flow with and without porous media. Because of the addition of the force term, the whole equation became implicit to solve. Therefore, a transformation of the density distribution function $\bar{\mathbf{f}}$ was made to eliminate the implicitness. Following that, the lattice Boltzmann equation was rewritten as

$$\bar{\mathbf{f}}(\mathbf{x}+\mathbf{e}\delta_t,t+\delta_t) - \bar{\mathbf{f}}(\mathbf{x},t) = -\frac{1}{\tau_v}\left[\bar{\mathbf{f}}(\mathbf{x},t) - \mathbf{f}^{eq}(\mathbf{x},t)\right] + \delta_t\mathbf{F}_v(\mathbf{x},t), \tag{3.10}$$

The macroscopic density ρ and velocity $\mathbf{u}$ were then defined as

$$\rho = \sum_i \bar{f}_i, \tag{3.11}$$

and

$$\rho\mathbf{u} = \sum_i \mathbf{e}_i\bar{f}_i + \frac{\delta_t}{2}\mathbf{F}. \tag{3.12}$$

2. Guo et al. [66] proposed a forcing scheme where the external force term was added to the lattice Boltzmann equations without shifting the density distribution functions. The components in the vector form of the external force

term $\mathbf{F}_v$ can be expressed as

$$F_v = w_i(1 - \frac{1}{2\tau_v}) \left[\frac{\mathbf{e}_i \cdot \mathbf{F}}{c_s^2} + \frac{(\mathbf{e}_i \cdot \mathbf{u})(\mathbf{e}_i \cdot \mathbf{F})}{c_s^4} - \frac{\mathbf{uF}}{c_s^2} \right], \tag{3.13}$$

where i denotes the ith component in the vector, and the total number of the components is determined by the lattice structure ($DmQn$) as demonstrated in Section 3.1.1. The macroscopic properties can then be calculated as follows:

$$\rho = \sum_i f_i, \tag{3.14}$$

$$\rho \mathbf{u} = \sum_i \mathbf{e}_i f_i + \frac{\delta_t}{2} \mathbf{F}. \tag{3.15}$$

3.1.3 MRT Lattice Boltzmann Schemes

The Basic LBGK model is developed based on single-relaxation-time (SRT) scheme which lacks numerical stability, especially for low fluid viscosity. Therefore, LB models based on the multi-relaxation-time (MRT) scheme have been proposed to increase the stability and feasibility of LBM [67]. The key feature of the MRT LB model is utilizing a matrix to transform the distribution functions into a moment vector, and the relaxation time can be set differently for each component of the moment vector. Such a feature significantly increases the stability and versatility of LBM, especially for PCM HX cases.

The MRT method was devised by d'Humières [68] based on the LBGK model without an external forcing scheme. The MRT lattice Boltzmann model based on

He et al.'s forcing scheme [65] was proposed later with an explicit treatment of the forcing term [69]. Generally, the MRT scheme develops a transition matrix that can be used to turn the density distribution functions from velocity space to a moment space. For the D2Q9 model, the MRT form of the lattice Boltzmann equation with an external forcing scheme can be expressed as

$$\bar{\mathbf{f}}(\mathbf{x}+\mathbf{e}\delta_t,t+\delta_t)-\bar{\mathbf{f}}(\mathbf{x},t)=-\mathbf{M}^{-1}\mathbf{S}\left[\mathbf{m}(\mathbf{x},t)-\mathbf{m}^{eq}(\mathbf{x},t)\right]+\delta_t\mathbf{M}^{-1}\left(\mathbf{I}-\frac{\mathbf{S}}{2}\right)\mathbf{F}_m, \tag{3.16}$$

where $\bar{\mathbf{f}}(\mathbf{x},t)$ is the vector of the density distribution functions at given location $\mathbf{x}=(x,y)$ and time t, $\mathbf{e}$ is the vector of the discrete velocities, $\mathbf{M}$ is the transition matrix, $\mathbf{S}$ is the relaxation matrix, $\mathbf{m}(\mathbf{x},t)$ and $\mathbf{m}^{eq}(\mathbf{x},t)$ are the moment vector and the corresponding equilibrium moment vector respectively , $\mathbf{I}$ is the identity matrix, $\mathbf{F}_m$ is the forcing term in the moment space and δ_t is the discrete time step.

The fluid evolution process in the D2Q9 model can be described by Eq. (3.16) from which the collision process is performed in the moment space as

$$\begin{aligned}\mathbf{m}^{*}(\mathbf{x},t)=\mathbf{m}(\mathbf{x},t)&-\mathbf{S}\left[\mathbf{m}(\mathbf{x},t)-\mathbf{m}^{eq}(\mathbf{x},t)\right]\\&+\delta_t\left(\mathbf{I}-\frac{\mathbf{S}}{2}\right)\mathbf{F}_m,\end{aligned} \tag{3.17}$$

where $\mathbf{m}^{*}(\mathbf{x},t)$ denotes the redistributed moment vector at location $\mathbf{x}=(x,y)$ after the collision process. This redistributed moment vector $\mathbf{m}^{*}(\mathbf{x},t)$ can then be transferred to its nearby grids during the streaming process. However, the streaming process is performed in the velocity space as specified in Eq. (3.16). Therefore the

results from Eq. (3.17) should be transformed back to density distribution functions in the velocity space for the calculation of the streaming process, as shown below:

$$\bar{\mathbf{f}}(\mathbf{x}+\mathbf{e}\delta_t, t+\delta_t) = \mathbf{M}^{-1}\mathbf{m}^*(\mathbf{x}, t). \tag{3.18}$$

The most commonly used transition matrix $\mathbf{M}$ in the D2Q9 model is given by

$$M = \begin{bmatrix} 1 & 1 & 1 & 1 & 1 & 1 & 1 & 1 & 1 \\ -4 & -1 & -1 & -1 & -1 & 2 & 2 & 2 & 2 \\ 4 & -2 & -2 & -2 & -2 & 1 & 1 & 1 & 1 \\ 0 & 1 & 0 & -1 & 0 & 1 & -1 & -1 & 1 \\ 0 & -2 & 0 & 2 & 0 & 1 & -1 & -1 & 1 \\ 0 & 0 & 1 & 0 & -1 & 1 & 1 & -1 & -1 \\ 0 & 0 & -2 & 0 & 2 & 1 & 1 & -1 & -1 \\ 0 & 1 & -1 & 1 & -1 & 0 & 0 & 0 & 0 \\ 0 & 0 & 0 & 0 & 0 & 1 & -1 & 1 & -1 \end{bmatrix}. \tag{3.19}$$

Based on the given transition matrix $\mathbf{M}$, the vector of distribution functions $\bar{\mathbf{f}} = \{f_i | i = 0, 1, ..., 8\}$ in the velocity space can be transformed into the vector $\mathbf{m}$ in the moment space, as shown below:

$$\mathbf{m} = \mathbf{M}\bar{\mathbf{f}} = \left[\rho, e, \varepsilon, j_x - \frac{\delta_t}{2}\rho F_x, q_x, j_y - \frac{\delta_t}{2}\rho F_y, q_y, P_{xx}, P_{xy}\right]^T, \tag{3.20}$$

where j_x and j_y are the components of the flow momentum, e and ε are the terms

related to the flow energy, P_{xx} and P_{xy} are the terms related to the strain tensor, and q_x and q_y are the terms related to the energy flux. For the flow with low Mach number in the LBM ($Ma = u_c/c_s \ll 1$), the incompressible approximation [70] is adopted for the liquid PCM flow, which assumes the fluid density is composed of the constant mean fluid density ρ_0 and the density fluctuation $\delta\rho$, i.e., $\rho = \rho_0 + \delta\rho$. According to this approximation, the higher order terms such as $\delta\rho(u/c)$ and $\delta\rho(u/c)^2$ can be neglected and therefore the equilibrium moment vector $\mathbf{m}^{eq}$ for the corresponding moment vector $\mathbf{m}$ can be calculated by

$$\begin{aligned}\mathbf{m}^{eq} &= \mathbf{M}\mathbf{f}^{eq} \\ &= \left[\rho, e^{eq}, \varepsilon^{eq}, j_x, q_x^{eq}, j_y, q_y^{eq}, P_{xx}^{eq}, P_{xy}^{eq}\right]^T,\end{aligned} \tag{3.21}$$

where

$$\begin{aligned}e^{eq} &= -2\rho + 3\rho_0(u_x^2 + u_y^2), \\ \varepsilon^{eq} &= \rho - 3\rho_0(u_x^2 + u_y^2), \\ j_r &= \rho_0 u_x, j_z = \rho_0 u_y, \\ q_x^{eq} &= -\rho_0 u_x, q_y^{eq} = -\rho_0 u_y, \\ p_{xx}^{eq} &= \rho_0(u_x^2 - u_y^2), p_{xy}^{eq} = \rho_0 u_x u_y,\end{aligned} \tag{3.22}$$

and the vector of the equilibrium distribution functions $\mathbf{f}^{eq} = \{f_i^{eq} | i = 0, 1, ..., 8\}$ in velocity space is given by

$$f_i^{eq} = \omega_i \rho + \omega_i \rho_0 \left[\frac{\mathbf{e}_i \cdot \mathbf{u}}{c_s^2} + \frac{(\mathbf{e}_i \cdot \mathbf{u})^2}{2c_s^4} - \frac{|\mathbf{u}|^2}{2c_s^2}\right], \tag{3.23}$$

where $c_s = c/\sqrt{3}$ is the lattice sound speed of the D2Q9 model, and ω_i is the weight coefficient of the D2Q9 model as Eq. (3.4) shows. Noting that Eq. (3.23) is developed for incompressible flow, and it can be reduced to Eq. (3.3) by setting $\rho_0 = \rho$.

Based on the moment vector given in Eq. (3.21), the relaxation matrix $\mathbf{S}$ can be determined as

$$\mathbf{S} = diag(s_\rho, s_e, s_\varepsilon, s_j, s_q, s_j, s_q, s_v, s_v), \tag{3.24}$$

where overall the components of the relaxation matrix $s_i \in (0, 2)$. Among them, $s_\rho = s_j = 1.0$ indicates the mass and momentum are conserved in the flow region, and the critical relaxation rate s_v, which determines the flow pattern, is related to the fluid viscosity and can be expressed as

$$s_v = \frac{1}{\tau_v}, \tag{3.25}$$

$$\tau_v = \frac{v_l}{c_s^2 \delta_t} + 0.5, \tag{3.26}$$

where v_l is the fluid kinematic viscosity.

The forcing term $\mathbf{F}_m$ in the moment space is then defined as [69]

$$\mathbf{F}_m = \rho_0 \begin{bmatrix} 0 \\ 6(u_x F_x + u_y F_y) \\ -6(u_x F_x + u_y F_y) \\ F_x \\ -F_x \\ F_y \\ -F_y \\ 2(u_x F_x - u_y F_y) \\ u_x F_y + u_y F_x \end{bmatrix}, \tag{3.27}$$

where F_x and F_y are the components of the total external force $\mathbf{F}$ determined by Eq. (2.4).

The macroscopic fluid density ρ and velocity $\mathbf{u} = (u_x, u_y)$ can be recovered by Eq. (3.11) and Eq. (3.12) respectively. And for the fluid pressure P under the incompressible approximation [70], it can be determined by using $\rho = \rho_0 + \delta\rho$, and the expression is given by

$$P = \rho c_s^2. \tag{3.28}$$

The model introduced above is the MRT form of a D2Q9 model in Cartesian coordinates based on He. et al.'s forcing scheme [65, 69]. This MRT model is widely adopted to simulate the thermal convective flow, and with certain improvement and modification, this model can be utilized to simulate the flow in asymmetric

coordinates and more complicated flow problems such as the porous thermal flow and solid-liquid phase change. Besides, to minimize the confusion, the author wants to clarify that the shifted density distribution function $\bar{\mathbf{f}}$ in this MRT model is directly obtained through the fluid evolution process of LBM and there is no need to transfer from or to the original $\mathbf{f}$. In other word, there is no difference in the actual solving process of MRT-LBM between $\bar{\mathbf{f}}$ and $\mathbf{f}$. Therefore, the literature sometimes use the term $\mathbf{f}$ instead of $\bar{\mathbf{f}}$ to keep the consistency of the lattice Boltzmann equations.

Additionally, this model utilizes the transition matrix given in Eq. (3.19). Another widely adopted transition matrix is called the non-orthogonal matrix, which is given as [71]

$$M = \begin{bmatrix} 1 & 1 & 1 & 1 & 1 & 1 & 1 & 1 & 1 \\ 0 & 1 & 0 & -1 & 0 & 1 & -1 & -1 & 1 \\ 0 & 0 & 1 & 0 & -1 & 1 & 1 & -1 & -1 \\ 0 & 1 & 1 & 1 & 1 & 2 & 2 & 2 & 2 \\ 0 & 1 & -1 & 1 & -1 & 0 & 0 & 0 & 0 \\ 0 & 0 & 0 & 0 & 0 & 1 & -1 & 1 & -1 \\ 0 & 0 & 0 & 0 & 0 & 1 & 1 & -1 & -1 \\ 0 & 0 & 0 & 0 & 0 & 1 & -1 & -1 & 1 \\ 0 & 0 & 0 & 0 & 0 & 1 & 1 & 1 & 1 \end{bmatrix}. \tag{3.29}$$

By applying this non-orthogonal M, some orders and values change correspondingly for the equilibrium moment vector $\mathbf{m}^{eq}$, the force term $\mathbf{F}_m$ and the relaxation matrix

S. Since it is still based on the same theory, the non-orthogonal model is still very similar to the original one. The detailed settings of those vectors can also be found in Liu et al. [71].

3.1.4 Axisymmetric MRT-LBM for Fluid Field

Generally, there exist two ways to convert the lattice Boltzmann model from Cartesian coordinates to axisymmetric coordinates. One approach is by adding extra source terms while keeping basic lattice functions the same as those in Cartesian coordinates. The other is by modifying the equilibrium distribution functions directly, and thus the moment equilibrium functions and the force term change accordingly.

In the first approach, the basic lattice equations represent the terms that both exist in Cartesian and axisymmetric coordinates, while the extra source terms are utilized to retrieve the terms that appear only in the axisymmetric coordinates. Both the SRT and MRT models based on this theory were proposed by Li et al. [72]. For the MRT D2Q9 model under the assumption of incompressible flow, all the given equations, from Eq. (3.16) to Eq. (3.26), can be used simply by replacing the subscript (x, y) by (r, z) for axisymmetric coordinates. While the extra source term

is added to the force term, as shown below

$$\bar{\mathbf{F}}_m = -\frac{u_r}{r}\mathbf{m}^{eq} + \rho_0 \begin{bmatrix} 0 \\ 6(u_r a_r + u_z a_z) \\ -6(u_r a_r + u_z a_z) \\ a_r \\ -a_r \\ a_z \\ -a_z \\ 2(u_r a_r - u_z a_z) \\ u_r a_z + u_r a_z \end{bmatrix}, \tag{3.30}$$

where the equilibrium moment vector $\mathbf{m}^{eq}$ is in the form of Eq. (3.21) but with (r, z) as its subscript, and a_r, a_z are defined as

$$\begin{aligned} a_r &= -\frac{2v_l u_r}{r^2} + F_r, \\ a_z &= F_z \end{aligned} \tag{3.31}$$

where v_l is the fluid kinematic viscosity, F_r and F_z are the components of the total external force $\mathbf{F}$ in axisymmetric coordinates.

Additional post-collision modification should be made to the 4th and 6th components in the moment space to account for the extra term in axisymmetric coor-

dinates [49], which are given by

$$\bar{m}_3^* = m_3^* - \frac{1}{r}(1-0.5s_v)\delta_t^2\left[(s_e/s_v)m_1^{(1)} + 0.5m_7^{(1)}\right],$$
$$\bar{m}_5^* = m_5^* - \frac{1}{r}(1-0.5s_v)\delta_t^2 m_8^{(1)}, \tag{3.32}$$

where m_3^* and m_5^* are the post-collision values for 4th and 6th moments, $\bar{m}_3^*$ and $\bar{m}_3^*$ are the new values of these two moments after the modification, and $m_1^{(1)}$, $m_7^{(1)}$ and $m_8^{(1)}$ can be calculated by

$$\delta_t m_i^{(1)} = (m_i - m_i^{eq} + 0.5\delta_t \bar{F}_{m,i}), \quad i = 1, 7, 8, \tag{3.33}$$

where m_i is the current value of ith moment (before collision). The macroscopic density and velocity can be obtained as follows:

$$\rho = \sum_i f_i - \frac{\delta_t}{2}\frac{\rho_0 u_r}{r}, \tag{3.34}$$

$$\mathbf{u} = \frac{\sum_i \mathbf{e}_i f_i}{\sum_i f_i + (\delta_t v_l/\rho_0 r^2)\delta_{ir}}, \tag{3.35}$$

where δ_{ir} is equal to one for radial direction (r) and zero for axial direction (z). The calculation of density in Eq. (3.34) requires the value of radial velocity u_r, thus the velocity should be calculated first by Eq. (3.35) and then the density can be obtained by Eq. (3.34) based on the new radial velocity.

The model described above is the one approach for simulating axisymmetric flow. In another approach, the lattice equations are rebuilt to represent the axisym-

metric flow without extra modification. And the model developed by this method can be found in Wang et al. [73]. For the MRT D2Q9 model, the equilibrium distribution functions in Eq. (3.23) are multiplied by the radius r, as given below:

$$f_i^{eq} = \omega_i r\rho + \omega_i r\rho_0 \left[\frac{\mathbf{e}_i \cdot \mathbf{u}}{c_s^2} + \frac{(\mathbf{e}_i \cdot \mathbf{u})^2}{2c_s^4} - \frac{|\mathbf{u}|^2}{2c_s^2}\right]. \tag{3.36}$$

Correspondingly, the expressions of the equilibrium moment vector in Eq. (3.21) are also modified as

$$\begin{aligned} \mathbf{m}^{eq} &= \mathbf{M}\mathbf{f}^{eq} \\ &= r\left[\rho, e^{eq}, \varepsilon^{eq}, j_r, q_r^{eq}, j_z, q_z^{eq}, P_{rr}^{eq}, P_{rz}^{eq}\right]^T, \end{aligned} \tag{3.37}$$

where

$$\begin{aligned} e^{eq} &= -2\rho + 3\rho_0(u_r^2 + u_z^2), \\ \varepsilon^{eq} &= \rho - 3\rho_0(u_r^2 + u_z^2), \\ j_r &= \rho_0 u_r, j_z = \rho_0 u_z, \\ q_r^{eq} &= -\rho_0 u_r, q_z^{eq} = -\rho_0 u_z, \\ p_{rr}^{eq} &= \rho_0(u_r^2 - u_z^2), p_{rz}^{eq} = \rho_0 u_r u_z, \end{aligned} \tag{3.38}$$

and for the forcing term $\mathbf{F}_m$, a modified vector is given by [43]

$$\bar{\mathbf{F}}_m = r\rho_0 \begin{bmatrix} 0 \\ 6(u_r a_r + u_z a_z) \\ -6(u_r a_r + u_z a_z) \\ a_r \\ -a_r \\ a_z \\ -a_z \\ 2(u_r a_r - u_z a_z) \\ u_r a_z + u_r a_z \end{bmatrix}, \tag{3.39}$$

where a_r, a_z are defined as [74]

$$\begin{aligned} a_r &= F_r + \frac{c_s^2}{r}\left[1 - \frac{2(\tau_v - 0.5)\delta_t u_r}{r}\right], \\ a_z &= F_z. \end{aligned} \tag{3.40}$$

The macroscopic density and velocity can then be obtained as follows:

$$\rho = \frac{1}{r}\sum_i f_i, \tag{3.41}$$

$$u_r = \frac{r}{r^2 + c_s^2(\tau_v - 0.5)\delta_t}\left[\frac{\sum_i \mathbf{e}_i f_i}{\rho_0} + \frac{\delta_t}{2} r F_r + \frac{\delta_t}{2} c_s^2\right],$$

$$u_z = r\left[\frac{\sum_i \mathbf{e}_i f_i}{\rho_0} + \frac{\delta_t}{2} r F_z\right]. \tag{3.42}$$

To conclude, the equations from Eq. (3.30) to Eq. (3.35) are developed by adding extra source terms, which can replace the corresponding ones in Section 3.1.3. While the equations from Eq. (3.35) to Eq. (3.42) are developed by modifying the equilibrium distribution functions. They are developed from different points of view, but both ways can handle the convective flow in axisymmetric coordinates.

3.1.5 MRT-LBM for Porous Flow at REV Scale

As discussed in Chapter 1, the porous media can be either modeled at the pore-scale or the REV scale. For the physical size of the flow field as large as the PCM HX, modeling the porous media at the REV scale is more efficient. Following the introduction of MRT-LBM above, the modification of MRT-LBM for the flow field with porous media at the REV scale is provided in this section.

3.1.5.1 Porous MRT-LBM in Cartesian Coordinates

Based on the D2Q9 Cartesian MRT-LBM introduced in Section 3.1.3, the equations of equilibrium moment vector $\mathbf{m}^{eq}$ (3.21, 3.22), equilibrium density distribution functions f_i^{eq} (3.23), forcing term F_m (3.27), and fluid pressure P (3.28) are modified for porous flow. Those equations after the modification are given as

follows:

$$\begin{aligned}\mathbf{m}^{eq} &= \mathbf{M}\mathbf{f}^{eq} \\ &= \left[\rho, e^{eq}, \varepsilon^{eq}, j_x, q_x^{eq}, j_y, q_y^{eq}, P_{xx}^{eq}, P_{xy}^{eq}\right]^T, \end{aligned} \tag{3.43}$$

where

$$\begin{aligned} e^{eq} &= -2\rho + \frac{3\rho_0(u_x^2+u_y^2)}{\phi}, \\ \varepsilon^{eq} &= \rho - \frac{3\rho_0(u_x^2+u_y^2)}{\phi}, \\ j_r &= \rho_0 u_x, j_z = \rho_0 u_y, \\ q_x^{eq} &= -\rho_0 u_x, q_y^{eq} = -\rho_0 u_y, \\ p_{xx}^{eq} &= \frac{\rho_0(u_x^2-u_y^2)}{\phi}, p_{xy}^{eq} = \frac{\rho_0 u_x u_y}{\phi}, \end{aligned} \tag{3.44}$$

$$f_i^{eq} = \omega_i\rho + \omega_i\rho_0\left[\frac{\mathbf{e}_i\cdot\mathbf{u}}{c_s^2} + \frac{(\mathbf{e}_i\cdot\mathbf{u})^2}{2\phi c_s^4} - \frac{|\mathbf{u}|^2}{2\phi c_s^2}\right], \tag{3.45}$$

$$\mathbf{F}_m = \rho_0\begin{bmatrix} 0 \\ 6(u_xF_x+u_yF_y)/\phi \\ -6(u_xF_x+u_yF_y)/\phi \\ F_x \\ -F_x \\ F_y \\ -F_y \\ 2(u_xF_x-u_yF_y)/\phi \\ (u_xF_y+u_yF_x)/\phi \end{bmatrix}, \tag{3.46}$$

$$P = \frac{\rho c_s^2}{\phi}. \tag{3.47}$$

Moreover, the calculation of the macroscopic velocity $\mathbf{u}$ needs special treatment because of the presence of porous media. For the porous convective flow at the REV scale, the total external force $\mathbf{F}$ can be expressed as Eq. (2.12) in Chapter 2, which needs to be used in the calculation of the macroscopic velocity as specified in Eq. (3.12) for D2Q9 MRT model. Unlike the convective flow without porous media, where the total external force only contains the gravity as given in Eq. (2.4), the porous flow, however, has the drag forces between the fluid and the porous structures, which are velocity-dependent as expressed by Eq. (2.12). Such a dependency causes Eq. (3.12) to be implicit, which requires further treatment. According to the method proposed by Guo and Zhao [75], the macroscopic velocity $\mathbf{u}$ can be explicitly solved by

$$\mathbf{u} = \frac{\mathbf{v}}{d_0 + \sqrt{d_0^2 + d_1|\mathbf{v}|}}, \tag{3.48}$$

where d_0 and d_1 are given by

$$d_0 = \frac{1}{2}\left[1 + \phi\frac{\delta_t}{2}\frac{v_l}{K}\right], \tag{3.49}$$

$$d_1 = \phi\frac{\delta_t}{2}\frac{C}{\sqrt{K}}, \tag{3.50}$$

where the inertial coefficient C and the permeability K are defined in Eq. (2.17) and Eq. (2.18) from Chapter 2.

And the temporal velocity $\mathbf{v}$ in Eq. (3.48) is defined as

$$\mathbf{v} = \sum_{i=0}^{8} \mathbf{e}_i f_i / \rho_0 + \frac{\delta_t}{2} \phi \mathbf{G}. \tag{3.51}$$

3.1.5.2 Porous MRT-LBM in Axisymmetric Coordinates

Two D2Q9 MRT-LBM models for axisymmetric coordinates introduced in Section 3.1.4 are developed based on the different concepts. Based on the one proposed by Wang et al. [73], Liu et al. [43] developed a porous axisymmetric MRT-LBM at REV scale, which modifies the equations (3.36, 3.37, 3.38, 3.39) as follows:

$$f_i^{eq} = \omega_i r \rho + \omega_i r \rho_0 \left[\frac{\mathbf{e}_i \cdot \mathbf{u}}{c_s^2} + \frac{(\mathbf{e}_i \cdot \mathbf{u})^2}{2c_s^4} - \frac{|\mathbf{u}|^2}{2c_s^2} \right]. \tag{3.52}$$

$$\begin{aligned} \mathbf{m}^{eq} &= \mathbf{M}\mathbf{f}^{eq} \\ &= r \left[\rho, e^{eq}, \varepsilon^{eq}, j_r, q_r^{eq}, j_z, q_z^{eq}, P_{rr}^{eq}, P_{rz}^{eq} \right]^T, \end{aligned} \tag{3.53}$$

where

$$\begin{aligned} e^{eq} &= -2\rho + \frac{3\rho_0(u_r^2 + u_z^2)}{\phi}, \\ \varepsilon^{eq} &= \rho - \frac{3\rho_0(u_r^2 + u_z^2)}{\phi}, \\ j_r &= \rho_0 u_r, j_z = \rho_0 u_z, \\ q_r^{eq} &= -\rho_0 u_r, q_z^{eq} = -\rho_0 u_z, \\ p_{rr}^{eq} &= \frac{\rho_0(u_r^2 - u_z^2)}{\phi}, p_{rz}^{eq} = \frac{\rho_0 u_r u_z}{\phi}, \end{aligned} \tag{3.54}$$

and

$$\bar{\mathbf{F}}_m = r\rho_0 \begin{bmatrix} 0 \\ 6(u_r a_r + u_z a_z)/\phi \\ -6(u_r a_r + u_z a_z)/\phi \\ a_r \\ -a_r \\ a_z \\ -a_z \\ 2(u_r a_r - u_z a_z)/\phi \\ (u_r a_z + u_r a_z)/\phi \end{bmatrix}. \tag{3.55}$$

Other than the modifications above, the velocity calculation also needs special treatment because of the same reason as mentioned in Section 3.1.5.1 for the Cartesian porous model. The explicit method to calculate the macroscopic velocity $\mathbf{u}$ in axisymmetric coordinates is given as

$$\mathbf{u} = \frac{\mathbf{v}}{\mathbf{d}_0 + \sqrt{\mathbf{d}_0^2 + d_1|\mathbf{v}|}}, \tag{3.56}$$

where $\mathbf{d}_0 = (d_{0r}, d_{0z})$ and d_1 are given by

$$d_{0r} = \frac{1}{2}\left[\frac{r^2 + c_s^2(s_v^{-1} - 0.5)\delta_t}{r} + r\phi\frac{\delta_t}{2}\frac{v_l}{K}\right], \tag{3.57}$$

$$d_{0z} = \frac{r}{2}\left(1 + \phi\frac{\delta_t}{2}\frac{v_l}{K}\right), \tag{3.58}$$

$$d_1 = r\phi\frac{\delta_t}{2}\frac{C}{\sqrt{K}}, \tag{3.59}$$

and $\mathbf{v} = (v_r, v_z)$ is a temporal velocity defined as

$$\begin{aligned} v_r &= \frac{1}{\rho_0}\sum_{i=0}^{8} e_{ir} f_i + \frac{\delta_t}{2} c_s^2, \\ v_z &= \frac{1}{\rho_0}\sum_{i=0}^{8} e_{iz} f_i + \frac{\delta_t}{2} r\phi G_z. \end{aligned} \tag{3.60}$$

Additionally, the fluid pressure is calculated in the same way as Eq. (3.47) in Section 3.1.5.1.

3.2 Single-Phase Lattice Boltzmann Models for Temperature Field

From Section 3.1 in this chapter, the single-phase lattice Boltzmann models for fluid flow are demonstrated. However, they are only for isothermal flow. Although the external force from Eq. (2.4) and Eq. (2.12) based on Boussinesq approximation can be brought into the forcing term $\mathbf{F}_m$, the evolution of the temperature field must be solved because the temperature difference is considered in the calculation of the buoyancy force.

The simulation of heat transfer can be carried out using either a conventional CFD or LBM. The former is called hybrid LBM, which uses isothermal LBM for fluid flow and solves the temperature field separately using either FVM or FDM [76,77]. While for the latter one, solving the temperature via LBM, the most popular approach in LBM is called the double-distribution-function (DDF) method, as it has

more numerical stability and versatility than other methods in thermal LBM [9].

The very basic DDF-LBM is free of the heat source term [78, 79]. So it is not sufficient to solve thermal flow with heat source or PCM phase change. The basic DDF-LBM and its MRT form thereby are only briefly introduced in this section, while a detailed introduction is made to the DDF-LBM with the heat source treatment in Chapter 4.

So in this section, the energy side of DDF-LBM is introduced in Section 3.2.1, and the MRT scheme of the thermal lattice Boltzmann models is discussed in Section 3.2.2

3.2.1 Double-Distribution-Function (DDF) Approach

Various DDF-LBM have been devised to model the single-phase flow with temperature variations [42], while the key feature of DDF-LBM is to establish a discrete energy equation in the similar form with Eq. (3.1) but solving the energy distribution functions $\mathbf{g}(\mathbf{x}, t)$ instead. The heat transfer can be simulated by solving the discrete energy equation in the same way as solving the discrete Boltzmann equation for fluid flow. The general discrete energy equation in DDF-LBM can be described as

$$\mathbf{g}(\mathbf{x} + \mathbf{e}\delta_t, t + \delta_t) - \mathbf{g}(\mathbf{x}, t) = -\frac{1}{\tau_g}\left[\mathbf{g}(\mathbf{x}, t) - \mathbf{g}^{eq}(\mathbf{x}, t)\right], \tag{3.61}$$

where τ_g is the relaxation time for the energy equation, and $\mathbf{g}^{eq}$ are the equilibrium energy distribution functions.

Depending on the recovered macroscopic energy equation, the thermal DDF-LBM can either be temperature-based or enthalpy-based. For temperature-based DDF, the temperature T can be recovered from the distribution functions g_i, given by

$$T = \sum_i g_i, \tag{3.62}$$

while for enthalpy-based DDF, the enthalpy h is what solved in LBM, as shown below

$$h = \sum_i g_i. \tag{3.63}$$

3.2.2 Thermal MRT Lattice Boltzmann Schemes

DDF-MRT models have been attractive in the past decade owing to their versatility and numerical stability [9]. DDF-MRT models have been developed either based on temperature or enthalpy. In this section, two commonly adopted DDf-MRT models are introduced. One is D2Q5 temperature-based DDF-MRT model [9, 51] and the other one is D2Q9 enthalpy-based DDF-MRT model [59].

3.2.2.1 D2Q5 Temperature-Based DDF-MRT Model

As its name suggests, D2Q5 model only has 5 velocity directions in one lattice structure, as Fig. 3.3 shows. The corresponding MRT energy equation is given by

$$\mathbf{g}(\mathbf{x} + \mathbf{e}\delta_t, t + \delta_t) - \mathbf{g}(\mathbf{x}, t) = -\mathbf{N}^{-1}\mathbf{R}\left[\mathbf{n}(\mathbf{x}, t) - \mathbf{n}^{eq}(\mathbf{x}, t)\right], \tag{3.64}$$

where $\mathbf{n}(\mathbf{x}, t)$ and $\mathbf{n}^{eq}(\mathbf{x}, t)$ are the moment vector and the equilibrium moment vector, corresponding to $\mathbf{g}(\mathbf{x}, t)$ respectively.

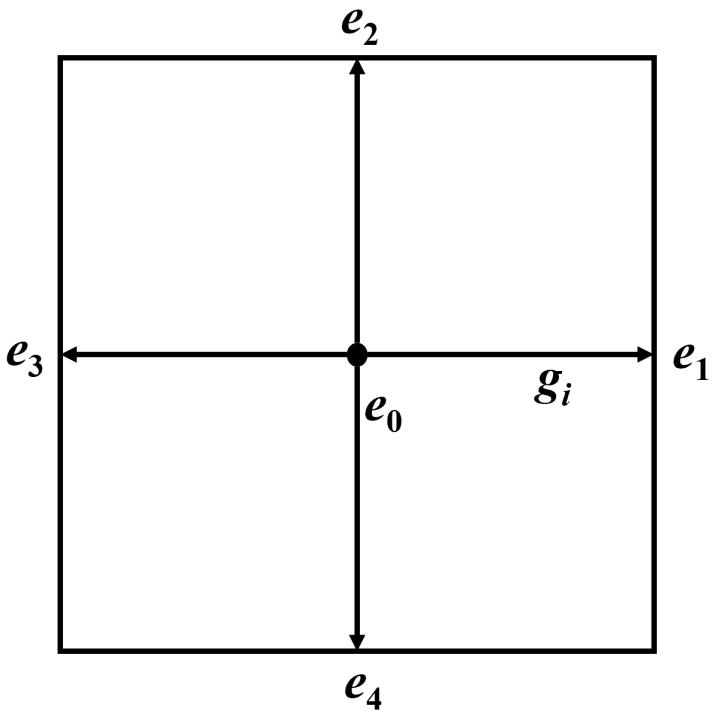

Figure 3.3: D2Q5 lattice structure.

The transition matrix $\mathbf{N}$ is defined as

$$N = \begin{bmatrix} 1 & 1 & 1 & 1 & 1 \\ 0 & 1 & 0 & -1 & 0 \\ 0 & 0 & 1 & 0 & -1 \\ -4 & 1 & 1 & 1 & 1 \\ 0 & 1 & -1 & 1 & -1 \end{bmatrix}, \tag{3.65}$$

based on which the equilibrium moment vector $\mathbf{n}^{eq}$ is defined as

$$\begin{aligned}\mathbf{n}^{eq} &= \mathbf{N}\mathbf{g}^{eq} \\ &= \begin{bmatrix} T,\ u_x T,\ u_y T,\ \bar{\omega} T,\ 0 \end{bmatrix}^T,\end{aligned} \tag{3.66}$$

where $\bar{\omega}$ is a constant of the D2Q5 model which can be set between -4 and 1, and the equilibrium distribution function g_i^{eq} is given by

$$g_i^{eq} = \tilde{\omega}_i T(1 + \frac{\mathbf{e}_i \cdot \mathbf{u}}{c_{sT}^2}), \tag{3.67}$$

where the c_{sT} is the lattice sound speed of D2Q5 model, which is different from that in D2Q9. It can be calculated from the equation $c_{sT}^2 = (4 + \bar{\omega})c^2/10$, where the lattice speed is commonly set to $c = \delta_x/\delta_t = 1$ in LBM.

The weight coefficients $\tilde{\omega}_i$ are given as

$$\tilde{\omega}_i = \begin{cases} (1 - \bar{\omega})/5, & i = 0, \\ (4 + \bar{\omega})/20, & i = 1, 2, 3, 4, \end{cases} \tag{3.68}$$

and the macroscopic temperature T can be calculated with Eq. (3.62).

3.2.2.2 D2Q9 Enthalpy-Based DDF-MRT Model

As its name suggests, the lattice structure and velocity directions are the same as Fig. 3.2 shows. The MRT governing equation is in the same form as Eq. (3.64), but with nine velocity directions instead of five ones.

The transition matrix is the same as the one in the MRT model for fluid flow, which is given in Eq. (3.19). The equilibrium moment vector $\mathbf{n}^{eq}$ can then be defined as

$$\begin{aligned}\mathbf{n}^{eq} &= \mathbf{N}\mathbf{g}^{eq} \\ &= \Bigg[h, -4h + 2c_pT + \frac{3c_pT|\mathbf{u}|^2}{c^2}, 4h - 3c_pT - \frac{3c_pT|\mathbf{u}|^2}{c^2}, \\ &\frac{c_pTu_x}{c}, -\frac{c_pTu_x}{c}, \frac{c_pTu_y}{c}, -\frac{c_pTu_y}{c}, \frac{c_pT(u_x^2 - u_y^2)}{c^2}, \frac{c_pTu_xu_y}{c^2}\Bigg],\end{aligned} \tag{3.69}$$

where the vector of the equilibrium distribution functions $\mathbf{g}^{eq} = \{g_i^{eq} | i = 0, 1, ..., 8\}$ is given by

$$g_i^{eq} = \begin{cases} h - c_pT + \omega_i c_pT - \omega_i c_pT \dfrac{|\mathbf{u}|^2}{2c_s^2}, & i = 0, \\ \omega_i c_pT \left[1 + \dfrac{(\mathbf{e}_i \cdot \mathbf{u})}{c_s^2} + \dfrac{(\mathbf{e}_i \cdot \mathbf{u})^2}{2c_s^4} - \dfrac{|\mathbf{u}|^2}{2c_s^2}\right], & i \neq 0, \end{cases} \tag{3.70}$$

where the weight coefficient ω_i is the same as that in Eq. (3.4). And it is the enthalpy solved by this model, which can be calculated by Eq. (3.63).

3.3 Other DmQn Lattice Boltzmann Models

For two-dimensional cases, the D2Q9 model is widely adopted for simulating the flow field, and both D2Q5 and D2Q9 models are commonly utilized in solving the temperature field. The example models for both D2Q9 and D2Q5 are provided in the previous sections of this chapter.

While for three-dimensional cases, the widely adopted models for the fluid field

are D3Q15 and D3Q19 LBM [9], and a thermal LBM based on D3Q7 [80] can be used to solve for heat transfer in 3D. In this section, D3Q15 and D3Q19 for fluid flow and D3Q7 for heat transfer are briefly introduced.

3.3.1 D3Q15 SRT-LBM for Fluid Field

For the D3Q15 lattice model, the lattice Boltzmann equation, equilibrium density distribution functions and calculations of macroscopic properties are in the same form with Eq. (3.1), Eq. (3.3), Eq. (3.7) and Eq. (3.8) in Section 3.1.1. Based on the lattice structure shown in Fig. 3.4, the discrete velocities **e** can be given by

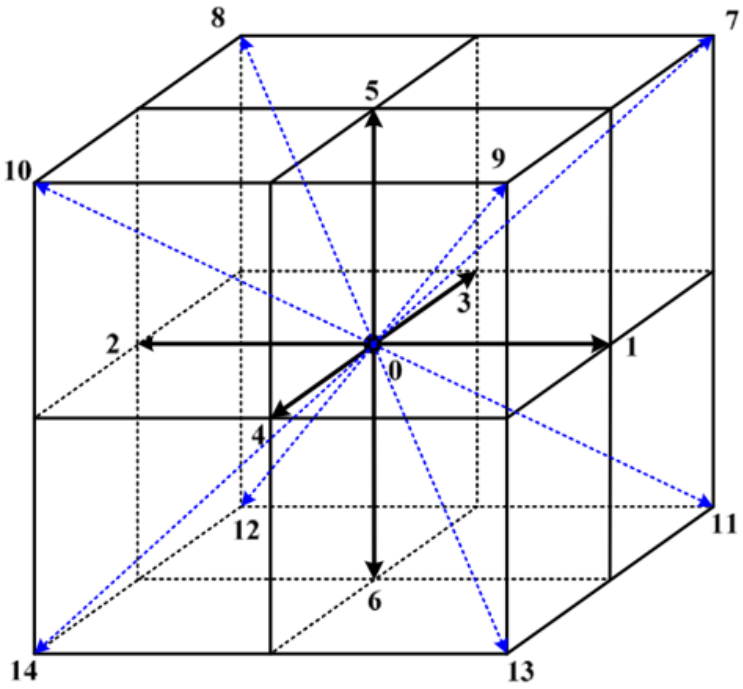

Figure 3.4: D3Q15 lattice structure [9].

$$\mathbf{e} = \begin{bmatrix} \begin{pmatrix} 0 \\ 0 \\ 0 \end{pmatrix} & \begin{pmatrix} 1 \\ 0 \\ 0 \end{pmatrix} & \begin{pmatrix} -1 \\ 0 \\ 0 \end{pmatrix} & \begin{pmatrix} 0 \\ 1 \\ 0 \end{pmatrix} & \begin{pmatrix} 0 \\ -1 \\ 0 \end{pmatrix} & \begin{pmatrix} 0 \\ 0 \\ 1 \end{pmatrix} & \begin{pmatrix} 0 \\ 0 \\ -1 \end{pmatrix} & \begin{pmatrix} 1 \\ 1 \\ 1 \end{pmatrix} \\ \begin{pmatrix} -1 \\ 1 \\ 1 \end{pmatrix} & \begin{pmatrix} 1 \\ -1 \\ 1 \end{pmatrix} & \begin{pmatrix} -1 \\ -1 \\ 1 \end{pmatrix} & \begin{pmatrix} 1 \\ 1 \\ -1 \end{pmatrix} & \begin{pmatrix} -1 \\ 1 \\ -1 \end{pmatrix} & \begin{pmatrix} 1 \\ -1 \\ -1 \end{pmatrix} & \begin{pmatrix} -1 \\ -1 \\ -1 \end{pmatrix} \end{bmatrix}, \tag{3.71}$$

and the weight coefficients are

$$\omega_i = \begin{cases} \frac{2}{9}, & i = 0, \\ \frac{1}{9}, & i = 1 \sim 6, \\ \frac{1}{72}, & i = 7 \sim 14. \end{cases} \tag{3.72}$$

3.3.2 D3Q19 MRT-LBM for Fluid Field

D3Q19 lattice model has more velocity directions than the D3Q15 model, as shown in Fig. 3.5. The basic SRT settings are almost the same as those in the D3Q15 model. The only differences are for discrete velocities $\mathbf{e}$ and the weight functions ω_i,

which are defined as follows:

$$\mathbf{e} = \begin{bmatrix} \begin{pmatrix}0\\0\\0\end{pmatrix} & \begin{pmatrix}1\\0\\0\end{pmatrix} & \begin{pmatrix}-1\\0\\0\end{pmatrix} & \begin{pmatrix}0\\1\\0\end{pmatrix} & \begin{pmatrix}0\\-1\\0\end{pmatrix} & \begin{pmatrix}0\\0\\1\end{pmatrix} & \begin{pmatrix}0\\0\\-1\end{pmatrix} & \begin{pmatrix}1\\1\\0\end{pmatrix} & \begin{pmatrix}-1\\1\\0\end{pmatrix} & \begin{pmatrix}1\\-1\\0\end{pmatrix} \\ \begin{pmatrix}-1\\-1\\0\end{pmatrix} & \begin{pmatrix}1\\0\\1\end{pmatrix} & \begin{pmatrix}-1\\0\\1\end{pmatrix} & \begin{pmatrix}1\\0\\-1\end{pmatrix} & \begin{pmatrix}-1\\0\\-1\end{pmatrix} & \begin{pmatrix}0\\1\\1\end{pmatrix} & \begin{pmatrix}0\\-1\\1\end{pmatrix} & \begin{pmatrix}0\\1\\-1\end{pmatrix} & \begin{pmatrix}0\\-1\\-1\end{pmatrix} \end{bmatrix}, \tag{3.73}$$

$$\omega_i = \begin{cases} \frac{1}{3}, & i = 0, \\ \frac{1}{18}, & i = 1 \sim 6, \\ \frac{1}{36}, & i = 7 \sim 18. \end{cases} \tag{3.74}$$

A D3Q19 MRT model developed based on the SRT model by d'Humières [81] is then introduced in this section. The evolution process is still governed by Eq. (3.16), but the transition matrix is replaced by a 19×19 matrix, as shown below

$$M = \begin{bmatrix} 1 & 1 & 1 & 1 & 1 & 1 & 1 & 1 & 1 & 1 & 1 & 1 & 1 & 1 & 1 & 1 & 1 & 1 & 1 \\ -30 & -11 & -11 & -11 & -11 & -11 & -11 & 8 & 8 & 8 & 8 & 8 & 8 & 8 & 8 & 8 & 8 & 8 & 8 \\ 12 & -4 & -4 & -4 & -4 & -4 & -4 & 1 & 1 & 1 & 1 & 1 & 1 & 1 & 1 & 1 & 1 & 1 & 1 \\ 0 & 1 & -1 & 0 & 0 & 0 & 0 & 1 & -1 & 1 & -1 & 1 & -1 & 1 & -1 & 0 & 0 & 0 & 0 \\ 0 & -4 & 4 & 0 & 0 & 0 & 0 & 1 & -1 & 1 & -1 & 1 & -1 & 1 & -1 & 0 & 0 & 0 & 0 \\ 0 & 0 & 0 & 1 & -1 & 0 & 0 & 1 & 1 & -1 & -1 & 0 & 0 & 0 & 0 & 1 & -1 & 1 & -1 \\ 0 & 0 & 0 & -4 & 4 & 0 & 0 & 1 & 1 & -1 & -1 & 0 & 0 & 0 & 0 & 1 & -1 & 1 & -1 \\ 0 & 2 & 2 & -1 & -1 & -1 & -1 & 1 & 1 & 1 & 1 & 1 & 1 & 1 & 1 & -2 & -2 & -2 & -2 \\ 0 & -4 & -4 & 2 & 2 & 2 & 2 & 1 & 1 & 1 & 1 & 1 & 1 & 1 & 1 & -2 & -2 & -2 & -2 \\ 0 & 0 & 0 & 1 & 1 & -1 & -1 & 1 & 1 & 1 & 1 & -1 & -1 & -1 & -1 & 0 & 0 & 0 & 0 \\ 0 & 0 & 0 & -2 & -2 & 2 & 2 & 1 & 1 & 1 & 1 & -1 & -1 & -1 & -1 & 0 & 0 & 0 & 0 \\ 0 & 0 & 0 & 0 & 0 & 0 & 0 & 1 & -1 & -1 & 1 & 0 & 0 & 0 & 0 & 0 & 0 & 0 & 0 \\ 0 & 0 & 0 & 0 & 0 & 0 & 0 & 0 & 0 & 0 & 0 & 0 & 0 & 0 & 0 & 1 & -1 & -1 & 1 \\ 0 & 0 & 0 & 0 & 0 & 0 & 0 & 0 & 0 & 0 & 0 & 1 & -1 & -1 & 1 & 0 & 0 & 0 & 0 \\ 0 & 0 & 0 & 0 & 0 & 0 & 0 & 1 & -1 & 1 & -1 & -1 & 1 & -1 & 1 & 0 & 0 & 0 & 0 \\ 0 & 0 & 0 & 0 & 0 & 0 & 0 & -1 & -1 & 1 & 1 & 0 & 0 & 0 & 0 & 1 & -1 & 1 & -1 \\ 0 & 0 & 0 & 0 & 0 & 0 & 0 & 0 & 0 & 0 & 0 & 1 & 1 & -1 & -1 & -1 & -1 & 1 & 1 \end{bmatrix}, \tag{3.75}$$

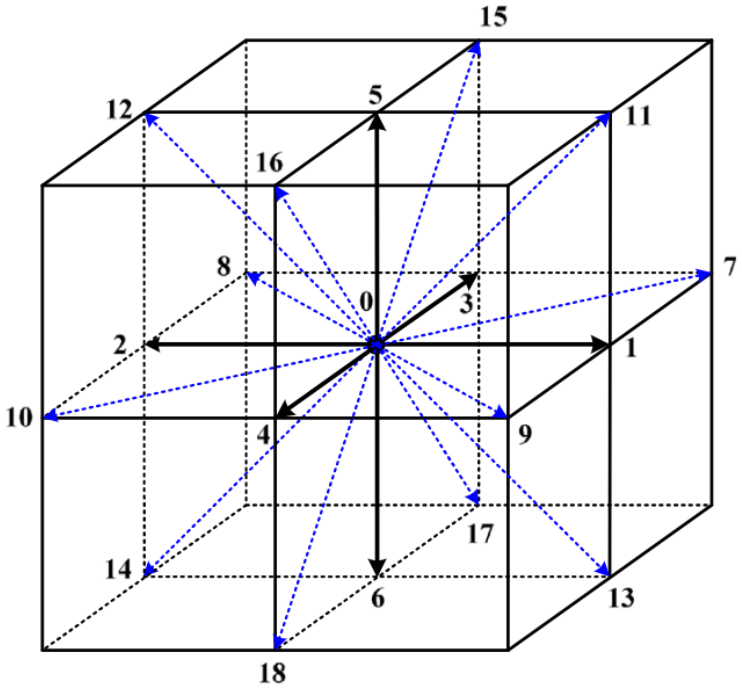

Figure 3.5: D3Q19 lattice structure [9].

based on which the equilibrium moment vector $\mathbf{m}^{eq}$ can be defined as

$$\begin{aligned}\mathbf{m}^{eq} =& \mathbf{M}\mathbf{f}^{eq} \\ =& \rho\Big[1, -11+19\mathbf{u}^2, 3-\frac{11\mathbf{u}^2}{2}, u_x, -\frac{2u_x}{3}, u_y, -\frac{2u_y}{3}, u_z, -\frac{2u_z}{3}, 3u_x^2-\mathbf{u}^2, \\ & -u_x^2+0.5(u_y^2+u_z^2), u_y^2-u_z^2, u_z^2-u_y^2, u_xu_y, u_yu_z, u_z, u_x, 0, 0, 0\Big]^T, \end{aligned} \tag{3.76}$$

and the forcing term in the moment space can be described as

$$\begin{aligned}\mathbf{F}_m = \Big[& 0,\ 38\mathbf{F}\cdot\mathbf{u}, -11\mathbf{F}\cdot\mathbf{u}, F_x, -\frac{2F_x}{3}, F_y, -\frac{2F_y}{3}, F_z, -\frac{2F_z}{3}, 6F_xu_x-2\mathbf{F}\cdot\mathbf{u}, \\ & \mathbf{F}\cdot\mathbf{u}-3F_xu_x, 2F_yu_y-2F_zu_z, F_zu_z-F_yu_y, F_xu_y+F_yu_x, \\ & F_yu_z+F_zu_y, F_xu_z+F_zu_x, 0, 0, 0\Big]^T. \end{aligned} \tag{3.77}$$

Besides, the relaxation matrix $\mathbf{S}$ is given by

$$\mathbf{S} = diag(0, s_e, s_\varepsilon, 0, s_q, 0, s_q, 0, s_q, s_v, s_\pi, s_v, s_\pi, s_v, s_v, s_v, s_t, s_t, s_t), \tag{3.78}$$

where s_v and s_e are related to fluid kinematic viscosity v_l and bulk viscosity ζ_l, described as

$$v_l = \frac{1}{3}(\frac{1}{s_v} - 0.5)\delta_t c^2, \qquad \zeta_l = \frac{2}{9}(\frac{1}{s_e} - 0.5)\delta_t c^2. \tag{3.79}$$

More details for D3Q19 MRT model can also be found in Premnath et. al [82].

3.3.3 D3Q7 MRT-LBM for Temperature Field

The lattice structure of D3Q7 is shown in Fig. 3.6.

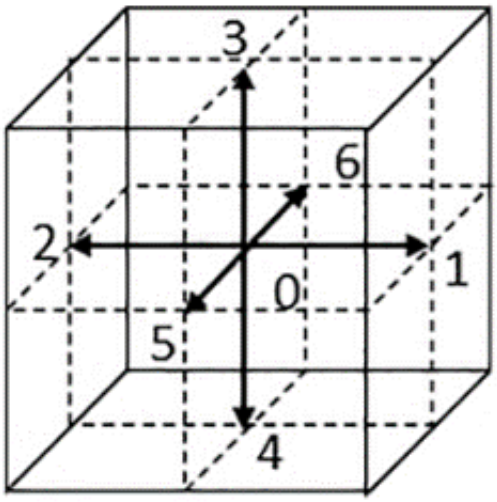

Figure 3.6: D3Q7 lattice structure [10].

The evolution process of D3Q7 MRT-LBM is still governed by Eq. (3.64), with

the transformation matrix defined as [83]

$$N = \begin{bmatrix} 1 & 1 & 1 & 1 & 1 & 1 & 1 \\ 0 & 1 & -1 & 0 & 0 & 0 & 0 \\ 0 & 0 & 0 & 1 & -1 & 0 & 0 \\ 0 & 0 & 0 & 0 & 0 & 1 & -1 \\ 6 & -1 & -1 & -1 & -1 & -1 & -1 \\ 0 & 2 & 2 & -1 & -1 & -1 & -1 \\ 0 & 0 & 0 & 1 & 1 & -1 & -1 \end{bmatrix}, \tag{3.80}$$

by which the equilibrium moment vector $\mathbf{n}^{eq}$ can be expressed as

$$\begin{aligned} \mathbf{n}^{eq} =& \mathbf{N} g^{eq} \\ =& \left[h, c_p T u_x, c_p T u_y, c_p T u_z, 6h - 21\omega_T c_{p,ref} T, 0, 0\right]. \end{aligned} \tag{3.81}$$

The discrete velocities for D3Q7 are given by,

$$\mathbf{e} = \begin{bmatrix} \begin{pmatrix} 0 \\ 0 \\ 0 \end{pmatrix} & \begin{pmatrix} 1 \\ 0 \\ 0 \end{pmatrix} & \begin{pmatrix} -1 \\ 0 \\ 0 \end{pmatrix} & \begin{pmatrix} 0 \\ 1 \\ 0 \end{pmatrix} & \begin{pmatrix} 0 \\ -1 \\ 0 \end{pmatrix} & \begin{pmatrix} 0 \\ 0 \\ 1 \end{pmatrix} & \begin{pmatrix} 0 \\ 0 \\ -1 \end{pmatrix} \end{bmatrix}, \tag{3.82}$$

and the equilibrium distribution functions are defined as

$$g_i^{eq} = \begin{cases} h - c_{p,ref}T + \omega_i c_{p,ref}T, & i = 0, \\ \\ \omega_i c_{p,ref}T + \dfrac{\mathbf{u}\cdot\mathbf{e}_i}{c_{sT}^2}\omega_i c_p T & i \neq 0, \end{cases} \tag{3.83}$$

where the weight functions ω_i can be calculated by

$$\omega_i = \begin{cases} 1 - 3\omega_T, & i = 0, \\ \\ 0.5\omega_T, & i \neq 0, \end{cases} \tag{3.84}$$

where ω_T is a constant between 0 and 1, by which the sound speed c_{sT} in D3Q7 is determined as $c_{sT} = (\omega_t)^{1/2}c$. Finally the enthalpy can be recovered by Eq. (3.63).

3.4 Chapter Summary

In this chapter, various single-phase lattice Boltzmann models are introduced, either for the flow field (Section 3.1) or for the temperature field (Section 3.2). Generally, lattice Boltzmann models can be characterized by their lattice structures (DmQn). Besides the models demonstrated in Section 3.1 and Section 3.2, other DmQn models are introduced in Section 3.3, including the three-dimensional lattice Boltzmann models.

In order to facilitate the indexing of the models introduced in this chapter, Table 3.1 summarizes all the mentioned models based on their lattice structures

(DmQn) and sorts them in the sequence of ascending values of m (dimensions) and n (numbers of discrete velocities).

Lattice structures	Lattice Boltzmann models	Sections
D2Q5	Temperature-based DDF-MRT	Section 3.2.2.1
D2Q9	LBGK (SRT)	Section 3.1.1
	Cartesian MRT	Section 3.1.3
	Axisymmetric MRT	Section 3.1.4
	Cartesian Porous MRT	Section 3.1.5.1
	Axisymmetric Porous MRT	Section 3.1.5.2
	Enthalpy-based DDF-MRT	Section 3.2.2.2
D3Q7	Enthalpy-based DDF-MRT	Section 3.3.3
D3Q15	Cartesian SRT	Section 3.3.1
D3Q19	Cartesian MRT	Section 3.3.2

Table 3.1: Summary of Single-Phase Lattice Boltzmann Models in Chapter 3.

Chapter 4: Solid-Liquid Lattice Boltzmann Models

In Chapter 3, the focus is on single-phase LBM for the flow field, as it is sufficient to solve the fluid flow in the liquid zone of the PCM phase change. In this chapter, the solid-liquid lattice Boltzmann models are developed, applying a single-phase LBM to the flow field in the liquid zone and an improved thermal LBM to the temperature field in the entire domain. The focus of this chapter is on the thermal side of the solid-liquid DDF-LBM.

4.1 Treatment of Latent Heat

Generally, the consideration of latent heat can be either by modeling the variation of specific heat capacity or by adding a heat source term. In solid-liquid LBM, treating the latent heat as a heat source term is easier to achieve in terms of the model development, and thus is widely used.

In Chapter 3, two thermal MRT models (D2Q5 and D2Q9) are introduced in Section 3.2.2 for Cartesian coordinates, which are free of heat source terms, i.e., single-phase thermal MRT-LBM. Between them, the D2Q9 enthalpy-based MRT-LBM can be directly used in solving solid-liquid phase change by modeling the enthalpy h based on the equations proposed in Section 2.5.1, while the D2Q5

temperature-based MRT-LBM needs to add a latent heat source term to the thermal lattice Boltzmann equation (3.64), which is then given as

$$\mathbf{g}(\mathbf{x}+\mathbf{e}\delta_t,t+\delta_t)-\mathbf{g}(\mathbf{x},t)=-\mathbf{N}^{-1}\mathbf{R}\left[\mathbf{n}(\mathbf{x},t)-\mathbf{n}^{eq}(\mathbf{x},t)\right]+\delta_t\mathbf{N}^{-1}\mathbf{Q}_m, \tag{4.1}$$

where $\mathbf{Q}_m$ is the latent heat source term in the moment space, which is given by [51]

$$\mathbf{Q}_m=\left(-\frac{L_a\Delta f_l}{c_{p,l}\delta_t}\ ,\ 0\ ,\ 0\ ,\ \ -\bar{\omega}\frac{L_a\Delta f_l}{c_{p,l}\delta_t}\ ,\ 0\right), \tag{4.2}$$

where $\bar{\omega}$ is a constant in D2Q5 which can be set between -4 and 1, and the change of liquid fraction Δf_l can be obtained by a forward finite difference scheme given as $\Delta f_l = f_l(\mathbf{x},t+\delta_t)-f_l(\mathbf{x},t)$.

Similar to the models for the flow field in Section 3.1.3, the collision process of the thermal models executed in the moment space can be expressed as

$$\mathbf{n}^*(\mathbf{x},t)=\mathbf{n}(\mathbf{x},t)-\mathbf{R}\left[\mathbf{n}(\mathbf{x},t)-\mathbf{n}^{eq}(\mathbf{x},t)\right]+\delta_t\mathbf{Q}_m, \tag{4.3}$$

and the streaming process that calculates based on the distribution functions is given as

$$g(\mathbf{x}+\mathbf{e}\delta_t,t+\delta_t)=\mathbf{N}^{-1}\mathbf{n}^*(\mathbf{x},t). \tag{4.4}$$

Although this D2Q5 model is based on temperature, the relationship between the liquid fraction f_l and the temperature T is determined by the enthalpy method. The forward scheme of Δf_l in the heat source term, which is required for solving the

temperature field, is also dependent on the temperature. Therefore, iterations are necessary for solving the evolution equation at every time step of temperature-based LBM to obtain the temperature field [47]. This limitation increases the computation costs and thus makes it less competitive than the enthalpy-based LBM in solving the solid-liquid phase change. In the following sections of this chapter, emphasis is placed on introducing the development of enthalpy-based thermal MRT-LBM.

4.2 Porous Media Treatments

As mentioned in latent heat treatments (Section 4.1), the D2Q9 enthalpy-based MRT-LBM in Section 3.2.2.2 can be directly used in solving solid-liquid phase change by modeling the enthalpy h based on the equations proposed in Section 2.5.1. In general, the enthalpy-based MRT-LBM can solve either single-phase or solid-liquid heat transfer by setting corresponding enthalpy equations. For porous PCM phase change at the REV scale, the enthalpy equations consider the porous media by applying the porosity ϕ as specified in Section 2.5.1. Besides, the relaxation time τ_g for the energy equation is calculated based on the effective thermal diffusivity α_e defined in Section 2.3, e.g., the relaxation matrix $\mathbf{R}$ is defined as

$$\mathbf{R} = diag(\sigma_h, \sigma_e, \sigma_\varepsilon, \sigma_j, \sigma_q, \sigma_j, \sigma_q, \sigma_p, \sigma_p), \tag{4.5}$$

where σ_h is set to 1.0 representing the energy is conserved, and the critical relaxation rate σ_j, which determines the heat transfer behavior, is related to the effective

thermal diffusivity α_e and can be expressed as

$$\sigma_j = \frac{1}{\tau_g}, \tag{4.6}$$

$$\tau_g = \frac{\alpha_e}{c_s^2 \delta_t} + 0.5, \tag{4.7}$$

where the effective thermal diffusivity is defined as $\alpha_e = k_e/(\rho_l c_p)$ with the effective thermal conductivity k_e solved by Eq. (2.19), where the thermal conductivity of the PCM (k_f) can be determined by

$$k_f = f_l k_l + (1 - f_l) k_s. \tag{4.8}$$

If the referenced specific heat $c_{p,ref}$ specified in Section 2.6 is used for the calculation of the thermal diffusivity. The effective thermal diffusivity is then re-defined as $\alpha_e = k_e/(\rho_l c_{p,ref})$. For pure PCM, the thermal conductivity between solid and liquid phases may differ. However, this difference is minimized for the effective thermal conductivity between the two phases, and therefore is negligible when the thermal conductivity of porous media ($k_{p,m}$) is high enough compared with those of the PCM (k_s and k_l). If this difference can not be ignored in some cases, another simplification can be made by assuming two effective thermal conductivities ($k_{e,s}$ and $k_{e,l}$) for both phases respectively, and neglecting the thermal conductivity variations in the mushy zone ($0 < f_l < 1$).

4.3 Axisymmetric Thermal MRT-LBM

The adaptions of thermal LBM to axisymmetric coordinates have been developed in recent years for thermal convective flow and phase change. In this section, the axisymmetric D2Q5 and D2Q9 thermal MRT-LBM are introduced.

4.3.1 D2Q5 Temperature-Based Thermal MRT-LBM

The D2Q5 temperature-based thermal MRT-LBM for axisymmetric coordinates from Wang et al. [53] is introduced in this section. The thermal lattice equation can be expressed as

$$\begin{aligned}\mathbf{g}(\mathbf{x}+\mathbf{e}\delta_t, t+\delta_t) - \mathbf{g}(\mathbf{x},t) = &- \mathbf{N}^{-1}\mathbf{R}\left[\mathbf{n}(\mathbf{x},t) - \mathbf{n}^{eq}(\mathbf{x},t)\right] + \delta_t \mathbf{N}^{-1}\boldsymbol{\Psi} \\ &+ \delta_t \mathbf{N}^{-1}(\mathbf{I} - \frac{\mathbf{R}}{2})\mathbf{H},\end{aligned} \tag{4.9}$$

where the transformation matrix $\mathbf{N}$ is in non-orthogonal form, defined as

$$N = \begin{bmatrix} 1 & 1 & 1 & 1 & 1 \\ 0 & 1 & 0 & -1 & 0 \\ 0 & 0 & 1 & 0 & -1 \\ 0 & 1 & 1 & 1 & 1 \\ 0 & 1 & -1 & 1 & -1 \end{bmatrix}, \tag{4.10}$$

and the equilibrium moment vector $\mathbf{n}^{eq}$ is expressed as

$$\begin{aligned}\mathbf{n}^{eq} &= \mathbf{N}\mathbf{g}^{eq} \\ &= \left[\begin{array}{ccccc} rT, & ru_zT, & ru_rT, & r\theta T, & 0 \end{array} \right]^T, \end{aligned} \tag{4.11}$$

where θ is a constant between 0 and 1.

Besides, $\mathbf{\Psi}$ is the source term given by

$$\mathbf{\Psi} = (0, 0, \alpha T\sigma_2, 0, 0)^T, \tag{4.12}$$

where thermal diffusivity α can be effective thermal diffusivity α_e for porous flow at REV scale, and σ_2 is the third component of the relaxation matrix $\mathbf{S}$ calculated as $\sigma_1 = \sigma_2 = 1/\tau_g$, where τ_g can be determined by the thermal diffusivity as $\tau_g = v/(c_{sT}^2\delta_t) + 0.5$. And $\mathbf{H}$ is a correction term defined as,

$$\mathbf{H} = (0, TF_z, TF_r, 0, 0)^T. \tag{4.13}$$

The temperature equilibrium distribution function g_i^{eq} is given by

$$g_i^{eq} = rT\bar{\omega}_i(1 + \frac{\mathbf{e}_i \cdot \mathbf{u}}{c_{sT}^2}), \tag{4.14}$$

where weight coefficients $\bar{\omega}_i$ equal to $1/2$ for $i = 0$ and $1/8$ for $i = 1 - 4$, and the lattice sound speed is defined as $c_{sT} = \sqrt{\theta/2}$ for D2Q5 model. And the temperature

T can be determined by

$$T = \sum_{i=0}^{4} g_i. \tag{4.15}$$

4.3.2 D2Q9 Enthalpy-Based Thermal MRT-LBM

The modifications of D2Q9 enthalpy-based thermal MRT-LBM for axisymmetric coordinates proposed by Li et. al [49] are introduced in this section. Although the mechanism of the single-phase enthalpy-based MRT-LBM can be directly used for phase change in Cartesian coordinates, the adaption of the model to axisymmetric coordinates requires additional treatments.

First, the MRT lattice equation is modified as

$$\mathbf{g}(\mathbf{x} + \mathbf{e}\delta_t, t + \delta_t) - \mathbf{g}(\mathbf{x}, t) = -\mathbf{N}^{-1}\mathbf{R}\left[\mathbf{n}(\mathbf{x}, t) - \mathbf{n}^{eq}(\mathbf{x}, t)\right] + \delta_t \mathbf{Q}_m, \tag{4.16}$$

where the relaxation matrix $\mathbf{R}$ is given by Eq. (4.5), the transformation matrix $\mathbf{N}$ is the same as Eq. (3.19), and the equilibrium moment vector $\mathbf{n}^{eq}$ is defined in the same form as Eq. (3.69) but with (r, z) subscripts.

The source term $\mathbf{Q}_m$ in Eq. (4.16) is then expressed as

$$\mathbf{Q}_m = -\frac{c_p T u_r}{r}(1, 0, 0, 0, 0, 0, 0, 0, 0)^T. \tag{4.17}$$

Besides, the first component of post-collision moment vector is modified to retrieve

the extra terms in axisymmetric coordinates, which is given by

$$\bar{n}_0^* = n_0^* - \frac{1}{r}(1 - 0.5\sigma_j)c\delta_t(n_3 - n_3^{eq}), \tag{4.18}$$

where n_0^* is the post-collision values for 0th moment, $\bar{n}_0^*$ is the new value of the 0th moment after the modification, and n_3, n_3^{eq} are 4th component of the moment vector and equilibrium moment vector before the collision respectively.

Correspondingly, this D2Q9 axisymmetric thermal MRT-LBM is developed based on the same concept as the second method used for the axisymmetric flow field introduced in Section 3.1.4. And since it is based on enthalpy, the enthalpy can be recovered from Eq. (3.63), which can be further used to calculate the temperature field based on the prescribed enthalpy equations.

4.4 Modified D2Q9 Enthalpy-Based MRT-LBM

As discussed in this chapter, the enthalpy-based LBM has advantages in simulating the solid-liquid phase change. In this section, several improvements to the enthalpy-based thermal MRT-LBM are proposed and developed in this dissertation in order to make it more capable of solving various cases of the PCM HX. To make the introduction more concise, the D2Q9 enthalpy-based MRT-LBM is used to demonstrate those improvements.

4.4.1 Coupling of DSC Correlated Enthalpy Equations

Based on the modified macroscopic energy equations specified in Section 2.6 for DSC correlated enthalpy equations. A corresponding D2Q9 enthalpy-based MRT model is proposed in this dissertation. Compared with the D2Q9 thermal model introduced in Section 3.2.2.2, the new expressions of equilibrium moment vector $\mathbf{n}^{eq}$ and equilibrium distribution function g_i^{eq} are given as follows:

$$\begin{aligned}\mathbf{n}^{eq} &= \mathbf{N}\mathbf{g}^{eq} \\ &= \Bigg[h, -4h + 2c_{p,ref}T + \frac{3h|\mathbf{u}|^2}{c^2}, 4h - 3c_{p,ref}T - \frac{3h|\mathbf{u}|^2}{c^2}, \\ &\frac{hu_x}{c}, -\frac{hu_x}{c}, \frac{hu_y}{c}, -\frac{hu_y}{c}, \frac{h(u_x^2 - u_y^2)}{c^2}, \frac{hu_xu_y}{c^2}\Bigg],\end{aligned} \tag{4.19}$$

$$g_i^{eq} = \begin{cases} h - c_{p,ref}T + \omega_i c_{p,ref}T - \omega_i h\dfrac{|\mathbf{u}|^2}{2c_s^2}, & i = 0, \\ \omega_i c_{p,ref}T + \omega_i h\left[\dfrac{(\mathbf{e}_i \cdot \mathbf{u})}{c_s^2} + \dfrac{(\mathbf{e}_i \cdot \mathbf{u})^2}{2c_s^4} - \dfrac{|\mathbf{u}|^2}{2c_s^2}\right], & i \neq 0, \end{cases} \tag{4.20}$$

where the enthalpy h is modeled based on the DSC correlated equations as specified in Section 2.5.2.

Additionally, for axisymmetric coordinates, the source term $\mathbf{Q}_m$ defined in Eq. (4.17) should also be modified as

$$\mathbf{Q}_m = -\frac{hu_r}{r}(1, 0, 0, 0, 0, 0, 0, 0, 0)^T. \tag{4.21}$$

4.4.2 High Rayleigh Number Flow Treatment

According to the Chapman-Enskog expansion, the recovered macroscopic energy equation contains the deviation term $\partial_t(h\mathbf{u})$, which can be ignored if the driven force in the liquid zone is not drastic. This assumption is valid under the Boussinesq approximation, but the error from the deviation term may become significant for high Rayleigh number flow ($Ra > 10^6$), where the flow velocity driven from the buoyancy force is high enough.

Based on the concept from [48, 84] and the developed D2Q9 thermal MRT-LBM in Section 4.4.1, a modified source term $\mathbf{Q}_m$ in the moment space for D2Q9 model is proposed in this dissertation to eliminate the mentioned deviation term, which can be given by

$$\mathbf{Q}_m = \Big[0\ ,\ 0\ ,\ 0\ ,\ (1-\frac{1}{2\tau_g})\Delta(hu_x)\ ,\ -(1-\frac{1}{2\tau_g})\Delta(hu_x)\ ,\ (1-\frac{1}{2\tau_g})\Delta(hu_y)\ ,\ -(1-\frac{1}{2\tau_g})\Delta(hu_y)\ ,\ 0\ ,\ 0\Big], \tag{4.22}$$

where $\Delta(hu_x)$ and $\Delta(hu_y)$ can be calculated by a forward scheme defined as follows:

$$\begin{aligned}\Delta(hu_x) &= h(\mathbf{x}, t+\delta_t)u_x(\mathbf{x}, t+\delta_t) - h(\mathbf{x}, t)u_x(\mathbf{x}, t)\\ \Delta(hu_y) &= h(\mathbf{x}, t+\delta_t)u_y(\mathbf{x}, t+\delta_t) - h(\mathbf{x}, t)u_y(\mathbf{x}, t)\end{aligned} \tag{4.23}$$

By applying this modification to the source term, the error caused by the term $\partial_t(h\mathbf{u})$ can be eliminated. And owing to this, the enthalpy-based MRT can be

capable of simulating high Rayleigh number flow ($Ra > 10^8$) accurately.

Similarly, the modified source term in axisymmetric coordinates can be given as

$$\mathbf{Q}_m = \Big[-\frac{hu_r}{r}\ ,\ 0\ ,\ 0\ ,\ (1-\frac{1}{2\tau_g})\Delta(hu_r)\ ,\ \ -(1-\frac{1}{2\tau_g})\Delta(hu_r)\ ,\ (1-\frac{1}{2\tau_g})\Delta(hu_z)\ ,\ \ -(1-\frac{1}{2\tau_g})\Delta(hu_z)\ ,\ 0\ ,\ 0\Big]. \tag{4.24}$$

4.4.3 Conjugate Heat Transfer

4.4.3.1 Conducting Fins in PCM HX

In Section 2.4, the governing equations for conducting fins are provided. A separate D2Q9 thermal MRT model can be used to simulate the pure conduction in fins by simply setting $\mathbf{u} = (0, 0)$ and $\alpha = \alpha_{fin}$.

Besides, the enthalpy h is defined as $h_{fin} = c_{p,fin}T$ for conducting fins, and the temperature and heat flux across the surface between the fins and the PCM should be consistent, which can be expressed as

$$T_{fin} = T_{PCM}, \tag{4.25}$$

$$\mathbf{n}_v \cdot (-k\nabla T)_{fin} = \mathbf{n}_v \cdot (-k\nabla T)_{PCM}, \tag{4.26}$$

where $\mathbf{n}_v$ is the normal vector of the surface.

4.4.3.2 Heat Transfer Fluid (HTF) Flow in PCM HX

For the HTF flow in the PCM HX, as shown in Fig. 4.1, the HTF is charged from the inlet and go through the pipe to transfer the heat with the PCM. If the PCM and the wall of the pipe are modeled, then the thermal boundary condition for the left side of the PCM container should be determined.

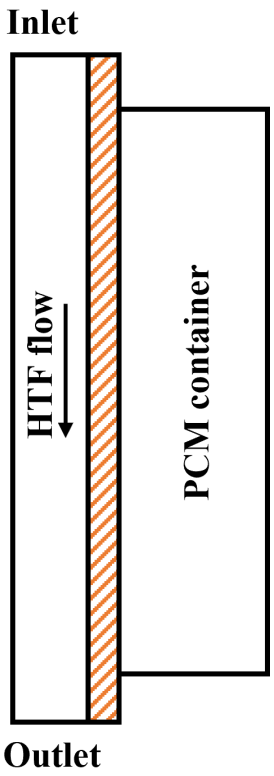

Figure 4.1: Heat transfer fluid (HTF) with PCM HX.

For the boundary treatment in the LBM, the temperature on the surface between the HTF and the wall is required. And thus the thermal boundary condition on the left side with the HTF is actually the temperature along the surface. However, if only the inlet temperature of the HTF is fixed, then the temperature along

the surface also depends on the heat transfer of the PCM.

In order to model the HTF flow side efficiently, a one-dimensional model as shown in Fig. 4.2 is used to simulate the temperature field of the HTF flow by assuming the temperature variations only occur along the flow direction. Then, at each time step, the temperature along the surface (wall) between the HTF and the PCM can be determined by assuming the consistent temperature T_{wall} and heat flux $\dot{Q}_{wall}$ between both sides of the surface, which can be calculated as

$$T_{wall} = C_{HTF}T_{HTF} + C_{PCM}T_{PCM}, \tag{4.27}$$

where $C_{HTF} + C_{PCM} = 1$, and the values of these two coefficients are determined by the heat resistance on each side of the surface. Following that, the heat flux $\dot{Q}_{wall}(x_i, t)$ from the HTF to the PCM can be obtained on each grid point in Fig. 4.2. If then setting the inlet mass flow rate as $\dot{m}_{HTF}$ and energy flux as $\dot{Q}_{HTF}(x_0, t) = \dot{m}_{HTF}c_{p,HTF}T(x_0, t)$ for the HTF, the temperature of the HTF along the flow direction for the next time step can be determined by performing the energy balance on each grid point of the 1D HTF model, as given by

$$\begin{aligned} T(x_{i+1}, t + \delta_t) &= \frac{\dot{Q}_{HTF}(x_i, t) - \dot{Q}_{wall}(x_i, t)}{\dot{m}_{HTF}c_{p,HTF}}, \\ &= T(x_i, t) - \frac{\dot{Q}_{wall}(x_i, t)}{\dot{m}_{HTF}c_{p,HTF}}, \end{aligned} \tag{4.28}$$

where subscript i is from 0 to n, where n refers to the number of the grid points in the HTF flow direction.

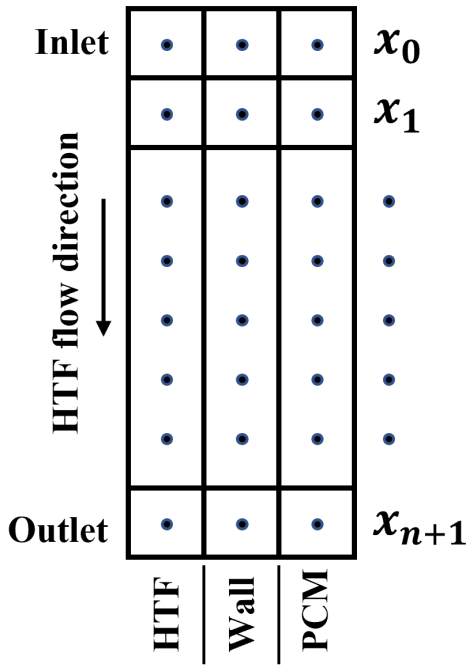

Figure 4.2: 1D HTF flow model.

By utilizing this 1D model for the temperature of the HTF and applying the calculated temperature along the wall to the boundary conditions in LBM, the variation of the temperature difference between the inlet and outlet of the HTF flow during the PCM melting can be achieved in the thermal LBM.

4.5 Boundary Treatments in LBM for PCM HX

For a general PCM HX configuration as shown in Fig. 4.3, the flow boundary conditions obviously can be the rigid wall with zero velocities, while the types of thermal boundary conditions can be either adiabatic (top and bottom boundaries) or convective (left and right boundaries). The application of boundary conditions in LBM is particle-based, performed at lattice scale instead of the macroscopic level. In this section, the boundary treatments in LBM are introduced both for the flow

and temperature field.

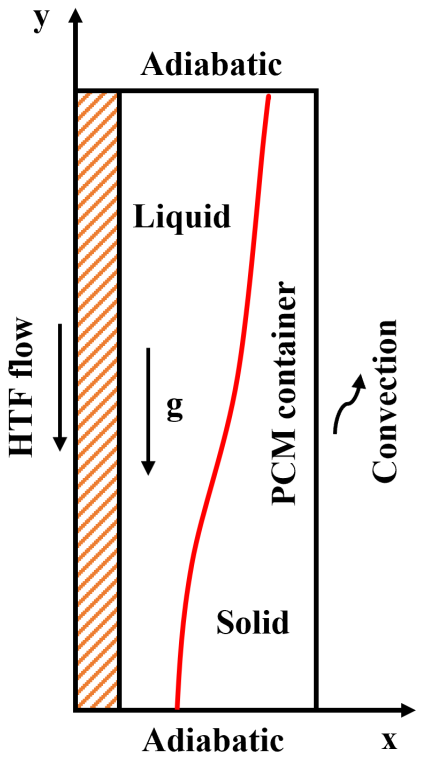

Figure 4.3: Types of boundary conditions in a PCM HX.

In LBM, solving the boundary conditions is to obtain the unknown distribution functions on the boundary nodes. Once the distribution functions on the boundary nodes are calculated, the entire field can be solved.

For the flow field, the half-way bounce back scheme [85] is adopted to solve the distribution functions on rigid walls by assuming the actual boundary surface is placed halfway between the PCM nodes and the solid wall nodes. This method is of second-order accuracy both in time and space.

For the temperature field, a half-way specular reflection scheme is applied to handle the thermal distribution functions at adiabatic boundaries. The differ-

ence between this scheme and the half-way bounce back scheme is demonstrated in Fig. 4.4, where the dashed line denotes the boundary placed halfway between the PCM layer and the wall layer, f_i and g_i are incident post-collision distribution functions from PCM nodes, and f_{ib} and g_{ib} are the reflected distribution functions at the boundary nodes.

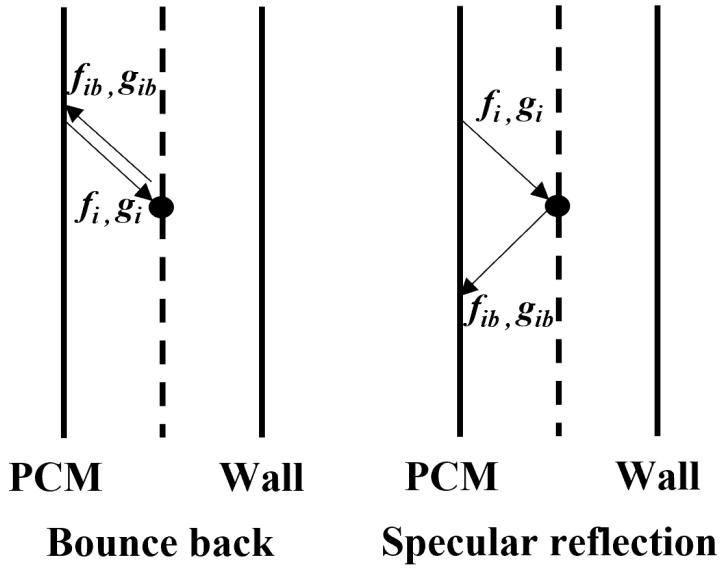

Figure 4.4: Half-Way bounce back scheme and half-way specular reflection scheme.

For convection heat transfer, the boundary treatment is to first determine the temperatures on the boundary nodes by using the method demonstrated in Section 4.4.3.2. Then the distribution functions on the boundary nodes can be obtained by an extrapolation scheme based on the boundary temperatures, and the details can be found in the literature from Chen et al. [86].

4.6 Parallel LBM Scheme

Owing to the completely local collision process and the explicit streaming process in LBM, the development of the parallel scheme in LBM is fairly convenient. The parallel LBM scheme is one of the common methods to solve large-scale problems in a time-efficient way. Therefore, a parallel LBM scheme for the enthalpy-based MRT LBM is developed in order to accelerate the simulation of the solid-liquid phase change, by which the parametric study of the PCM HX can be performed efficiently.

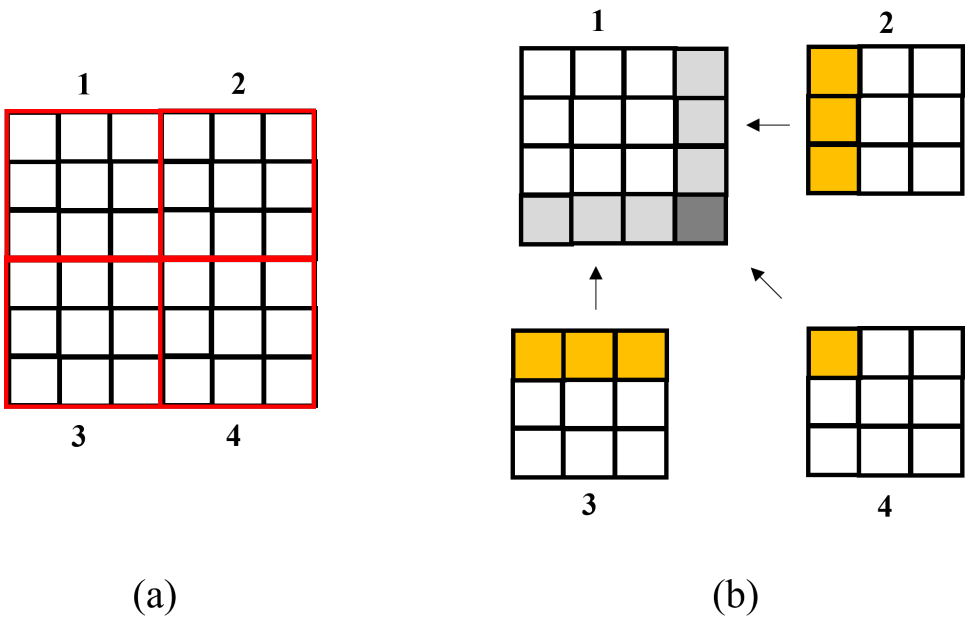

Figure 4.5: Parallel LBM scheme: (a) partial units (PUs) division and (b) data transition between PUs.

Generally, the mesh grid of LBM can be divided into several partial units (PUs), shown as the red rectangles denoted by 1, 2, 3, and 4 in Fig. 4.5. Because the calculation of the streaming process at each grid point in LBM requires information

from its nearby points, the data need to be transferred between partial units. Taking the partial unit 1 shown in Fig. 4.5 as an example, an extra layer of the grid pints shaded by the gray color is added to store the data transferred from the grid points highlighted by the orange color of its nearby partial units (2, 3 and 4).

In terms of code development, the communication between PUs is achieved by Message Passing Interface (MPI), and the parallel LBM scheme in this dissertation is programmed in C++. Besides, Microsoft MPI (MSMPI) is used for Windows environment and OpenMPI for Linux environment.

4.7 Unit Conversion from Macroscopic Units to Lattice Units

Unlike macroscopic units, there is only one system of units in LBM, i.e., lattice units. Because of this, many LBM literature omitted the lattice units when introducing their lattice Boltzmann simulations. But to demonstrate the unit conversion clearly, it is worth mentioning that the primary lattice units in LBM are length unit (lu), mass unit (mu), temperature unit (tu) and time unit (ts). In most lattice Boltzmann models, the space and time steps can be set to unity, i.e., $\Delta r = \Delta z = 1$ lu and $\Delta t = 1$ ts. For incompressible flow, the density in LBM is commonly chosen to be unity ($\rho_{lattice} = 1.0$ mu/lu^3) and the characteristic velocity ($u_{lattice}$) in lattice units should be set carefully to maintain a low Mach number ($Ma \ll 1$) and avoid instability issues. Based on these pre-assigned values, and in coupling with the matching of the critical dimensionless numbers and geometries, other parameters in lattice units can be converted from those of macroscopic units.

Taking the two-dimensional thermal convective flow in a vertical annulus with SI units as an example, the annulus that has radius $R = 0.1$ m and length $L = 0.2$ m is filled with water at $T_f = 293$ K. The physical values of properties of water at 293 K are density $\rho = 998.29$ kg/m^3, kinematic viscosity $v = 1.00 \times 10^{-6}$ m^2/s, thermal diffusivity $\alpha = 1.43 \times 10^{-7}$ m^2/s and thermal expansion coefficient $\beta = 2.07 \times 10^{-4}$ 1/K. Additionally, the wall of the annulus is kept at $T_b = 323$ K. To solve this problem, an axisymmetric model based on LBM is established with the computational domain $[N_r, N_z] = [100, 200]$.

To convert these parameters in the example from SI units to lattice units, the referenced values for the four primary units (lu, mu, tu, ts) need to be determined initially. The referenced value L_r in the length unit can be calculated as

$$L_r = \frac{R}{N_r \Delta r} = \frac{L}{N_z \Delta z} = 1.00 \times 10^{-3} \text{ m/lu}. \tag{4.29}$$

The referenced value m_r in the mass unit can then be determined by

$$m_r = Lr^3 \frac{\rho}{\rho_{lattice}} = 9.98 \times 10^{-7} \text{ kg/mu}, \tag{4.30}$$

where $\rho_{lattice}$ is pre-assigned to 1.0 as mentioned above in this section. Similarly, the referenced value t_r in the time unit can be determined by L_r in coupling with the velocity ratio between SI units and lattice units. Assuming the caracteristic velocity

in LBM is set to $u_{lattice} = 0.01\ lu/ts$, then t_r can be expressed as

$$t_r = L_r \frac{u_{lattice}}{u_c} = L_r \frac{u_{lattice}}{\sqrt{g\beta(T_b - T_f)L}} = 9.06 \times 10^{-5}\ \text{s/ts}, \tag{4.31}$$

where gravitational acceleration g in SI units is 9.81m/s^2. To covert g to lattice units, the same method is applied, i.e., $g_{lattice} = gt_r^2/L_r = 8.05 \times 10^{-5}\ lu/ts^2$. The last referenced value T_r in the temperature unit can be chosen arbitrarily, e.g., assuming $\Delta T_{lattice} = 1$ tu, then T_r is given by

$$T_r = \frac{T_b - T_f}{\Delta T_{lattice}} = 30\ \text{K/tu}. \tag{4.32}$$

After the initial step, the parameters in lattice units, such as kinematic viscosity, thermal diffusivity and thermal expansion coefficient, can be converted utilizing the combination of the four basic referenced values from Eqs. (4.29)–(4.32). Therefore in the given example, the parameters in lattice units are calculated as

$$\begin{aligned} v_{lattice} &= v\frac{tr}{L_r^2} = 9.06 \times 10^{-5}\ \text{lu}^2/\text{s}, \\ \alpha_{lattice} &= \alpha\frac{tr}{L_r^2} = 1.30 \times 10^{-5}\ \text{lu}^2/\text{s}, \\ \beta_{lattice} &= \beta T_r = 6.21 \times 10^{-3}\ 1/\text{tu}. \end{aligned} \tag{4.33}$$

In the same way, other parameters in LBM can be converted from the macroscopic units. Finally, the critical dimensionless numbers can be calculated with the

parameters in lattice units to check the correctness of the unit conversion. These dimensionless numbers, as shown in Eq. (2.31), need to be kept the same between the lattice units and the macroscopic units. For instance, the Rayleigh number in LBM is computed as

$$\begin{aligned} Ra_{lattice} &= \frac{g_{lattice}\beta_{lattice}\Delta T_{lattice}(N_z\Delta z)^3}{v_{lattice}\alpha_{lattice}} \\ &= 3.40 \times 10^9, \end{aligned} \tag{4.34}$$

which is in the same value compared with the Rayleigh number calculated from SI units. Additionally, the critical dimensionless numbers can act as bridges to link the lattice units with the macroscopic units. Therefore, they also can be utilized to calculate the values of the parameters in LBM to simplify the calculation of the unit conversion.

4.8 Chapter Summary

The enthalpy-based method is widely used for the simulation of the PCM phase change to track the liquid fraction by updating the enthalpy. The integration of the enthalpy-based method with the LB model extends the application of LBM in solving solid-liquid phase change problems. In this chapter, the development of a solid-liquid MRT LB model is introduced from Section 4.1 to Section 4.4. Besides, the boundary treatments in LBM for flow and temperature fields (Section 4.5), the development of the parallel LBM scheme (Section 4.6) and the conversion from macroscopic units to lattice units (Section 4.7) are also briefly discussed.

To summarize and highlight the basic models and the modifications adopted and developed for the solid-liquid phase change, the following subsections give a comprehensive D2Q9 enthalpy-based DDF-MRT LBM either in Cartesian coordinates or in axisymmetric coordinates.

4.8.1 D2Q9 DDF-MRT LBM in Cartesian Coordinates

The D2Q9 MRT-LBM for the flow with porous media at the REV scale introduced in Section 3.1.5.1 can be used for simulating the convective flow in the liquid PCM zone.

The D2Q9 enthalpy-based MRT-LBM introduced in Section 3.2.2.2, together with the enthalpy equations in Section 2.5, porous media treatments in Section 4.2, modifications proposed in Section 4.4, can be used for simulating the heat transfer of the PCM with or without fins across the entire domain.

Through Chapman-Enskog expansion [50, 87, 88], the corresponding macroscopic governing equations (2.9, 2.10 and 2.29) can be recovered. By setting the porosity ϕ equal to one, the model can be reduced to simulate the pure PCM convective heat transfer problems.

4.8.2 D2Q9 DDF-MRT LBM in Axisymmetric Coordinates

The D2Q9 MRT-LBM for the axisymmetric flow with porous media at the REV scale introduced in Section 3.1.5.2 is adopted to solve the axisymmetric porous convective flow in the liquid PCM zone.

The axisymmetric D2Q9 enthalpy-based MRT-LBM demonstrated in Section 4.3.2, together with the enthalpy equations in Section 2.5, porous media treatments in Section 4.2, modifications proposed in Section 4.4, is capable of simulating the various cases of the convective PCM heat transfer.

Through Chapman-Enskog expansion [50, 87, 88], the macroscopic governing equations (2.13, 2.14, 2.15 and 2.30) can be recovered. Similarly, by setting the porosity ϕ equal to one, the model can be reduced to simulate the axisymmetric pure PCM convective heat transfer problems.

Chapter 5: Numerical Simulations

The enthalpy-based DDF-MRT lattice Boltzmann model is developed based on the concepts and theories introduced in Chapter 2, Chapter 3 and Chapter 4. In this chapter, various numerical simulations are conducted to verify and validate the developed model, which is demonstrated in Section 5.1 and Section 5.2. Meanwhile, the scaling analysis of the parallel LBM scheme is introduced in Section 5.3 for the PCM HX.

5.1 Numerical Verification

5.1.1 Isothermal Flow in Lid-Driven Cavity

To verify the developed 2D single-phase LB model for flow field in Chapter 3, a simulation has been conducted for a 2D rectangular cavity with its top lid moving horizontally at a constant velocity U. Two cases are considered, $Re = 1000$ and $Re = 2000$. The schematic of the lid-driven cavity is shown in Fig. 5.1.

The computational domain is set to 257×257, the lid velocity $U = 0.1$ and the length $L = 1$ in the LB model. The streamlines of the flow within the cavity for different Re are shown in Fig. 5.2 and Fig. 5.3.

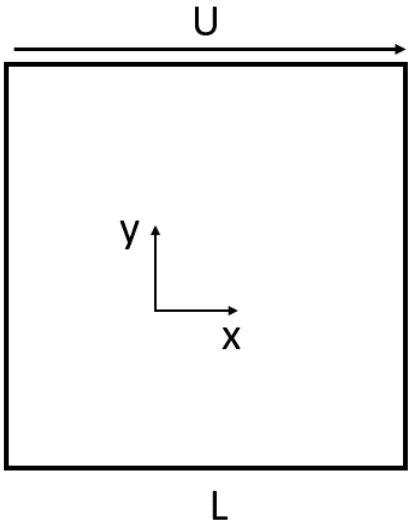

Figure 5.1: Lid-driven cavity.

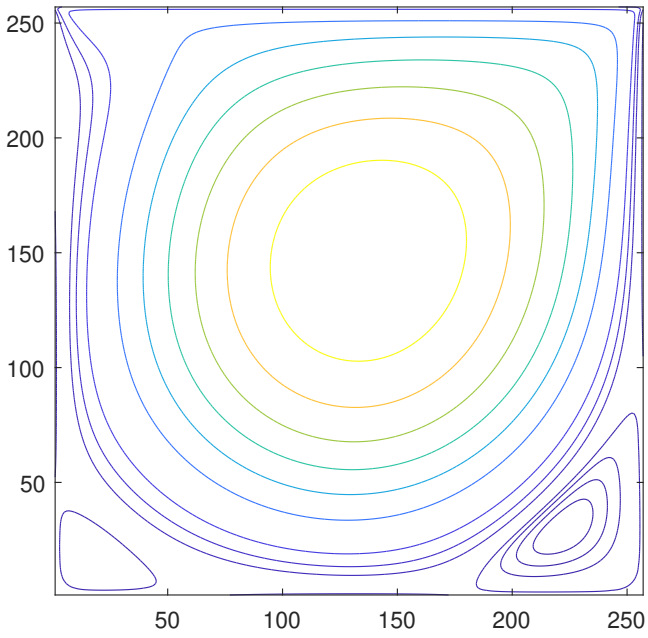

Figure 5.2: Streamlines of lid-driven cavity at Re = 1000.

There are three vortexes observed in the cavity due to the competition between inertia and shear stress. It is observed that a large primary vortex locates near the

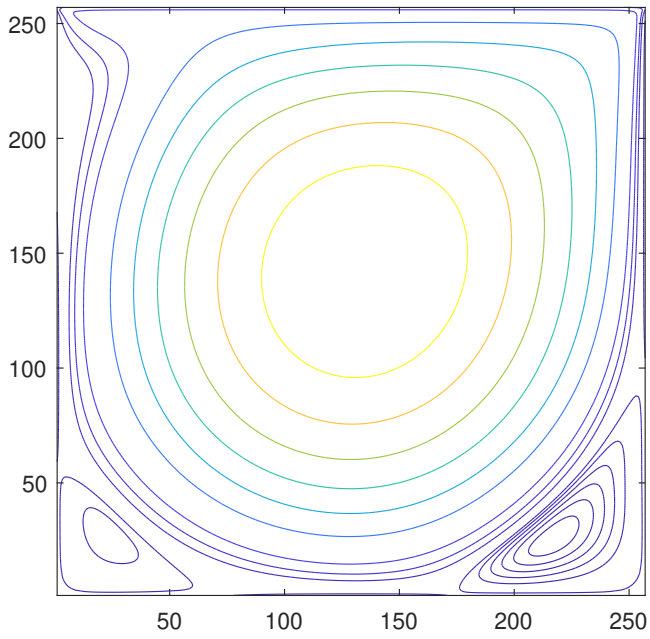

Figure 5.3: Streamlines of lid-driven cavity at Re = 2000.

center of the cavity and two small secondary vortexes appear at the bottom left and bottom right corners respectively. By measuring the exact center locations for those vortexes and comparing them with the results from Vanka and S Pratap [1], the single-phase LB model for the flow field is verified. The results are listed in Table 5.1

Re	Primary vortex	Bottom left vortex	Bottom right vortex
1000 (a)	[0.5438, 0.5625]	[0.0750, 0.0813]	[0.8625, 0.1063]
1000 (b)	[0.5334, 0.5660]	[0.0821, 0.0730]	[0.8610, 0.1108]
2000 (a)	[0.5250, 0.5500]	[0.0875, 0.1063]	[0.8375, 0.0938]
2000 (b)	[0.5230, 0.5486]	[0.0864, 0.1021]	[0.8421, 0.0963]

Table 5.1: Comparison of the Location of the Vortexes: (a) Vanka and S Pratap [1]; (b) Our Model.

5.1.2 PCM Melting with Porous Media in Cartesian Coordinates

In this section, a simulation of the PCM melting in a porous square cavity is conducted to test the performance of the basic Cartesian lattice Boltzmann model.

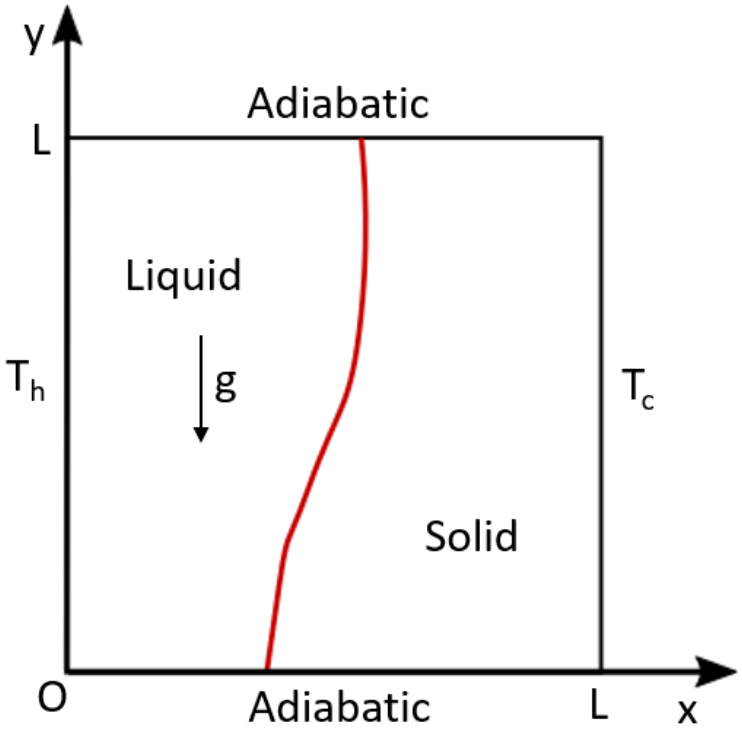

Figure 5.4: Schematic of the porous square cavity with PCM.

Rayleigh Number	Prandtl Number	Stefan Number	Porosity
841,000	0.0208	0.1241	0.385

Table 5.2: Dimensionless number for PCM melting in the porous cavity.

The square cavity is shown in Fig. 5.4, where the left surface is maintained at the highest temperature $T_h = 45$ °C and the right surface is held at the lowest temperature $T_c = 20$ °C. Both the top and bottom surfaces are adiabatic and the porous cavity is filled with the solid PCM initially. The melting temperature of the

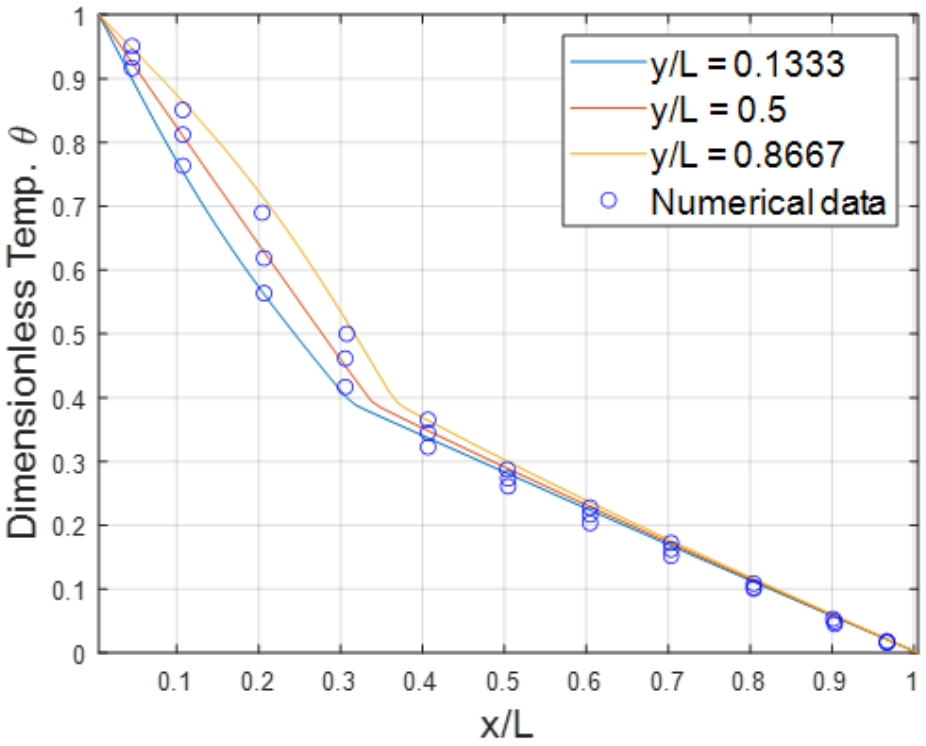

Figure 5.5: Comparison of temperature profile of PCM melting in the porous cavity with the numerical data [11] at $Fo = 1.829$.

PCM $T_m = 29.78$ °C and the initial temperature $T_i = T_c$, whereby the solid PCM starts to melt from the left side to the right side as time continues. Additionally, the PCM melting is assumed with no temperature glide. To verify the developed axisymmetric lattice Boltzmann model, the parametric settings listed in Table 5.2 are obtained from Liu et. al [51], and the computational domain is set to $[N_x, N_y] = [200, 200]$.

The temperature profile at Fourier Number $Fo = \alpha t/L^2 = 1.829$ is shown in Fig. 5.5, where $\theta = (T - T_c)/(T_h - T_c)$ is the dimensionless temperature, the lines are the results from the present model and the dots are the numerical data points from C. Beckermann and R. Viskanta [11]. The comparison shows a reasonable

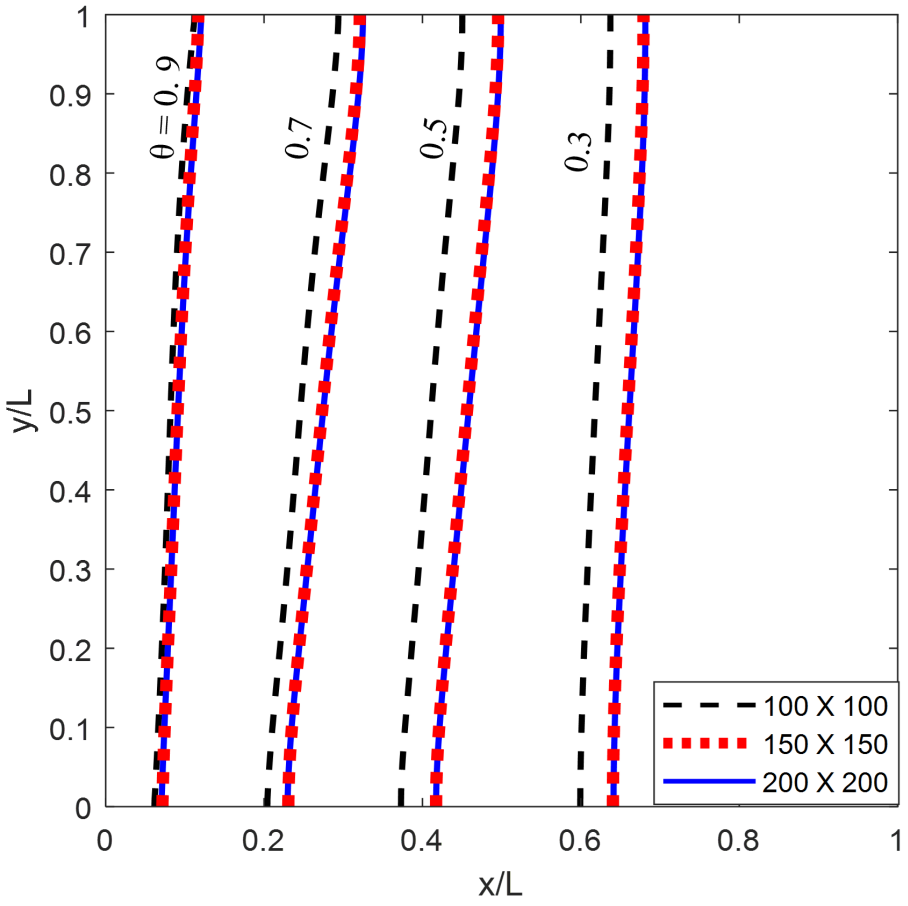

Figure 5.6: Isotherms at $Fo = 1.829$ with mesh size being 100×100, 150×150 and 200×200.

agreement and indicates that the basic Cartesian lattice Boltzmann model is capable of solving the convective PCM melting with the porous media. Additionally, a grid-independent study is conducted for this case. Three simulations were run on mesh sizes 100×100, 150×150 and 200×200 respectively and the results in Fig. 5.6 show the isotherms at $Fo = 1.829$. Comparing the deviation of the isotherms among each mesh size, the results indicate that the system with mesh size 150×150 is almost grid-independent.

5.1.3 Thermal Convective Flow in Axisymmetric Coordinates

Given that adapting the Cartesian LBM to axisymmetric coordinates alters the terms in the MRT scheme [49] and natural convection in the liquid zone plays an important role in PCM melting, it is necessary to verify the ability of the axisymmetric model to solve thermal flow with natural convection. Therefore a vertical annulus filled with the pure liquid is simulated based on this axisymmetric model, as shown in Fig. 5.7.

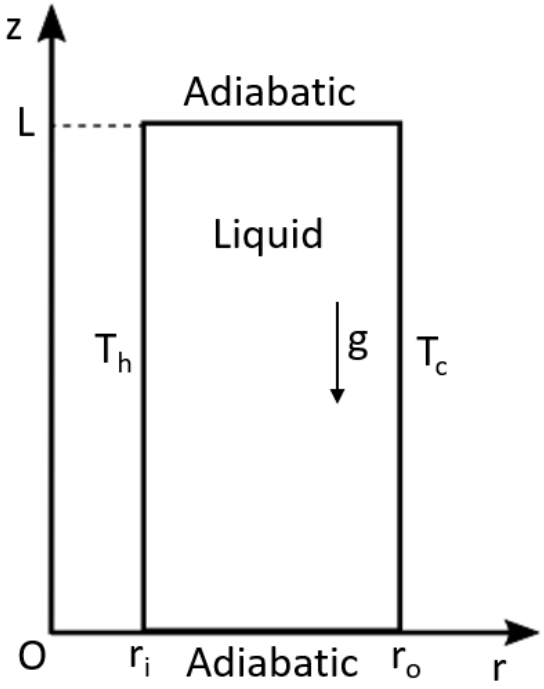

Figure 5.7: Schematic of the vertical annulus with pure liquid.

The thermal flow is simulated without porous media at various Rayleigh numbers ($Ra = 10^3,\ 10^4,\ 10^5$), where the computational domain is $[N_r, N_z] = [100, 200]$ and both the aspect ratio $L/(r_o - r_i)$ and the diameter ratio r_o/r_i are set to 2. The highest dimensionless temperature T_h is kept at 1 and lowest dimensionless

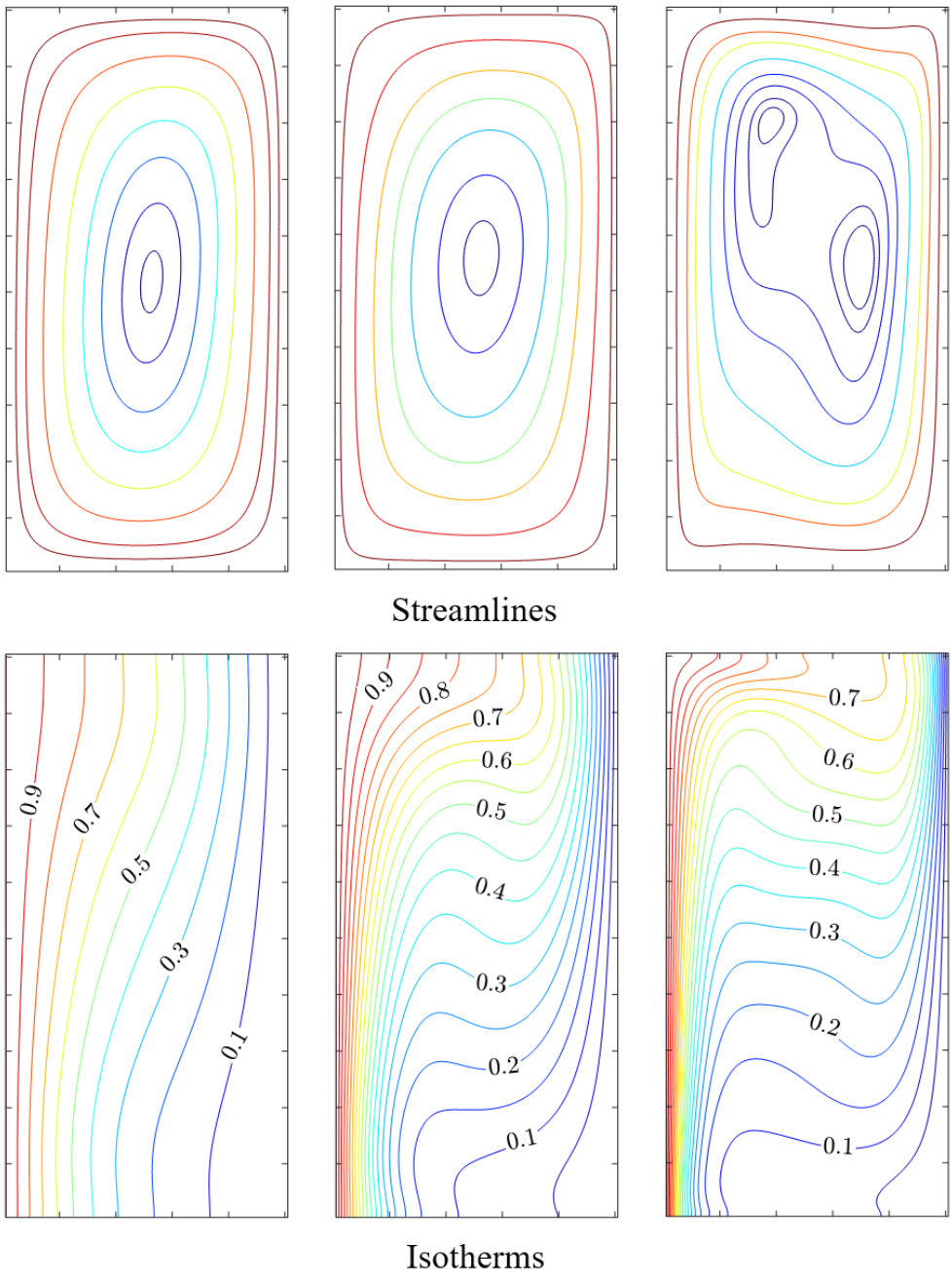

Figure 5.8: Streamlines and isotherms of the thermal flow in the vertical annulus for $Ra = 10^3$ (Left), 10^4 (Middle), 10^5 (Right).

temperature T_c is 0.

The streamlines and isotherms for different Ra are displayed in Fig. 5.8 and

Ra	Li et. al [89]	Wang et. al [90]	Present model
10^3	1.692	1.688	1.685
10^4	3.215	3.210	3.207
10^5	5.787	5.793	5.741

Table 5.3: Comparison of the Average Nusselt Numbers.

Ra	50×100	100×200	200×400
10^3	1.602	1.685	1.685
10^4	2.975	3.207	3.209
10^5	4.764	5.741	5.744

Table 5.4: Average Nusselt Numbers at Steady-State with Mesh Size being 50×100, 100×200 and 200×400.

the corresponding average Nusselt numbers are tabulated in Table 5.3 in comparison with the numerical results from Li et. al [89] and Wang et. al [53]. A clear trend can be seen in Fig. 5.8 that more hot fluid is driven from the bottom to the top near the inner (left) plate as Ra becomes higher, which results in the different flow and temperature distributions among these three cases. Moreover, the comparison of the average Nusselt numbers indicates that the present axisymmetric model is capable of solving the convective thermal flow accurately. A grid convergence study is also conducted for this case with three mesh sizes: 50×100, 100×200 and 200×400. The average Nusselt numbers at steady state are compared among the three mesh sizes and the results tabulated in Table 5.4 indicate that this axisymmetric thermal flow case with 100×200 can be regarded as grid-independent.

5.2 Numerical Validation

5.2.1 Thermal Convective Flow with Porous Media in Axisymmetric Coordinates

The new axisymmetric model is verified by simulating pure convective thermal flow as demonstrated in Section 5.1.3. The purpose of the case study in this section is to validate the ability of the new axisymmetric model to simulate porous thermal flow with natural convection. The schematic of the vertical annulus is similar to Fig. 5.7 but with porous media and different geometric ratios. The highest temperature T_h is kept at 60 °C and the lowest temperature T_c is 50 °C, and the rest of the settings are listed in Table 5.5.

Aspect ratio	Diameter ratio	Porosity	Da	Ra	Pr
2.0	5.338	0.3698	1.66×10^{-6}	1.75×10^{8}	1.0

Table 5.5: Dimensionless Numbers for Thermal Convective Flow with Porous Media in the Annulus.

The numerical data in Fig. 5.9 show the steady-state dimensionless temperature (θ) profiles along the radial direction (r) at different heights (Z) in comparison with the experimental data from V. Prasad and F. A. Kulacki. [12]. A small deviation can be observed for the temperature profile at $Z = 1$ near the top left and right corners. But the results, in general, indicate a good match of the temperature distributions in the annulus between the simulation and the experiment. The comparison with experimental data in Fig. 5.9 demonstrates that the new model can simulate the axisymmetric thermal flow with the porous media accurately.

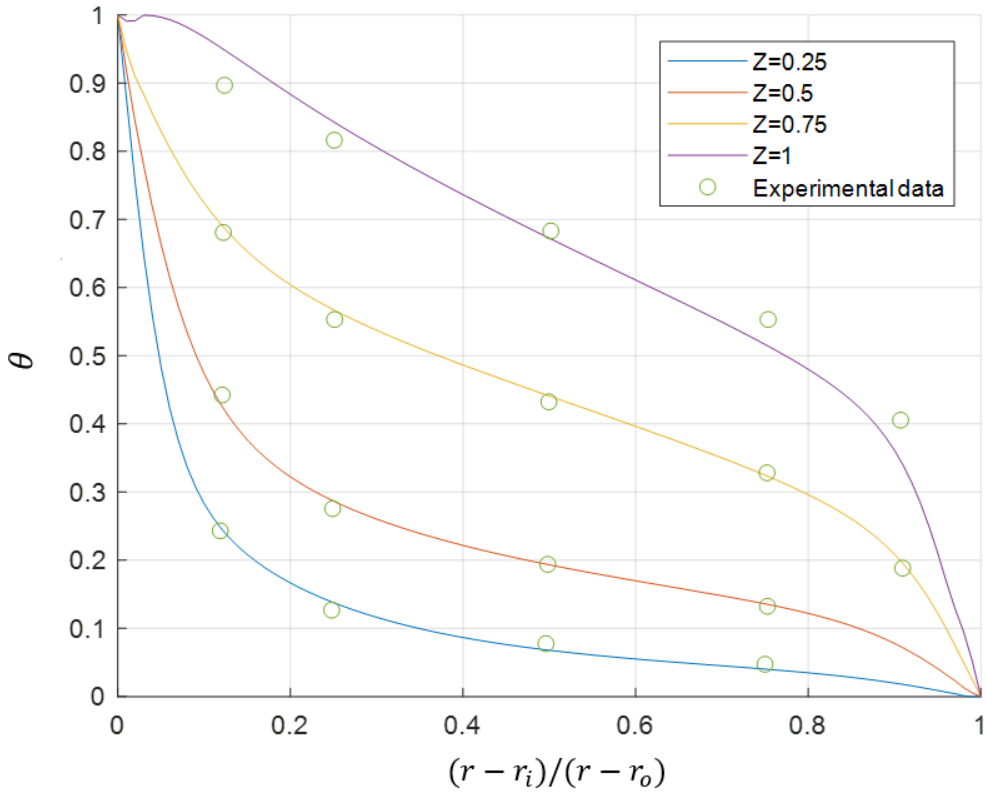

Figure 5.9: Comparison of temperature profiles (θ) of the thermal flow in the porous annulus along radial direction with the experimental data [12] at Different Heights $Z = z/L$.

5.2.2 PCM Melting in Axisymmetric Coordinates

To further validate the new axisymmetric model, a case study of the pure PCM melting in the cylindrical HX is conducted to compare the numerical results with the experimental data from CEEE group. The numerical model is set up based on the experimental settings, as shown in Fig. 5.10, where the type of the PCM used in the experiment is PT37 and its properties are listed in Table 5.6 [2]. The HX is well insulated, and thus both top and bottom boundaries can be treated as adiabatic. However, the right boundary, which is the outer wall of the cylinder, still has a tiny

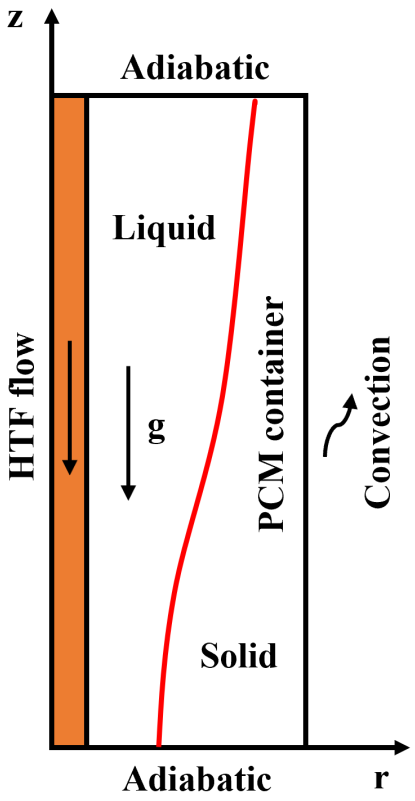

Figure 5.10: Schematic of the cylindrical PCM HX settings.

heat dissipation to the ambient air. Therefore, the convection boundary condition is applied to the right boundary to model this tiny heat loss. On the left boundary, the HTF is hot water pumped downward through the pipe, with the inlet temperature at 59.25 °C. Other important settings including the critical dimensionless numbers are tabulated in Table 5.7, where the Rayleigh number is calculated either based on the length L of the HX or the radius gap R defined as $R = r_o - r_i$, and both values are listed in Table 5.7. Moreover, it is worth noting that there is no exact data for the thermal expansion coefficient β of PT37 in the literature, and consequently, the value of β is assumed based on the properties of another paraffin wax, and is set to 3.85×10^{-4} in the simulation.

Property	Unit	Value
Nominal melting temperature (T_m)	°C	37
Latent heat of fusion (L_a)	kJ/kg	210
Density (solid) (ρ_s)	kg/m^3	920
Density (liquid) (ρ_l)	kg/m^3	840
Specific heat capacity (solid) ($c_{p,s}$)	kJ/(kg K)	2.21
Specific heat capacity (liquid) ($c_{p,l}$)	kJ/(kg K)	2.63
Thermal conductivity (solid) (k_s)	W/(m K)	0.25
Thermal conductivity (liquid) (k_l)	W/(m K)	0.15
Kinematic viscosity (liquid) (v_l)	mm^2/s	6.074

Table 5.6: PCM Properties of PT37 [2].

Parameter	Value
Initial temperature (T_i)	25 °C
Inlet temperature (T_{inlet})	59.25 °C
Length of the HX (L)	400 mm
Inner radius of the HX (r_i)	6.5 mm
Outer radius of the HX (r_o)	22 mm
Rayleigh number based on length (Ra_L)	9.59×10^9
Rayleigh number based on radius gap (Ra_R)	5.58×10^5
Prandtl number (Pr)	89.5
Stefan number (Ste)	0.335

Table 5.7: Parametric Settings for the PCM Melting in the Cylindrical HX.

The simulation is conducted with mesh size 32×800 for the 2-hour PCM melting in the cylindrical HX. According to the experiment, six levels are set to place the thermocouples, where the temperature measurements at three levels (1, 3 and 5) are chosen to compare with our simulation results. The configuration of the thermocouples at these three levels is shown in Fig. 5.11, where two thermocouples are placed at each level, with one at radius r_{in} and one at radius r_{out}. And the height of each level and values of r_{in} and r_{out} are listed in Table 5.8

The temperature profile at each level is compared with the experimental data,

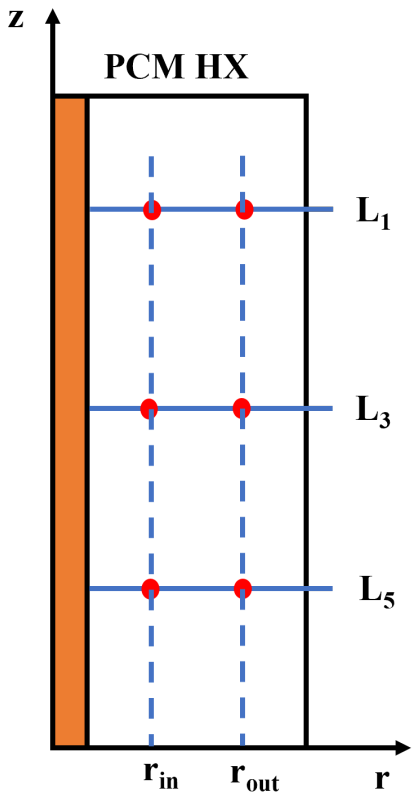

Figure 5.11: Configuration of thermocouples at three levels (L_1, L_3,L_5).

as shown by Fig. 5.12,Fig. 5.13, and Fig. 5.14. Fig. 5.12 shows the comparison of the temperatures at level one, which is located at the top part of the PCM HX. The difference between the simulation and experimental results is relatively small, which indicates a good match of the temperature field in the top part of the HX. Fig. 5.13 is for level three, which is located at the middle of the PCM HX, and relatively larger differences can be observed for inner temperatures after $t = 6000s$ and outer temperatures after $t = 4000s$. Similarly, Fig. 5.14 shows the temperature profile for level five at the bottom part of the HX, and differences can also be observed for both inner and outer temperatures after $t = 4000s$.

For all the three figures (5.12, 5.13 and 5.14), the simulation matches the

Level	Height	r_i	r_o
$\mathbf{L}_1$	350 mm	2.88 mm	9.25 mm
$\mathbf{L}_3$	210 mm	1.76 mm	9.5 mm
$\mathbf{L}_5$	70 mm	2.75 mm	10.5 mm

Table 5.8: Detailed locations of thermocouples in the cylindrical HX.

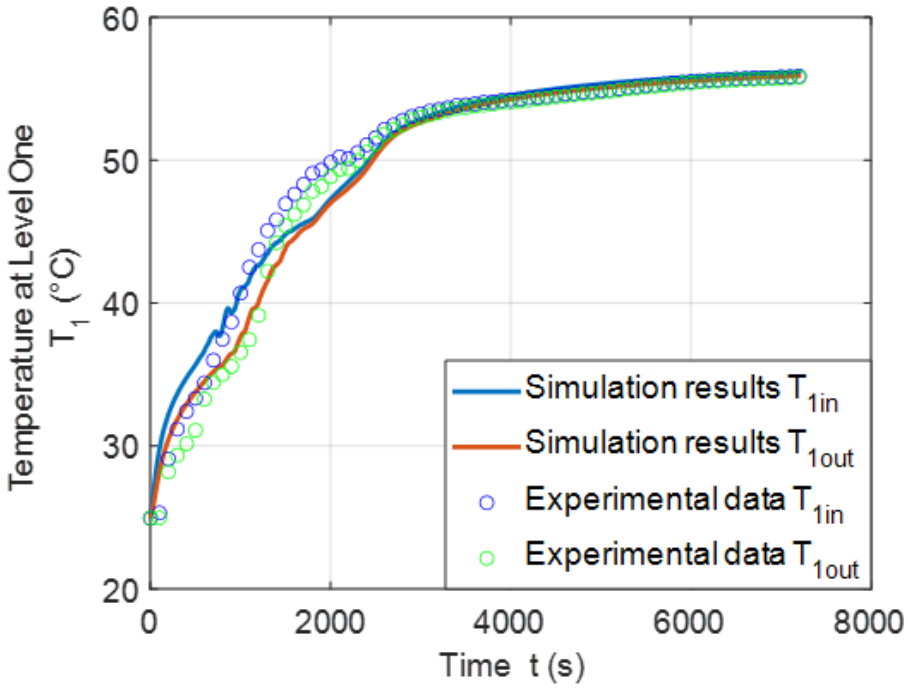

Figure 5.12: Comparison of temperature profiles at level one (L_1).

experiment relatively well below $t = 2000s$ when the natural convection effect is weak, being limited by the area of the liquid zone, and conduction is dominant. As the liquid zone grows with the melting of the solid PCM, convection starts to play an important role. Because of the assumptions and neglecting terms specified in Section 2.1, the simulation can not be identical to the actual liquid flow in the PCM HX. Consequently, the differences between the simulation and the experiment become relatively large after $t = 4000s$. Such a deviation is minimized at level one

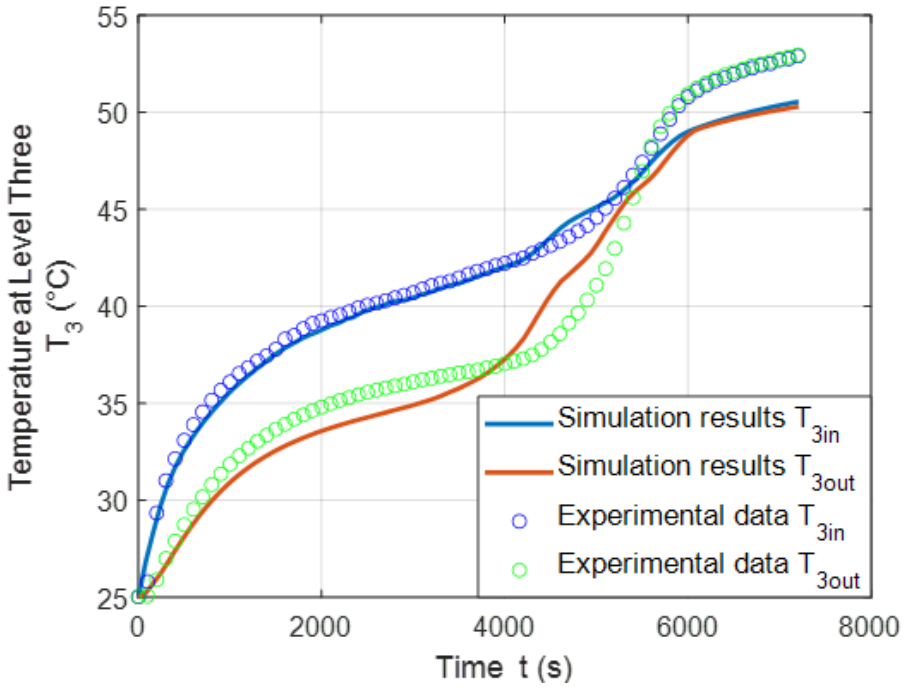

Figure 5.13: Comparison of temperature profiles at level three (L_3).

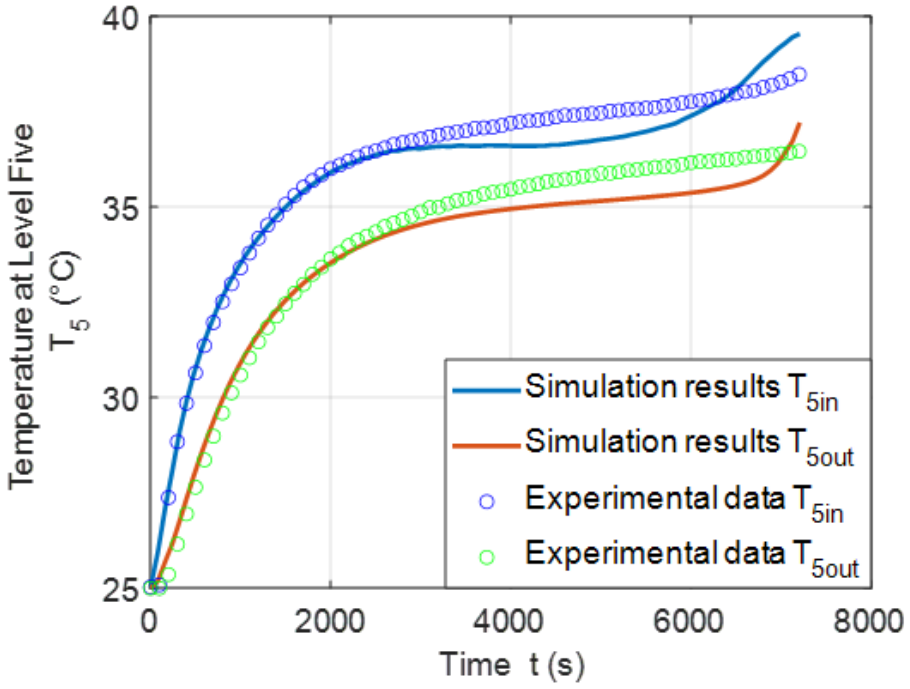

Figure 5.14: Comparison of temperature profiles at level five (L_5).

because of the convection heat transfer, which allows the top part to melt much faster than the rest of the HX, and the temperatures near the top part lift quickly and soon become relatively stable. In addition to, the heat transfer fluid (HTF) loop, the measuring errors from thermocouples, and heat dissipation from the experiment could also lead to the mismatch between the simulation and the experiment. Overall, these deviations for the temperature profiles at these three levels are confined within 10 %, which indicates that the new model is capable of predicting the convective PCM melting in the cylindrical HX relatively well. Moreover, it can be observed that the difference between the temperature profiles at r_i and r_o becomes larger at level three and five compared with level one. This phenomenon is also consistent with convection heat transfer, which results in PCM melting almost simultaneously between the inner and outer layers at the top part. Consequently, the hot fluid from the lower part of the HX is moving up to the top, causing the melting time difference between inner and outer layers of the PCM at lower parts of the HX to increase.

To further validate the model, the average temperature of the PCM in the HX is compared between the simulation and the experiment, as shown in Fig. 5.15. Generally, the deviation of the average temperature of the PCM is kept within 5 %, which is in better agreement with the temperature profiles at the specified levels. This comparison further demonstrates the ability of the new model to predict the heat transfer behavior of the PCM melting in cylindrical HX.

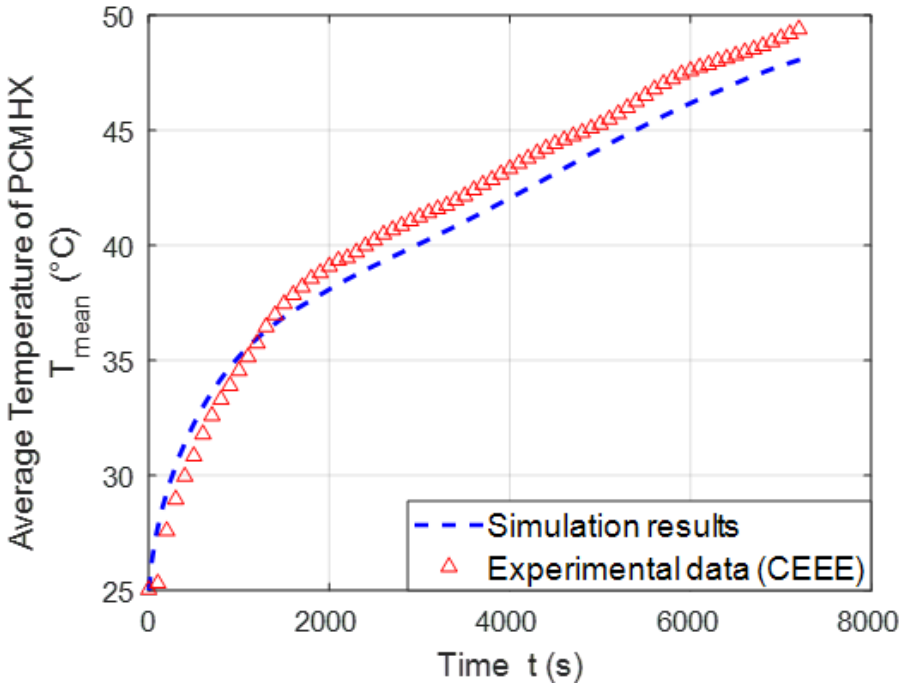

Figure 5.15: Comparison of average temperature in the PCM HX.

5.2.3 PCM Melting with Porous Media in Axisymmetric Coordinates

A case study in this section is conducted to validate the ability of the new axisymmetric model to simulate the porous PCM phase change in a cylindrical HX. The model is set up based on the experiment conducted by Martinelli et. al [91], where the PCM with the copper foam were contained in a vertical annulus, and water was used as the heat transfer fluid (HTF) to heat the PCM from the inner (left) side. According to the detailed PCM HX configuration provided by Martinelli et. al [91], the schematic of the 3D and the half center-sliced cylindrical PCM HX is shown in Fig. 5.16. The initial temperature of the PCM was kept at 15 °C and hot water around 55 °C was pumped from top to bottom during the experiment. A temperature profile of the inner wall ($r = r_i$) is assigned to the left boundary

of the computational domain based on the measured data at the inlet and outlet temperatures of the HTF.

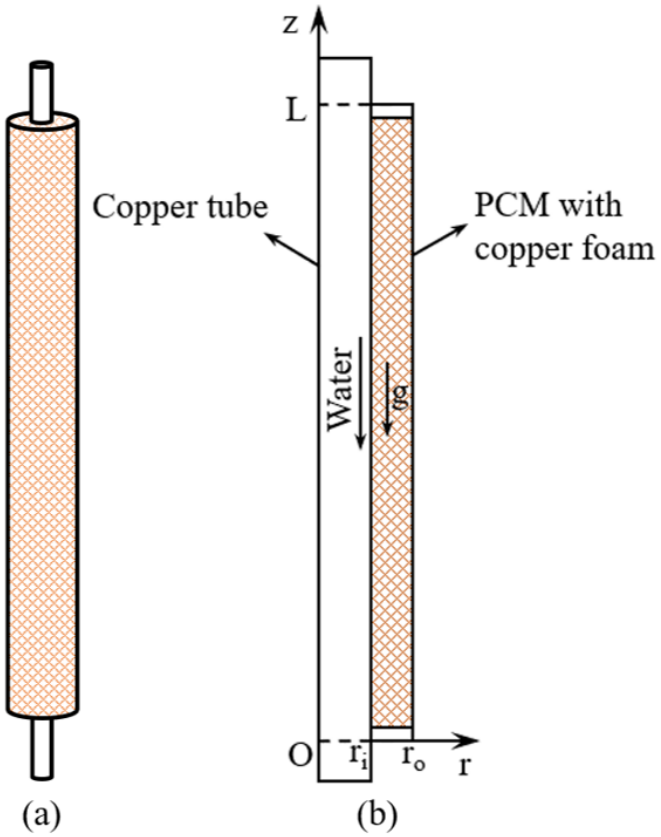

Figure 5.16: Schematic of the cylindrical PCM HX: (a) 3D cylinder sketch and (b) 2D half center-sliced cylinder sketch.

The PCM utilized in this experiment is RT35 HC and its thermophysical properties can be found in the related source [3], as listed in Table 5.9. Additionally, it is worth noting that the actual melting temperature is set to 33.75 °C (T_m) with a temperature glide from 32 °C (T_s) to 35.5 °C (T_l) according to the experimental data [91], which is slightly different from the nominal melting temperature (35 °C) provided by the manufacturer.

Theoretically, the maximum stored energy in the HX filled with current porous

Property	Unit	Value
Nominal melting temperature (T_m)	°C	35
Latent heat of fusion (L_a)	kJ/kg	220
Density (solid) (ρ_s)	kg/m^3	830.9
Density (liquid) (ρ_l)	kg/m^3	778.2
Specific heat capacity (solid) ($c_{p,s}$)	kJ/(kg K)	5.00
Specific heat capacity (liquid) ($c_{p,l}$)	kJ/(kg K)	2.10
Thermal conductivity (solid) (k_s)	W/(m K)	0.65
Thermal conductivity (liquid) (k_l)	W/(m K)	0.166
Thermal expansion coefficient (β)	1/K	0.021
Kinematic viscosity (liquid) (v_l)	mm^2/s	5.654

Table 5.9: PCM Properties of RT35 HC [3].

PCM is given by $E_{total} = E_{pcm} + E_{p,m} = 101.4$kJ, where $E_{pcm} = 96.6$ kJ is the energy stored in RT35HC and $E_{p,m} = 4.8$ kJ is the energy stored in copper foam. To make a comparison, the values of maximum stored energy for other settings of storage materials in the same volume are 106.2 kJ for pure RT35 HC without porous media, 52.7 kJ for pure copper and 62.9 kJ for pure liquid water.

Based on the given PCM properties and the HX configurations, the primary dimensionless numbers are calculated and tabulated in Table 5.10, where the Rayleigh number Ra in this case study is based on the length L of the cylinder. Moreover, the average effective conductivity k_e is calculated as 4.50 W/(m K) from Eq. (2.19) for the porous PCM, neglecting the difference between the solid phase and the liquid phase of the PCM. The simulation results are shown in Fig. 5.17 and Fig. 5.18. Fig. 5.17 demonstrates the streamlines of the liquid PCM and the temperature fields with the PCM melting fronts at various time steps, and Fig. 5.18 compares the temperature profiles of the PCM at selected locations with the experimental data from

Martinelli et. al [91].

For the analysis of the grid independence, additional simulations are conducted with mesh sizes 10×400 and 40×1600 in order to compare with the results with mesh size 20×800. The temperature variations versus time at locations A_t, C_t and E_t are demonstrated in Fig. 5.19. It is obvious that the mesh size 20×800 has been grid-independent.

Dimensionless number	**Value**
Ra_L	1.8×10^9
Pr	55.6
Ste	0.196
Porosity ϕ	0.91

Table 5.10: Dimensionless numbers for the PCM melting with copper foam in the cylindrical HX.

As shown in Fig. 5.17, the top part of the PCM melts in advance due to the top-down charge of the HTF. Moreover, the natural convection in the liquid zone drives the hot liquid PCM near the inner wall from bottom to top, which further accelerates the melting of the upper PCM. Therefore, the uneven evolution of the melting front along with the height, demonstrated by the red solid line in Fig. 5.17, is due to the combination of two factors, i.e., the temperature difference of the HTF and the natural convection effect in the liquid zone.

To further validate the new model, the temperature profiles of the PCM at three different heights A_t, C_t and E_t at radius $r_t = \frac{1}{3}(r_o - r_i)$ are compared with the experimental data measured by the thermocouples at the corresponding locations respectively [91]. As the side-view schematic in Fig. 5.18 demonstrates, the PCM region is evenly divided into five sections (A to E), and A_t, C_t and E_t are located at

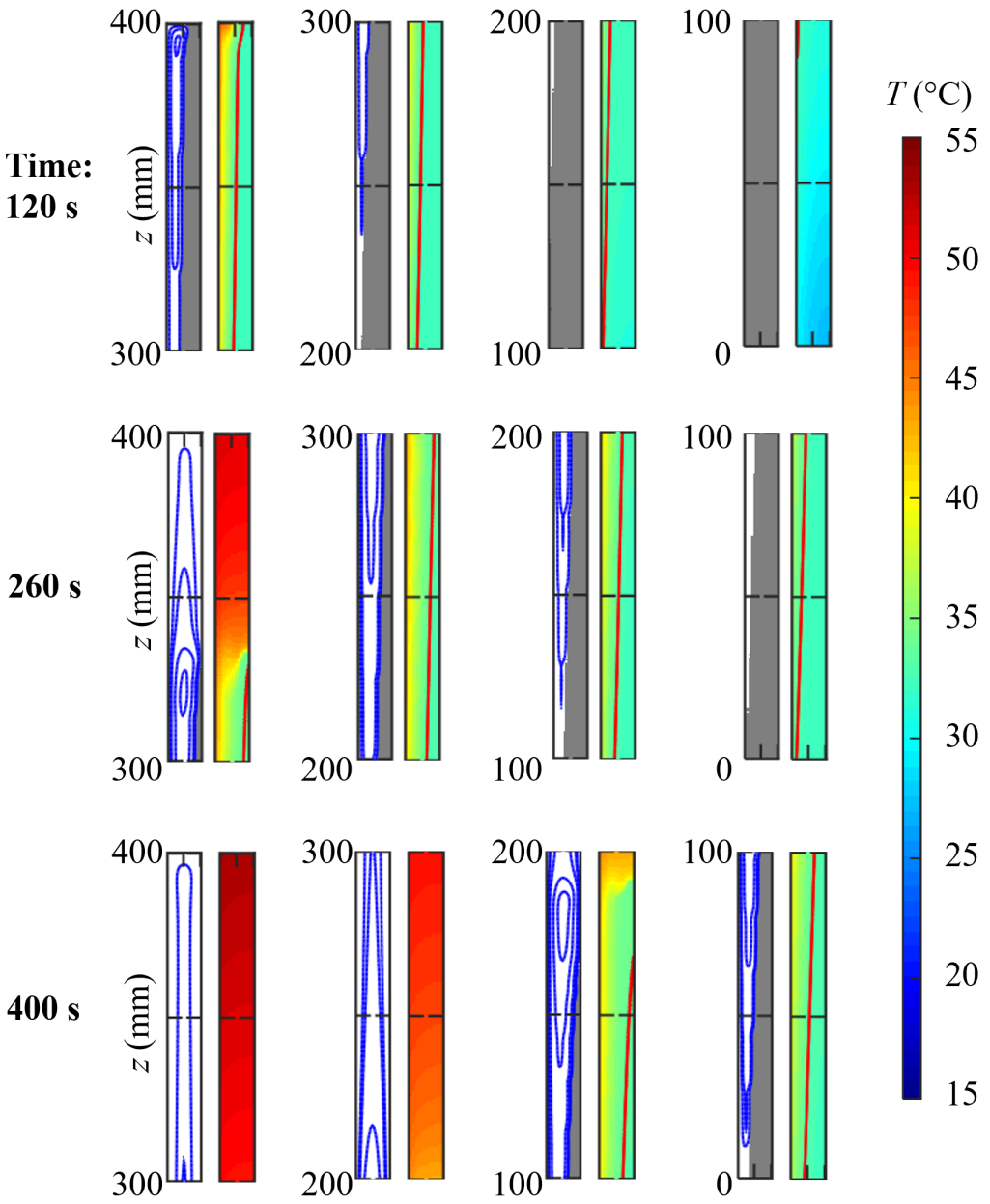

Figure 5.17: Streamlines and temperature fields with the melting fronts (red line) of the PCM with copper foam in the cylindrical HX (divided in length for better visualization).

the central height for each corresponding section. The comparisons are also shown in Fig. 5.18, where the simulation results show a good agreement with the experimental data for the overall heat transfer behavior of the PCM at the selected locations.

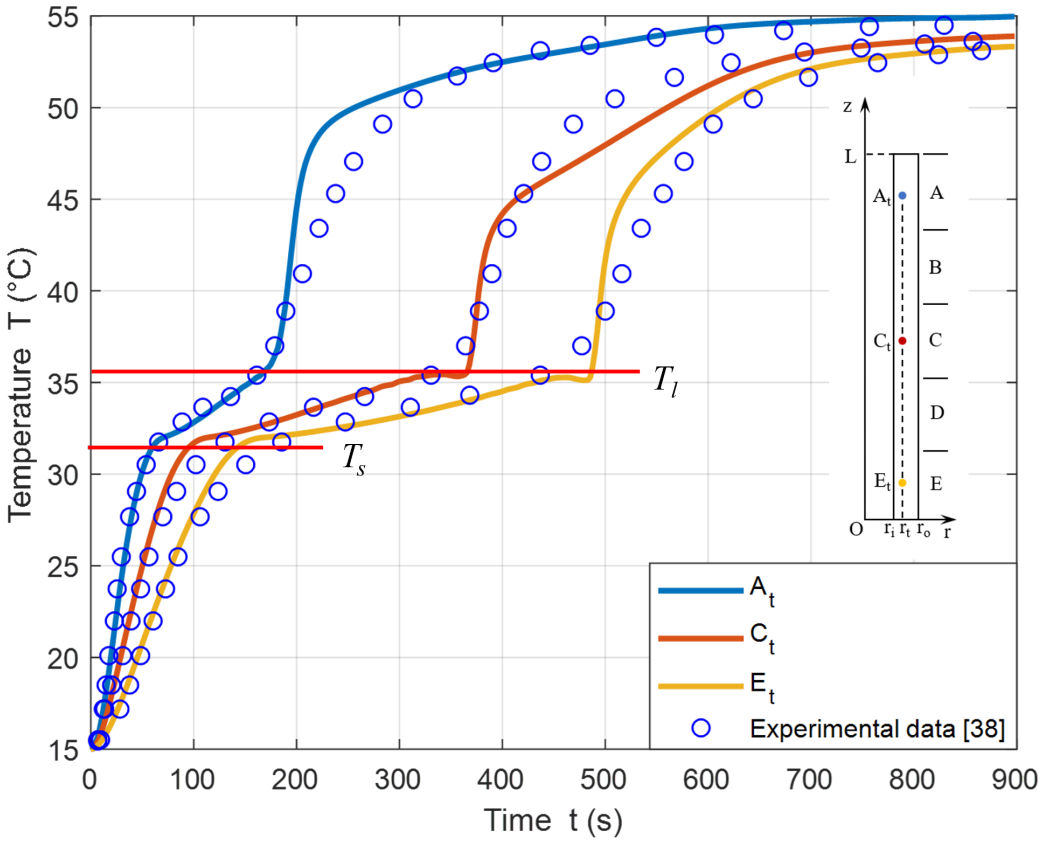

Figure 5.18: Temperature variations of the PCM with copper foam in the cylindrical HX at the selected locations.

With respect to PCM melting, small variations can be observed in Fig. 5.18 at locations C_t and E_t, especially when the PCM both begins to melt (T_s) and has completely melted (T_l). The reason for this discrepancy is that the enthalpy profile used in the model is a correlation that is not accurate enough when entering or leaving the two-phase region compared with the actual enthalpy profile of the PCM. The reason why such a deviation is not found for the PCM at location A_t is owing to its upper location where the intense heat transfer and the energy flowing in around the top part leads to a rapid energy accumulation, which shortens the PCM melting period and meanwhile reduces the error caused by the enthalpy function.

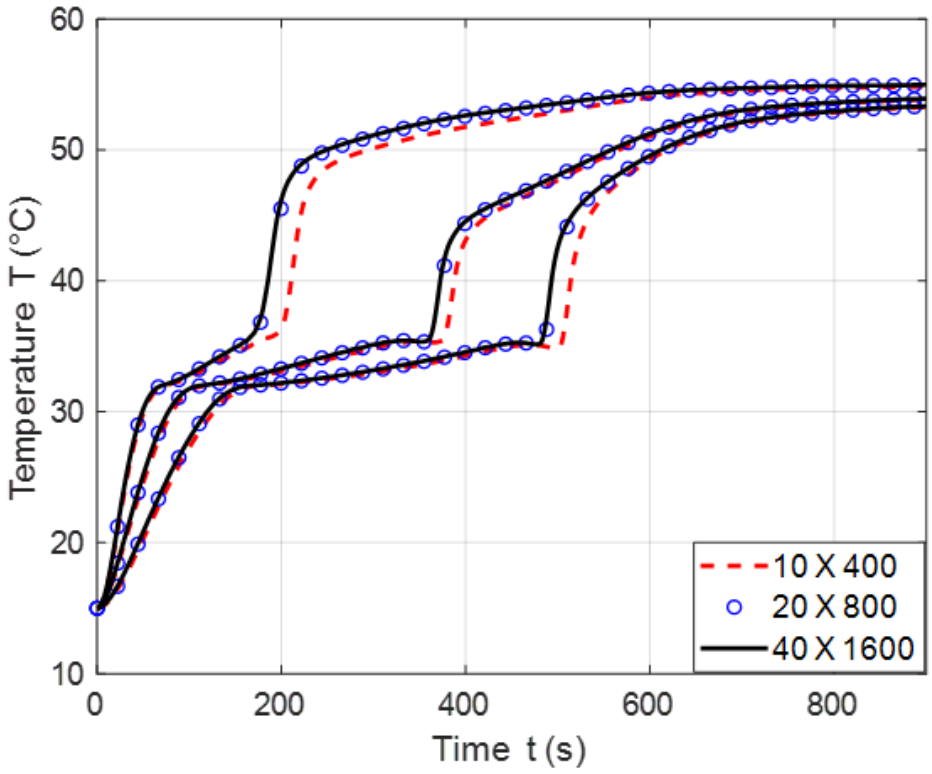

Figure 5.19: Temperature variations versus time at locations A_t, B_t and C_t with mesh size being 10×400, 20×800 and 40×1600.

While for the simulation of the liquid PCM after the melting, though some deviations can be found, the model is able to predict the time when the PCM becomes fully liquid. The deviations in the liquid region could be due to the inaccurate enthalpy profile and the boundary conditions such as the uneven temperature distribution of the HTF and the heat dissipation to the surroundings. More precise temperature profiles are expected to be obtained if the issues mentioned above could be solved. Nevertheless, the prediction error is confined within 10 % which indicates that the developed asymmetric model is capable of predicting the heat transfer behavior of the porous PCM in cylindrical HX.

A further evaluation of the effect of natural convection on the porous PCM

is performed based on the validation case in this section. Generally, adding porous material to the PCM can enhance the heat transfer because of its high thermal conductivity. Meanwhile, it also exerts more drag which slows down the motion of the liquid PCM and thereby dampening the effect of convection on PCM melting. Some porous media with low porosity can even neglect the effect of natural convection because liquid PCM is confined within the cavities of the porous media. But for those porous media that have higher porosity, such as the case in this section, natural convection still plays an important role. Because of the porous media, the natural convection effect can be different from that of the pure PCM. Therefore further analysis is required to quantitatively estimate the effect of natural convection on porous PCM.

For PCM melting, the Rayleigh number (Ra) mainly determines the intensity of natural convection. Moreover, the geometry of the model, as well as the PCM melting behavior, also play a role. To clearly identify the underlying physical mechanisms, further analysis is carried out using the same geometry as was used for the validation cases described above. The strength of natural convection will be controlled by changing Ra in the simulations. There are several terms in Ra that can be adjusted, e.g., temperature difference ΔT, viscosity v, thermal diffusivity α and thermal expansion coefficient β. From an application point of view, changing these terms is equivalent to varying the boundary and initial conditions of temperature, as well as replacing a new PCM with different fluid and thermal properties. Several simulations that adjust different terms are conducted and the results indicate that the heat transfer behavior almost remains the same under the same Ra, as

expected. Therefore, a parametric study based on Ra is reasonable. Additionally, the Rayleigh number in the following parametric study is also based on the length L of the cylinder.

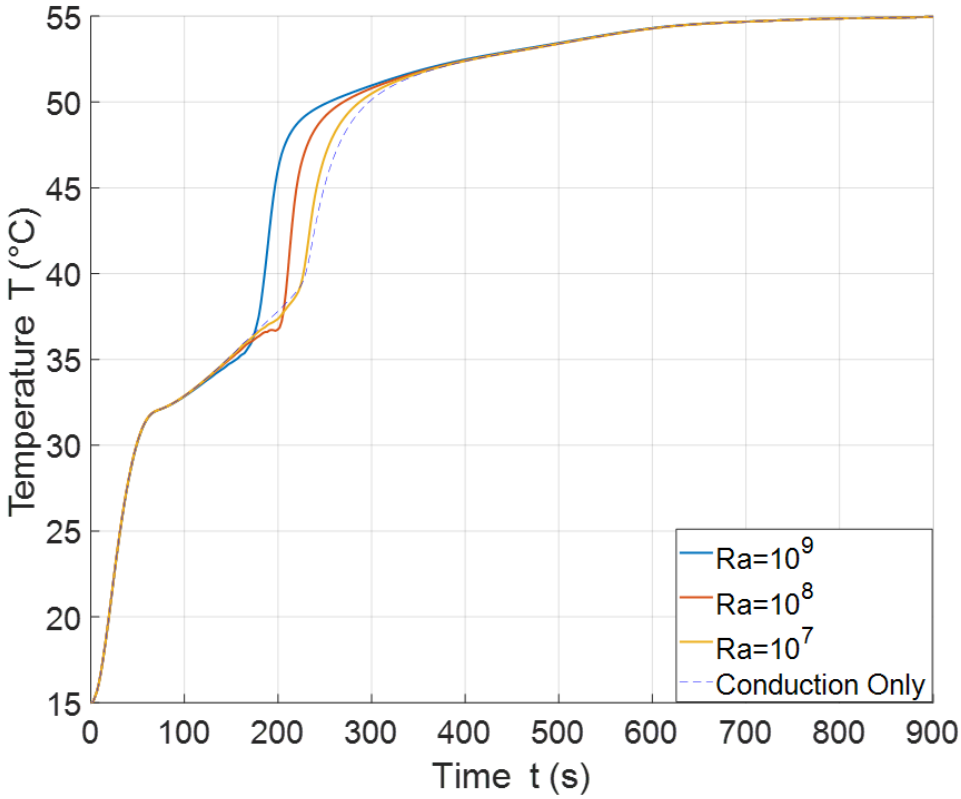

Figure 5.20: Comparison of the temperature profiles at $Ra = 10^9, 10^8$ and 10^7 with those of the PCM conduction only at location A_t.

For this parametric study, Ra is adjusted by changing the thermal expansion coefficient β as it directly contributes to the buoyancy force which drives natural convection. Fig. 5.20 - Fig. 5.22 compare the temperature profiles at three locations A_t, C_t and E_t of the HX at various Ra with those of pure PCM conduction. The three locations A_t, C_t and E_t shown in Fig. 5.18 represents the top, middle and bottom part of the HX. From these three figures, a clear trend can be observed that the PCM melts faster at higher Ra among the three parts of the HX. Another

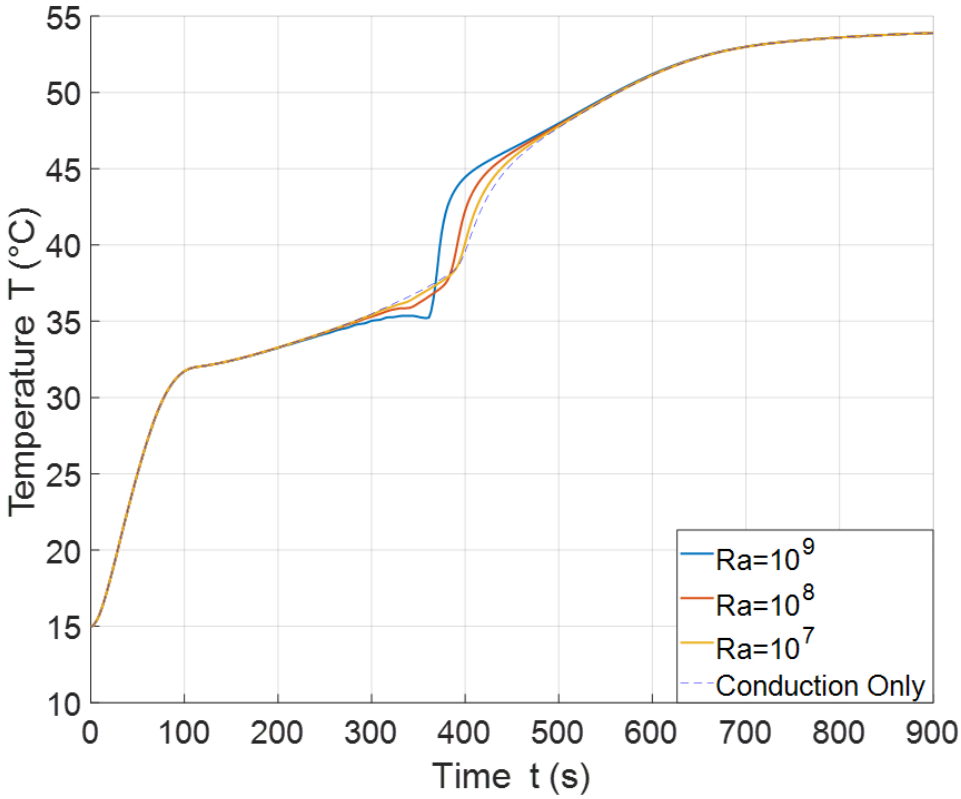

Figure 5.21: Comparison of the temperature profiles at $Ra = 10^9, 10^8$ and 10^7 with those of the PCM conduction only at location C_t.

phenomenon found in the middle (C_t) and bottom (E_t) parts of the HX is that a higher value of Ra results in a lower average PCM temperature during the melting process. This is due to the uneven temperature distribution caused by natural convection. Higher Ra results in stronger nature convection, which can bring more hot liquid PCM to the top and then cause the temperature at the middle and bottom to remain low. This analysis can be corroborated by the temperature profile at the top part (A_t) where the difference in temperature during melting is much smaller compared with the rest of the two parts.

Fig. 5.23 displays the calculated cumulative energy in PCM versus time for different Ra and the pure conduction case. The final stored energy in the PCM is

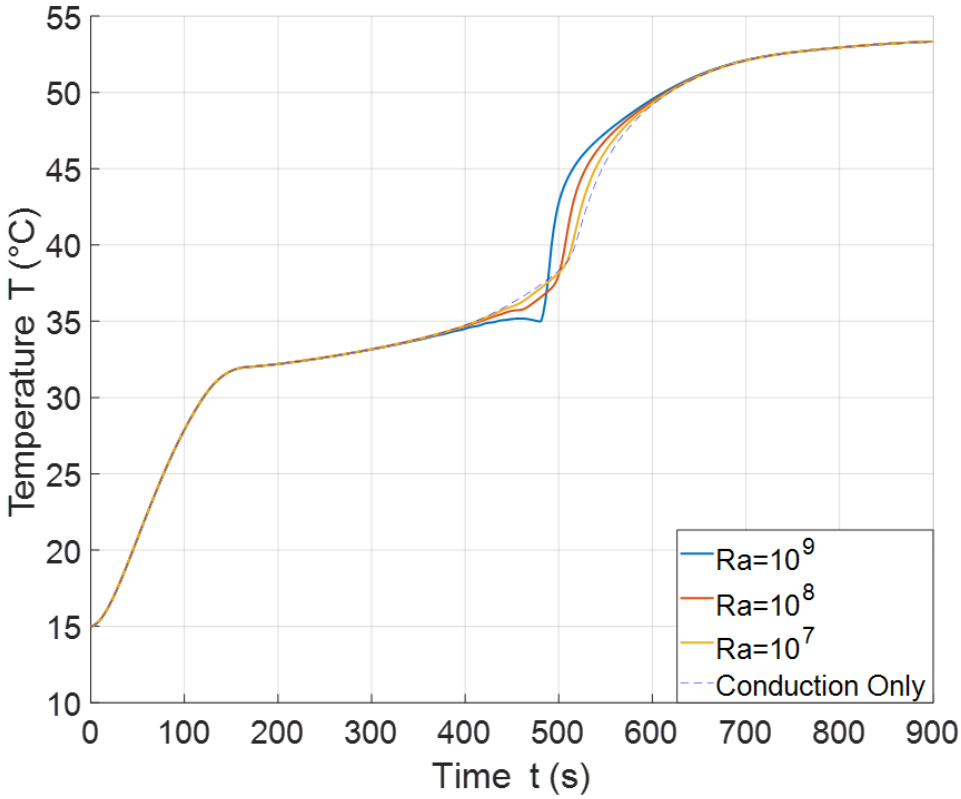

Figure 5.22: Comparison of the temperature profiles at $Ra = 10^9, 10^8$ and 10^7 with those of the PCM conduction only at location E_t.

about $E_{fpcm} = 83\ kJ$. It is reasonable to set $E_{pcm} >= 0.9E_{fpcm}$ as the condition for determining whether the PCM has fully melted. By comparing the time at which the energy satisfies this criterion, it can be concluded that natural convection can enhance melting by 10 % on average for the HX configuration specified in Fig. 5.16.

5.2.4 PCM Melting with Conducting Fins in Axisymmetric Coordinates

The new axisymmetric model is validated with respect to its capability for simulating PCM melting in cylindrical HX with and without porous media, as demon-

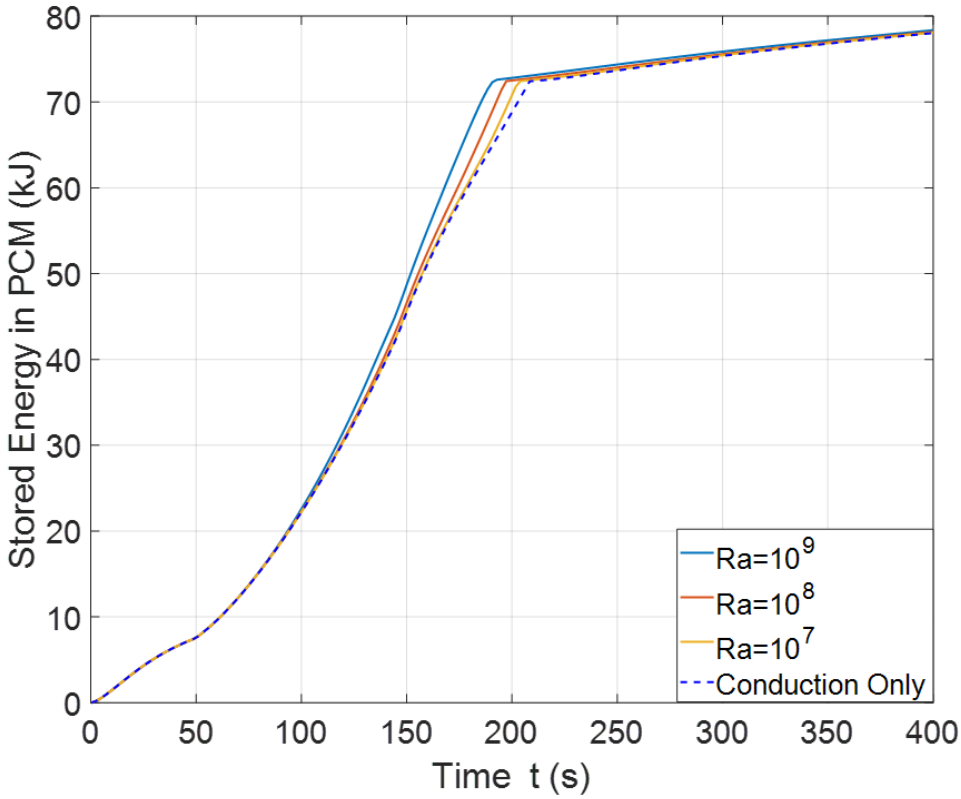

Figure 5.23: Comparison of the cumulative energy stored in PCM versus time.

strated in Section 5.2.2 and Section 5.2.3. The simulations presented in this section are carried out to validate the conjugate heat transfer model for simulating the PCM phase change with conducting fins. The model is set up based on the experiment conducted by CEEE group. The detailed geometry and experimental settings are provided by J. Yang et al. [6]. To better demonstrate this case study, a figure is given here as Fig. 5.24 to show the PCM HX with fins in a general form, and this schematic does not represent the exact HX from our simulation and the corresponding experiment.

The conducting fins and the wall of the HTF pipe shown in Fig. 5.24 are modeled as a whole, based on the conjugate thermal LBM introduced in Section 2.4

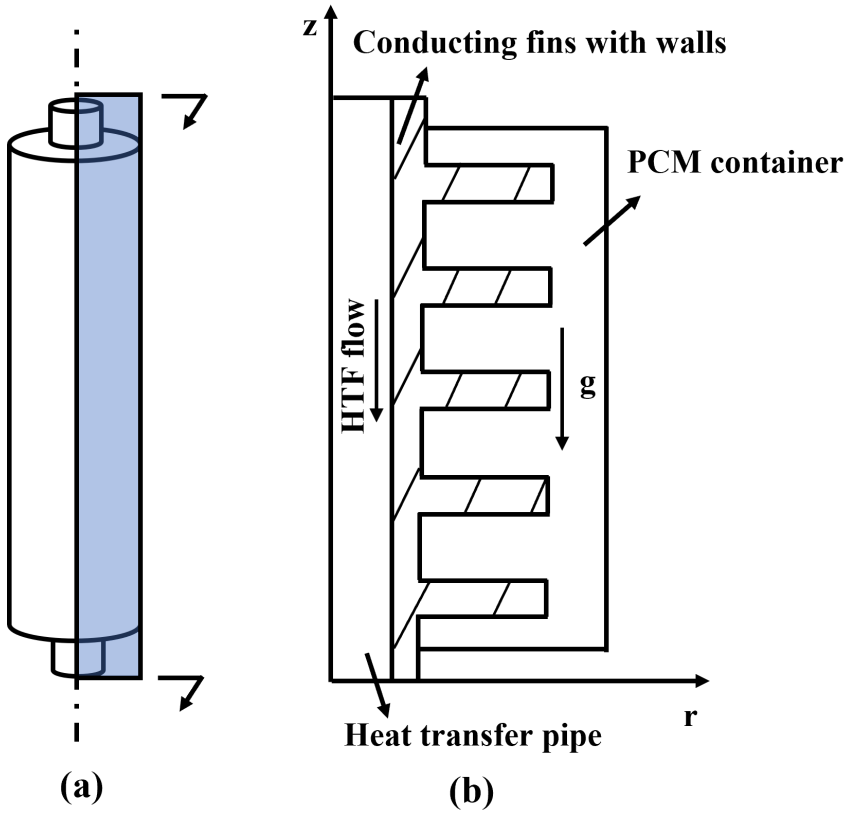

Figure 5.24: Schematic of the PCM HX with conducting fins: (a) 3D cylinder sketch and (b) 2D half center-sliced cylinder sketch.

and Section 4.4.3. By integrating this with the enthalpy-based MRT-LBM for PCM, together with the 1D HTF flow model for determining the wall temperatures on the left boundary, the entire PCM HX with fins can be modeled.

The PCM used in the HX is RT35, which is different from RT35 HC, and its properties are given in Table 5.11 [4,5]. The HTF flow is pumped through the center pipe from the bottom to the top. Moreover, Table 5.12 summarizes the geometric settings of the HX [6] and Table 5.13 gives other important settings, including the temperature settings and the critical dimensionless numbers.

The simulation is conducted with mesh size $N_r \times N_z = 32 \times 500$, and the results

Property	Unit	Value
Nominal melting temperature (T_m)	°C	35
Latent heat of fusion (L_a)	kJ/kg	157
Density (solid) (ρ_s)	kg/m^3	880
Density (liquid) (ρ_l)	kg/m^3	760
Specific heat capacity (solid) ($c_{p,s}$)	kJ/(kg K)	1.8
Specific heat capacity (liquid) ($c_{p,l}$)	kJ/(kg K)	2.4
Thermal conductivity (solid) (k_s)	W/(m K)	0.2
Thermal conductivity (liquid) (k_l)	W/(m K)	0.2
Thermal expansion coefficient (β)	1/K	0.0006
Kinematic viscosity (liquid) (v_l)	mm^2/s	3.3

Table 5.11: PCM Properties of RT35 [4, 5].

Geometry	Value
Length of the HX (L)	285 mm
Inner radius of the PCM container (r_i)	6.35 mm
Outer radius of the PCM container (r_o)	22.25 mm
Wall thickness of the HTF pipe (b_p)	1.5 mm
Number of fins (N_{fin})	19
Fin radius (r_{fin})	21.225 mm
Fin spacing (t_{fin})	12.7 mm
Fin thickness (b_{fin})	1.5 mm

Table 5.12: Geometric Settings of the Finned HX [6].

shown in Fig. 5.25 display the streamlines in the liquid zone and the temperature fields for the PCM and the fins with the wall at various Fourier numbers (Fo) from 1.2 to 5.0. It can be observed that adding fins increases the effective heat transfer area, which enhances PCM melting. Moreover, the fins confine the convection flow in small blocks, which dampens the effect of convection, but makes the temperature distributions more uniform compared to that in pure PCM.

A further comparison of the temperature profiles at two locations is shown in Fig. 5.26, where the detailed locations of $T_{18\text{-}out}$ and $T_{2\text{-}out}$ can be found in the

Parameter	Value
Initial temperature (T_i)	25.2 °C
Inlet temperature (T_{inlet})	54.5 °C
Rayleigh number based on length (Ra_L)	6.04×10^9
Rayleigh number based on radius gap (Ra_R)	1.05×10^6
Prandtl number (Pr)	22.6
Stefan number (Ste)	1.0

Table 5.13: Parametric Settings for the PCM Melting in the Finned HX.

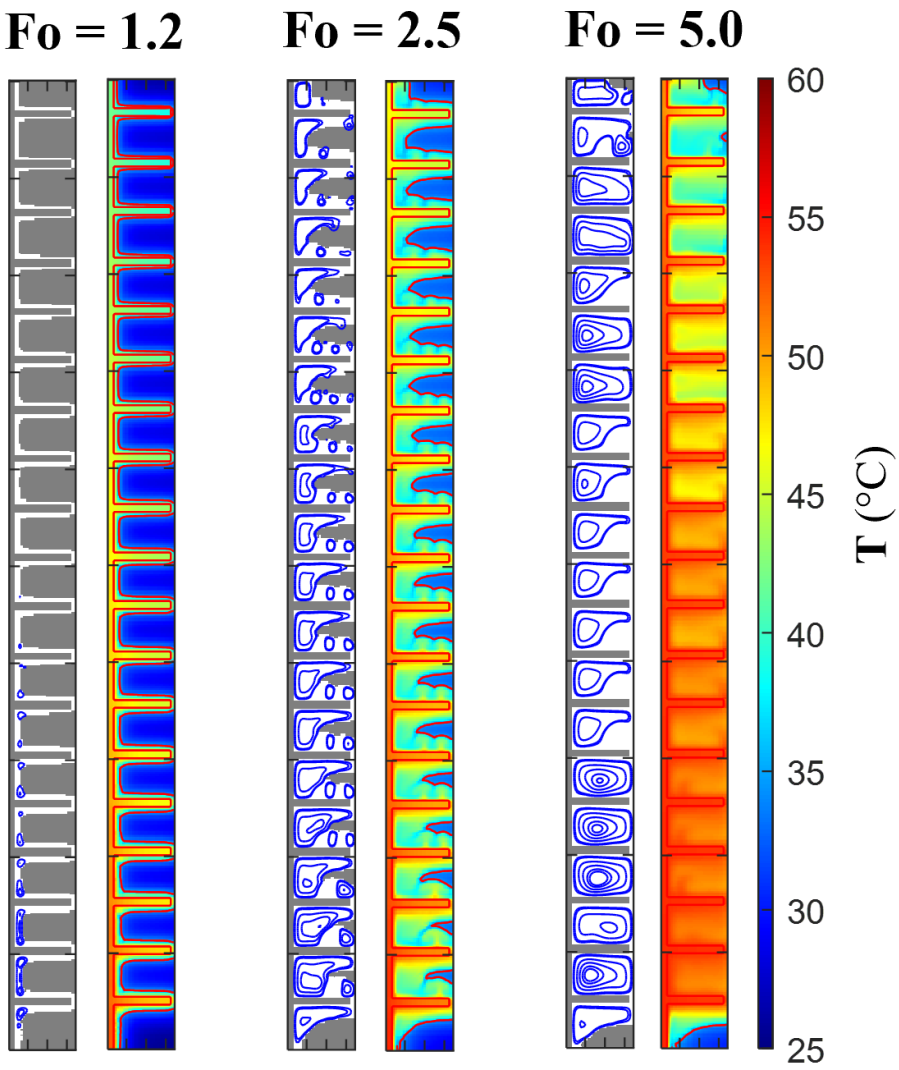

Figure 5.25: Streamlines and temperature fields of the finned HX at $Fo = 1.2$, 2.5 and 5.0.

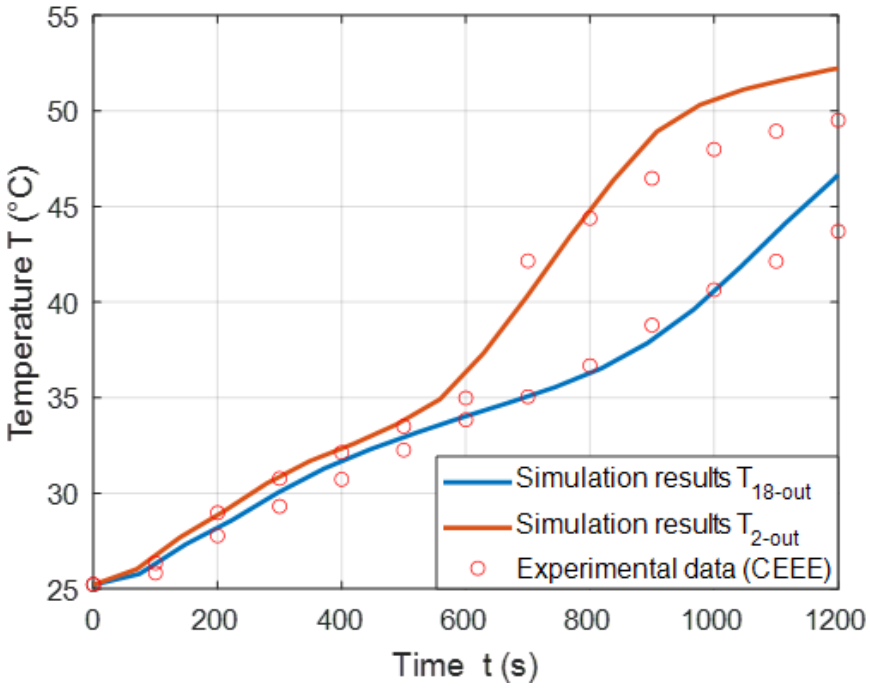

Figure 5.26: Comparison of the temperature profiles at locations $T_{18\text{-}out}$ and $T_{2\text{-}out}$ with the experimental data [6].

experiment from Yang, J. et al. [6]. Generally, $T_{18\text{-}out}$ is near the top between the 17th and 18th fins, and $T_{2\text{-}out}$ is just above the bottom between the 1st and 2nd fins. Both the simulation results and the experimental data indicate the difference between the temperatures at these two locations, which is mainly because of the uneven temperature distributions of the HTF flow since the convection heat transfer is extremely limited by the conducting fins in this case. Overall, the temperature profiles have a good match despite the small deviations after $t = 800s$. And more validations and case studies of the conjugate phase change model are still necessary to further proves its capability of solving the PCM with different types of fins in the HX.

5.3 Scaling Analysis of the Parallel LBM Scheme

In Section 5.1 and Section 5.2, the developed enthalpy-based DDF-MRT lattice Boltzmann model is verified and validated by several case studies. In this section, a scaling analysis is performed to test the parallel LBM scheme introduced in Section 4.6. The case study of porous PCM melting in cylindrical HX as discussed in Section 5.2.3 is chosen as the baseline, which simulates 900 seconds of PCM melting with the mesh size 20×800. Both the series code and parallel code are developed for this case study and operated on the high performance computing (HPC) resources from University of Maryland. Based on the computational time for different mesh sizes and operating cores, both the strong and weak scaling analyses are conducted to evaluate the developed parallel scheme in solving the solid-liquid phase change.

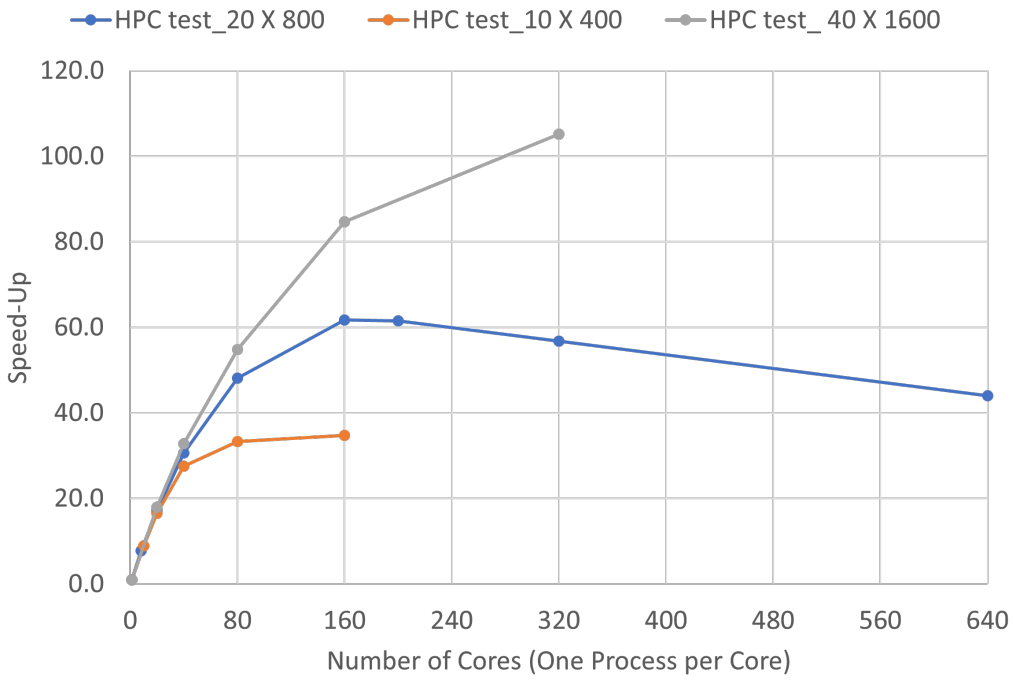

Figure 5.27: Strong scaling analysis of the parallel LBM scheme.

The strong scaling analysis refers to the speed-up at different operating cores, where the speed-up is defined as the computational time using the current number of cores over the computational time for series code (one core). Moreover, each core only allows one process in order to better perform the analysis. Then the strong scaling analysis can be conducted by increasing the number of operating cores and then calculating the speed-up for each running case, as shown in Fig. 5.27. Three mesh sizes are tested, and the results are represented by colored lines. Theoretically, the speed-up should be linear. However, due to the series part in the LBM parallel code, it cannot be perfectly parallel. Therefore the speed-up in practice will gradually slow down and may even decline as the number of cores increases, which is consistent with the trend of the lines in Fig. 5.27. Besides, it can also be observed that the rate of the speed-up increases as the size of the model becomes larger, which indicates that the optimal number of operating cores could be higher for larger mesh sizes. In general, 40 operating cores, seems to be an effective working load for all the mesh sizes in this case study.

The weak scaling analysis is carried out by increasing the mesh size and operating cores in the same proportion. So the computational time of the running case should remain the same ideally. However, this does not happen for the same reason as the strong scaling analysis as mentioned above. Therefore the computation time should gradually lift when increasing the mesh sizes and operating cores, as Fig. 5.28 shows. Although the computational time increases throughout, the growth is small below the mesh size of 20×800 with 40 cores and it becomes rapid after that point. The result of the weak scaling analysis is consistent with that of the strong scaling

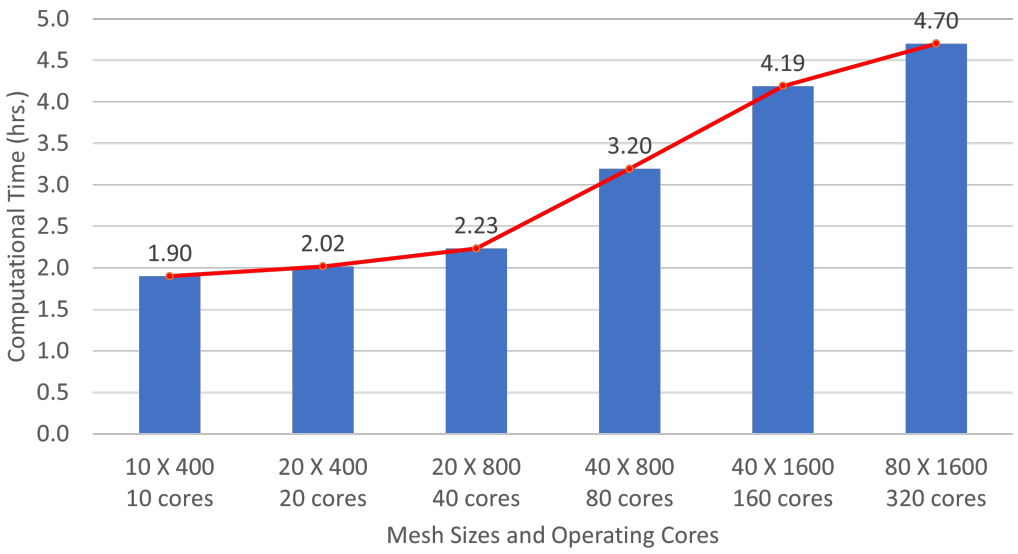

Figure 5.28: Weak scaling analysis of the parallel LBM scheme.

analysis, which shows that the benefit of using parallel computation to speed up the calculation. Moreover, the analyses of the parallel LBM allows the determination of the optimal number of processors for a given mesh size, which makes it possible to perform parametric studies of various PCM HXs in a time-efficient way.

5.4 Chapter Summary

In this chapter, both the numerical verifications in Section 5.1 and validations in Section 5.2 are demonstrated, and the results are discussed. Among them, the porous PCM melting in the Cartesian cavity (Section 5.1.2), PCM melting in cylindrical HX with and without porous media (Section 5.2.2 and Section 5.2.3), and PCM melting with conducting fins (Section 5.2.4) are essential for the parametric studies presented in Chapter 6 and analyses discussed in Chapter 7. The results indicate that the new model is capable of simulating PCM phase change both in

Cartesian and axisymmetric coordinates, with and without porous media and conducting fins, and from low to high Rayleigh numbers. Moreover, Section 5.3 in this chapter introduces the scaling analyses of the parallel scheme, which is also one of the key techniques to perform the various numerical studies of the PCM HXs.

Method	**CPU usage**	**Computational time (hrs.)**
Sequential LBM	1 core	65.3
Parallel LBM one	8 cores	8.6
Parallel LBM two	40 cores	2.2

Table 5.14: Computational Time for the Simulation of Porous PCM Melting in Cylindrical HX.

Table 5.14 provides the computational time for the simulation of 900 seconds porous PCM melting in cylindrical HX introduced in Section 5.2.3 using basic sequential LBM or newly developed parallel LBM. The computational time for other verification and validation cases in this chapter as well as the parametric studies in Chapter 6 is in the same magnitude as Table 5.14 for the PCM melting in the same time period.

Chapter 6: Parametric Studies of the PCM HX using Axisymmetric DDF-LBM

The study of porous PCM in the cylindrical HX discussed in Section 5.2.3, indicates that the enhancement of PCM melting can only be up to 10 % by increasing the Rayleigh number. From the comparisons of the figures in Section 5.2.3, it can be observed that the temperature field is mainly governed by conduction and heat transfer is limited by the inlet temperature of the HTF. Consequently, natural convection has a limited effect on enhancing the heat transfer. In fact, the effect of natural convection on PCM melting can be limited by several factors such as the HX geometry, the drag force due to the presence of the porous media, the variation of the HTF temperatures and heat dissipation at the outer walls. In order to further study the natural convection effect on PCM melting under different conditions, several parametric studies are conducted, which are demonstrated in the following sections.

6.1 Effect of Aspect Ratio

In this section, a parametric study is introduced, focusing on the PCM melting in the HX with different aspect ratios A under various Rayleigh numbers Ra.

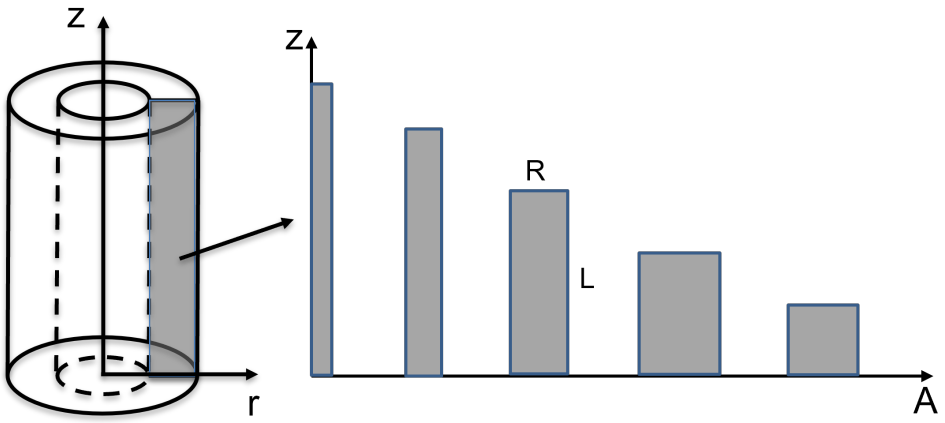

Figure 6.1: Schematic of the cylindrical HX at various aspect ratios.

The schematic of the cylindrical HX at various aspect ratios is given in Fig. 6.1, where the aspect ratio A in this parametric study is defined as $A = R/L$, where the radius gap R can be calculated by $R = r_o - r_i$. Based on this definition, the HX with smaller aspect ratios turns out to be more slender, while the 2D shape of the PCM domain in the HX becomes more like a rectangle as A approaches one. The parametric study in this section is performed at five aspect ratios selected as $A =$ 1.0, 0.75, 0.5, 0.25, and 0.05, and meanwhile maintaining the total volume of the HX as constant so that the theoretical maximum energy storage for different cases can be the same.

For the PCM HX with each aspect ratio, the simulation is conducted for several Rayleigh numbers, which indicates the variation of the convection heat transfer conditions. It is worth noting that the Rayleigh numbers (Ra) in this parametric study are based on the radius gap R, and the variation of Ra is achieved by adjusting the thermal expansion coefficient β, which reflects the strength of the buoyancy force.

The parametric settings are similar to those in Section 5.2.2. The PCM prop-

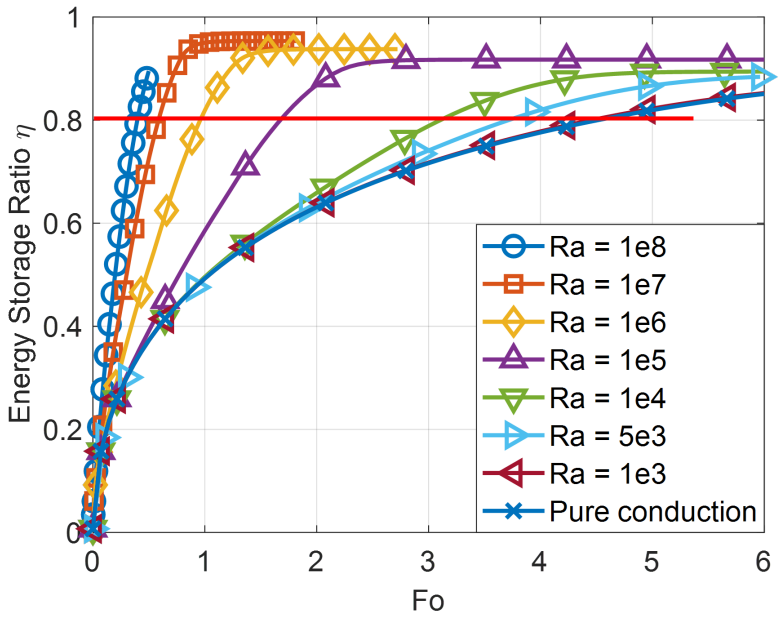

Figure 6.2: Energy storage ratio (η) versus Fourier number (Fo) at various Rayleigh numbers (Ra) for aspect ratio $A = 1.0$.

erties are set based on PT37, though the exact settings in the simulation differ as the Rayleigh number changes. The purpose of using PT37 as a basis is to consider the real paraffin PCM properties so that the parametric settings can be more practical. The energy storage ratio η, defined as the current energy stored in the PCM HX over the theoretical maximum energy that the HX can attain, is plotted over the Fourier numbers (Fo) defined as $Fo = \alpha t/R^2$, which can be treated as the dimensionless time. The plot for $A = 1.0$ is shown as Fig. 6.2, where different curves refer to the energy storage ratios versus Fo at corresponding Ra. The trend indicates that melting is accelerated as convection heat transfer becomes stronger. By setting a portion of the theoretical maximum energy storage as a criterion to evaluate the HX performance, such as 80 %, denoted by the red bar in Fig. 6.2, the accelerations of the PCM melting at different Ra can be quantified by comparing

the Fo (dimensionless time) at which the energy storage ratios reach 80 %.

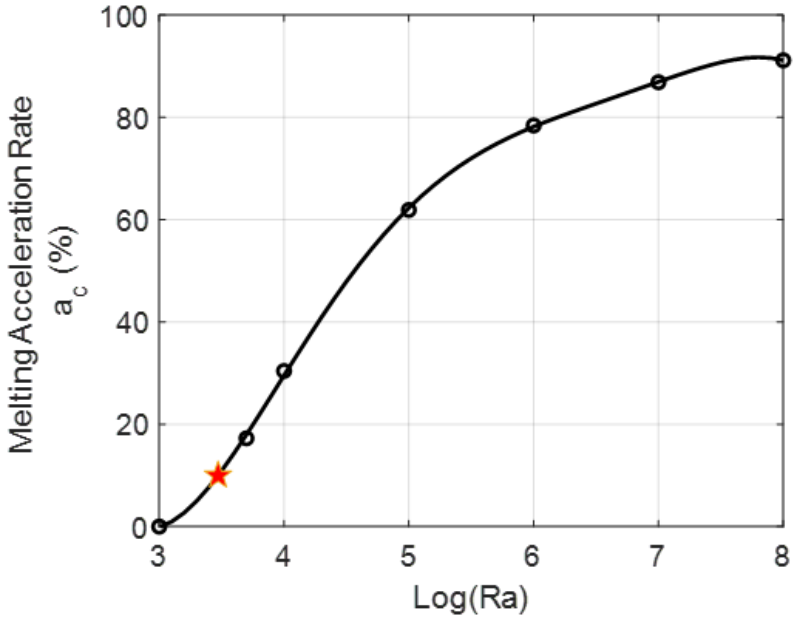

Figure 6.3: Acceleration of melting for different Rayleigh numbers (Ra) at $\eta = 0.8$ and $A = 1.0$.

Based on the concept above, melting accelerations at various Ra can be obtained, as shown in Fig. 6.3, where the y-axis denotes the acceleration rate a_c of the PCM melting, defined as the $a_c = (Fo_{cv,0.8} - Fo_{cd,0.8})/Fo_{cd,0.8}$, where $Fo_{cv,0.8}$ denotes the Fo at which $\eta = 0.8$ for the convection cases, while $Fo_{cd,0.8}$ represents the Fo at which $\eta = 0.8$ for the pure conduction case. The setting of the criterion can be adjusted, and it is set to 0.8 in this parametric study. For a better demonstration of the curve, the x-axis is modified to be $log(Ra)$.

The red star in Fig. 6.3 denotes $a_c = 10\%$, and its corresponding Ra can be defined as a threshold Rayleigh number (Ra_{dc}), above which the acceleration of the PCM melting is larger than 10 %, and thus the convection heat transfer becomes important or starts to play an important role. For the cases $Ra < Ra_{dc}$, convection

has limited effect on melting and can be neglected for the modeling of heat transfer in the PCM HX.

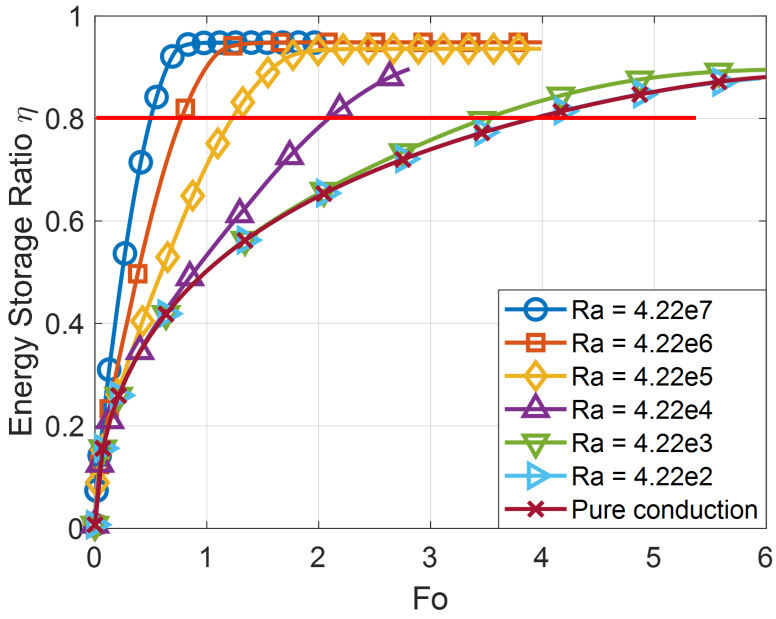

Figure 6.4: Energy storage ratio (η) versus Fourier number (Fo) at various Rayleigh numbers (Ra) for aspect ratio $A = 0.75$.

Fig. 6.2 and Fig. 6.3 are for $A = 1.0$, while other cases are shown from Fig. 6.4 to Fig. 6.7, which also indicate the melting of PCM becomes faster as Ra increases for all of the aspect ratios. The melting acceleration a_c is calculated based on the curves from Fig. 6.2 to Fig. 6.7 for each aspect ratio, and the details are shown in Fig. 6.8, where each line refers to an acceleration curve of its corresponding aspect ratio. The criterion for all the curves is set to 0.8 for consistency. From the figure, a clear trend can be found that the acceleration curve starts to shift to the right as the aspect ratio becomes smaller, which indicates that higher Ra is required for the HX with a smaller aspect ratio to achieve the same acceleration rate for the PCM melting. But this phenomenon does not indicate that the HX with a smaller aspect

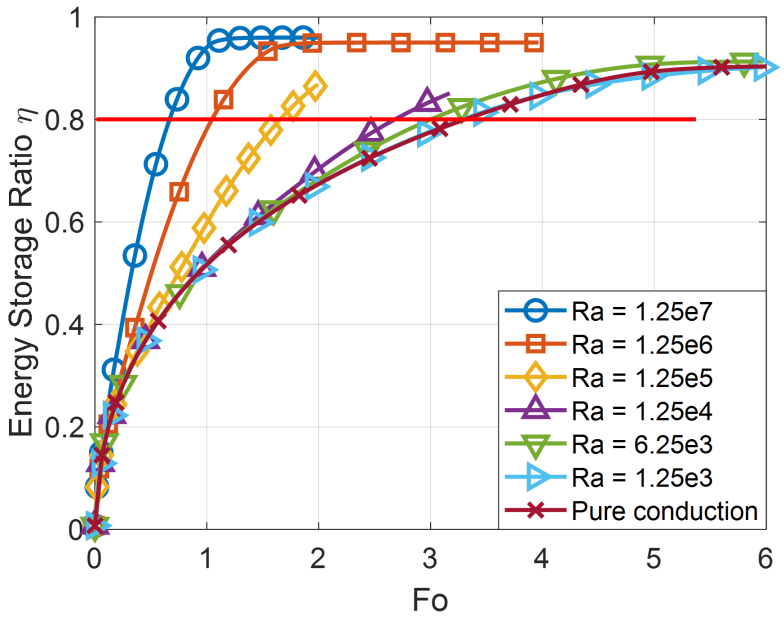

Figure 6.5: Energy storage ratio (η) versus Fourier number (Fo) at various Rayleigh numbers (Ra) for aspect ratio $A = 0.5$.

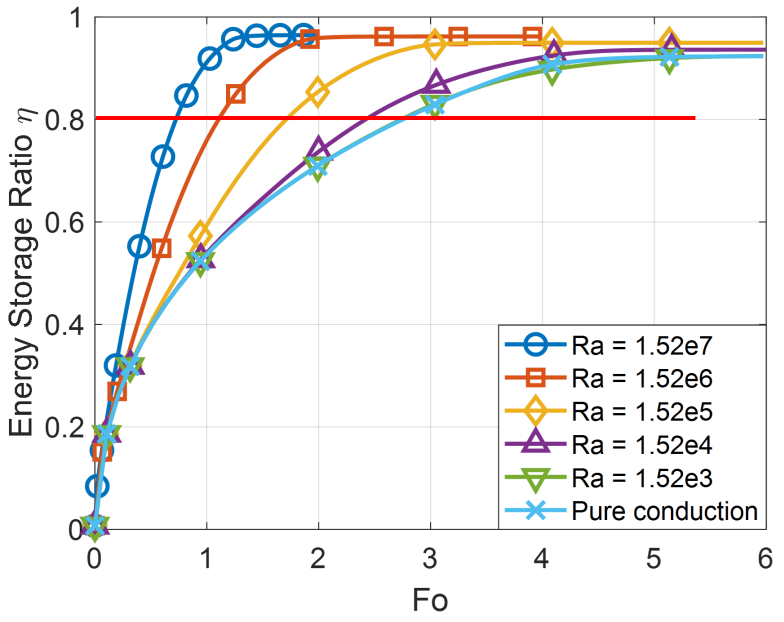

Figure 6.6: Energy storage ratio (η) versus Fourier number (Fo) at various Rayleigh numbers (Ra) for aspect ratio $A = 0.25$.

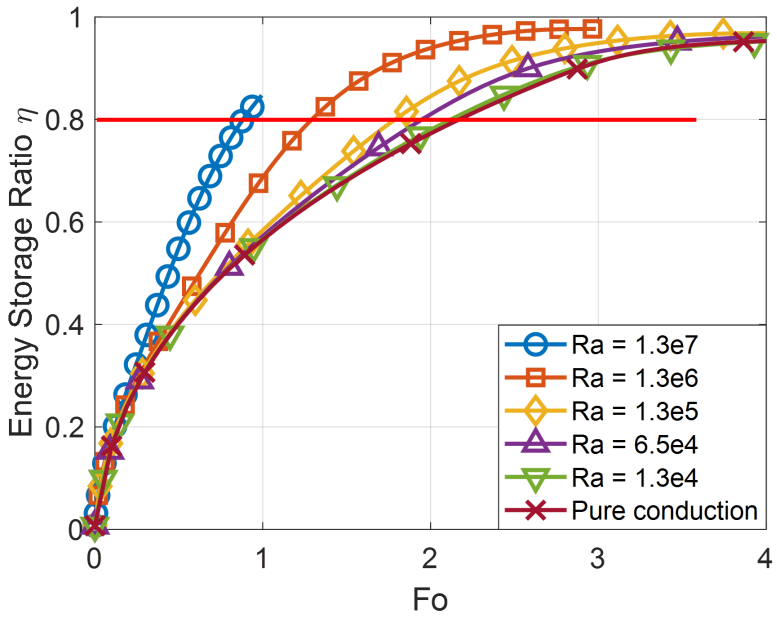

Figure 6.7: Energy storage ratio (η) versus Fourier number (Fo) at various Rayleigh numbers (Ra) for aspect ratio $A = 0.05$.

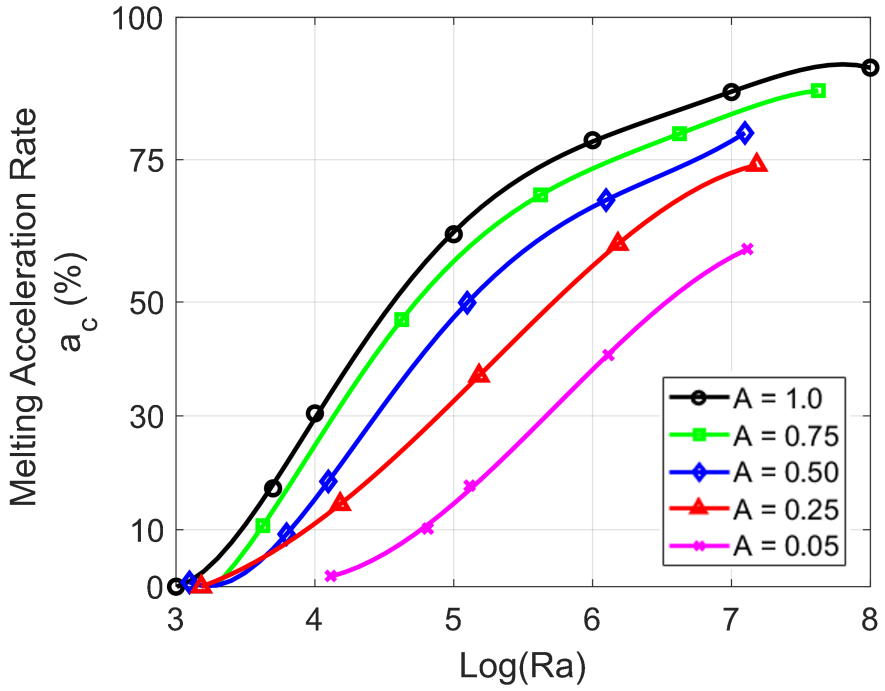

Figure 6.8: Acceleration of melting for different Rayleigh numbers (Ra) at $\eta = 0.8$ with various aspect ratios $A = 1.0, 0.75, 0.5, 0.25, 0.05$.

ratio is less efficient in the convective PCM melting, since the rate of acceleration is also determined by the pure conduction curve, and it can be different for each aspect ratio. Therefore, the acceleration curve for each aspect ratio in Fig. 6.8 actually identifies how much the melting can be accelerated compared to its pure conduction curve, correspondingly. In other words, the trend in this figure, can not determine which aspect ratio is better for the HX at a certain Ra, but it can tell which HX can benefit more from the convection based on the aspect ratio of the HX.

As discussed above, if setting a further criterion for acceleration of the melting, such as $a_c = 10\%$, the threshold Rayleigh number Ra_{dc} can be obtained for each aspect ratio. And for this parametric study, the values of Ra_{dc} are tabulated in Table 6.1. The values of Ra_{dc} can be different by setting different criterions of η and a_c. The criteria adopted in this dissertation are $\eta = 0.8$ and $a_c = 10\%$, which can be considered as a kind of general settings based on the practical performance of the PCM HX.

Aspect ratio (A)	**Deciding Rayleigh number** (Ra_{dc})
1.0	2962
0.75	4029
0.50	6619
0.25	8480
0.05	58067

Table 6.1: Threshold Rayleigh Numbers (Ra_{dc}) Based on $\eta = 0.8$ and $a_c = 10\%$ for Aspect Ratios $A = 1.0$, 0.75, 0.5, 0.25 and 0.05.

From Table 6.1, a big jump in Ra_{dc} can be observed, from 8480 at $A = 0.25$ to 58067 at $A = 0.05$, while the variation of Ra_{dc} from $A = 1.0$ to $A = 0.25$ is

almost linear. To interpret this behavior, the cases for both $A = 0.25$ and $A = 0.05$ are discussed in detail. Attention is focused on the case $A = 0.25$. Fig. 6.9 and Fig. 6.10 show the overall liquid fraction and the average temperature of the PCM respectively for $A = 0.25$, which can be used to demonstrate the uneven temperature distribution caused by convection.

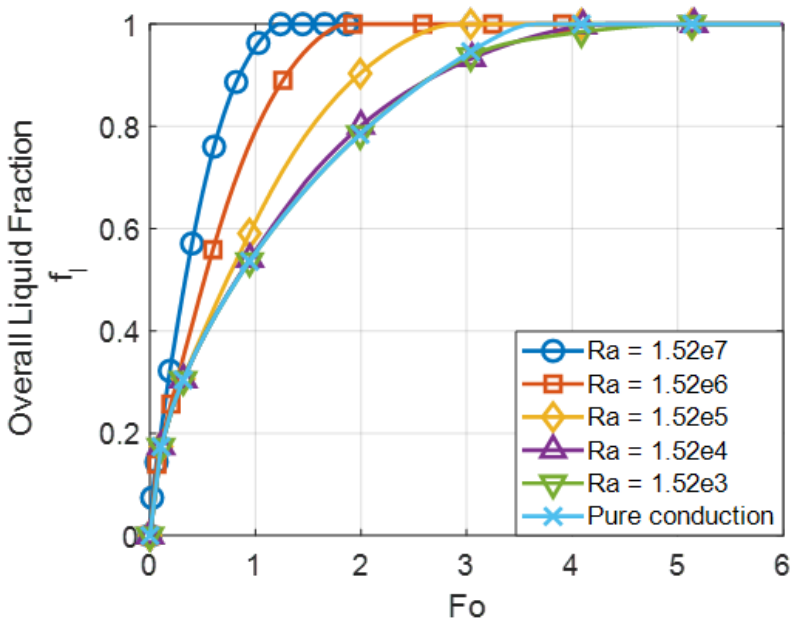

Figure 6.9: Overall liquid fraction f_l versus Fourier number (Fo) with aspect ratio $A = 0.25$.

It can be observed from Fig. 6.9 that the liquid fraction for both $Ra = 1.52 \times 10^4$ and $Ra = 1.52 \times 10^3$ is lower than that for pure conduction between $Fo = 3$ and $Fo = 4$, which indicates that there should be residual solid PCM for these two cases, which are relatively difficult to melt uniformly because of uneven convection. Moreover, the average temperature for these two cases are almost above the conduction curve according to Fig. 6.10. Lower liquid fraction with higher average temperature further reveals the uneven temperature distributions caused by

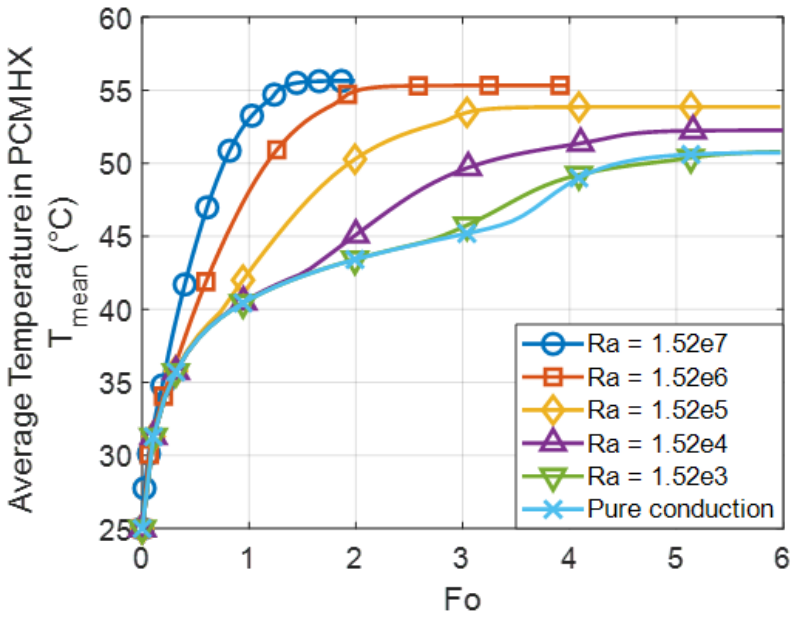

Figure 6.10: Average temperature T_{mean} in PCM HX versus Fourier number (Fo) with aspect ratio $A = 0.25$.

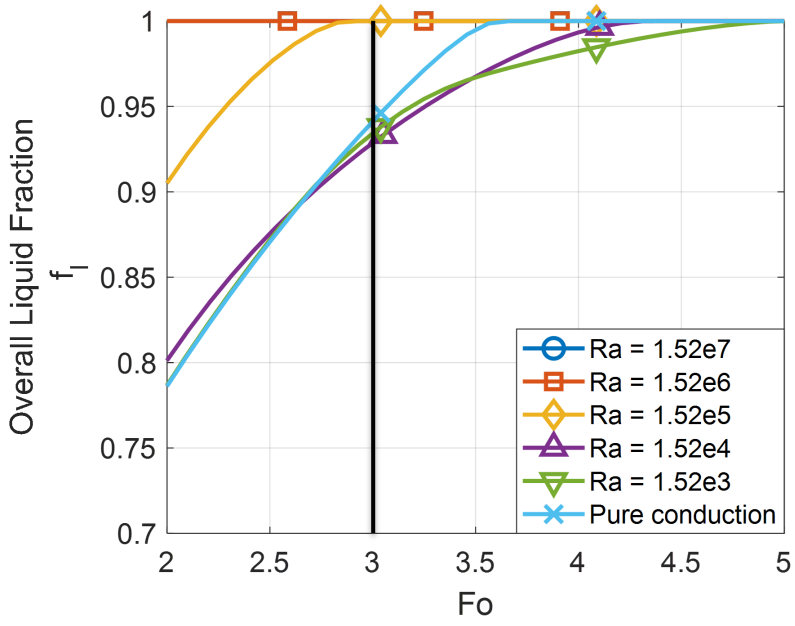

Figure 6.11: Overall liquid fraction f_l versus Fourier number (Fo) with aspect ratio $A = 0.25$ (zoomed).

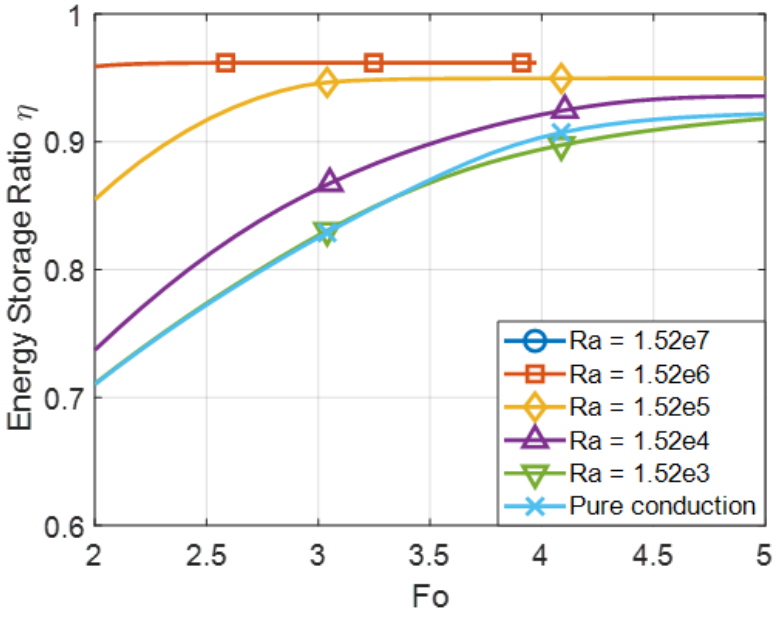

Figure 6.12: Energy storage ratio (η) versus Fourier number (Fo) at various Rayleigh numbers (Ra) for aspect ratio $A = 0.25$ (zoomed).

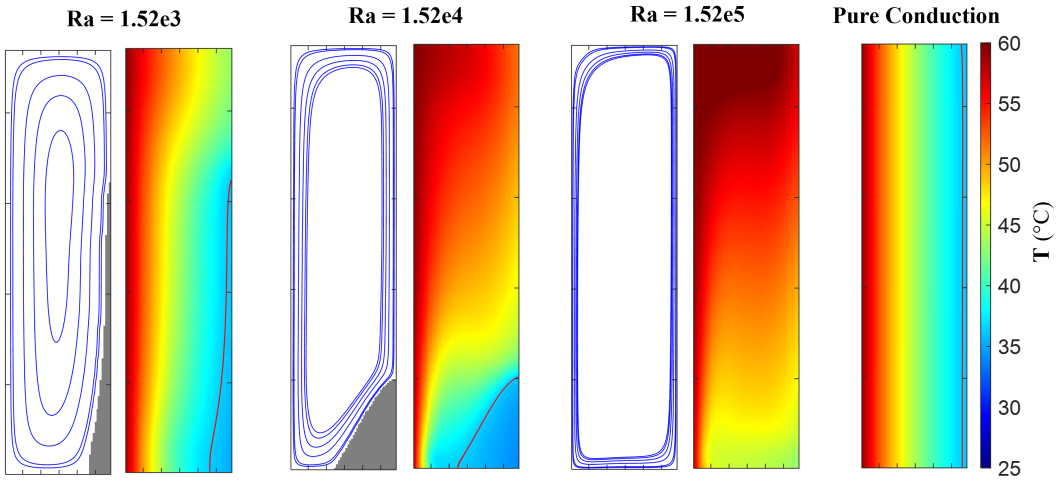

Figure 6.13: Streamlines and temperature field of the PCM HX with aspect ratio ($A = 0.25$) at $Fo = 3$ for $Ra = 1.52\times10^3, 1.52\times10^4, 1.52\times10^5$ and pure conduction.

the convection heat transfer. The differences among those curves can be seen more clearly by zooming into Fig. 6.9, which is shown in Fig. 6.11. Another zoomed in

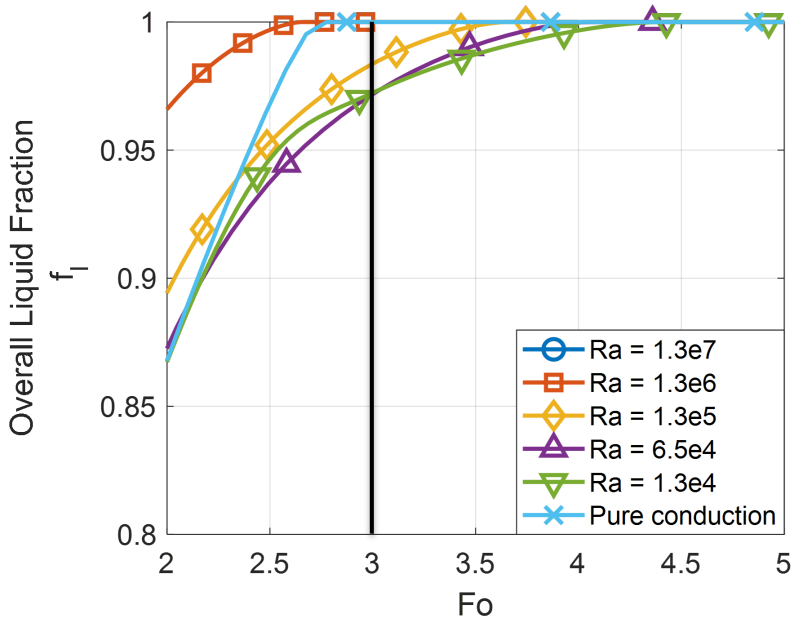

Figure 6.14: Overall liquid fraction f_l versus Fourier number (Fo) with aspect ratio $A = 0.05$ (zoomed).

view is also provided for the energy storage ratio in Fig. 6.12. According to Fig. 6.11 and Fig. 6.12, the uneven temperature distribution resulting in a higher average temperature of the PCM reduces the heat transfer from the HTF to the PCM, which can be observed by the energy storage curve at $Ra = 1.52 \times 10^3$, where the thermal performance is even worse than pure conduction. For the case of $Ra = 1.52 \times 10^4$, enhancement of heat transfer by convection can already compensate for the decrease in performance due to the uneven distribution, therefore making it more efficient than pure conduction.

Fig. 6.13 further supports this interpretation by comparing the streamlines and isotherms between the convection cases and the pure conduction at $Fo = 3$, as denoted by the vertical bar in Fig. 6.11. Compared with the temperature field for pure conduction, in the convection cases with low Ra, such as that of $Ra = 1.52 \times 10^3$,

convection only alters the melting front and is not strong enough to enhance heat transfer. However, such a deformation of the melting front results in an uneven temperature distribution, which keeps producing liquid PCM on the top part which become superheated and thus harms the thermal performance of the HX. As Ra becomes larger, the convection effect starts to govern the heat transfer, as shown by the cases of $Ra = 1.52 \times 10^4$ and $Ra = 1.52 \times 10^5$ in the Fig. 6.13, where the convection effect is strong enough as it leads the melting front along the axial direction towards the bottom. In such a situation, the enhancement of heat transfer from convection can offset and even exceed the weakening of thermal performance caused by uneven temperature distributions.

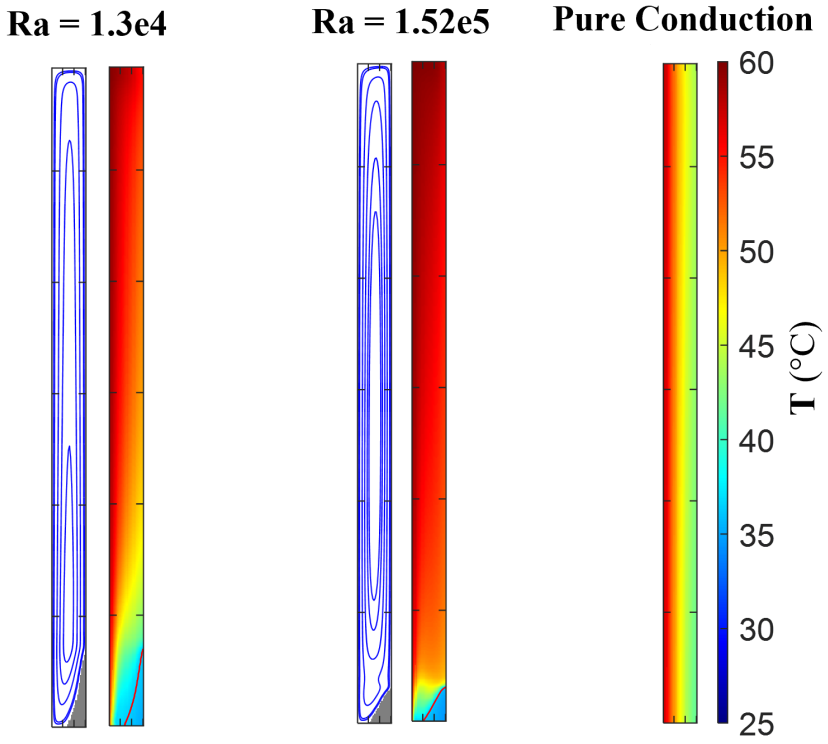

Figure 6.15: Streamlines and temperature field of the PCM HX with aspect ratio ($A = 0.05$) at $Fo = 3$ for $Ra = 1.3 \times 10^4, 1.3 \times 10^5$ and pure conduction.

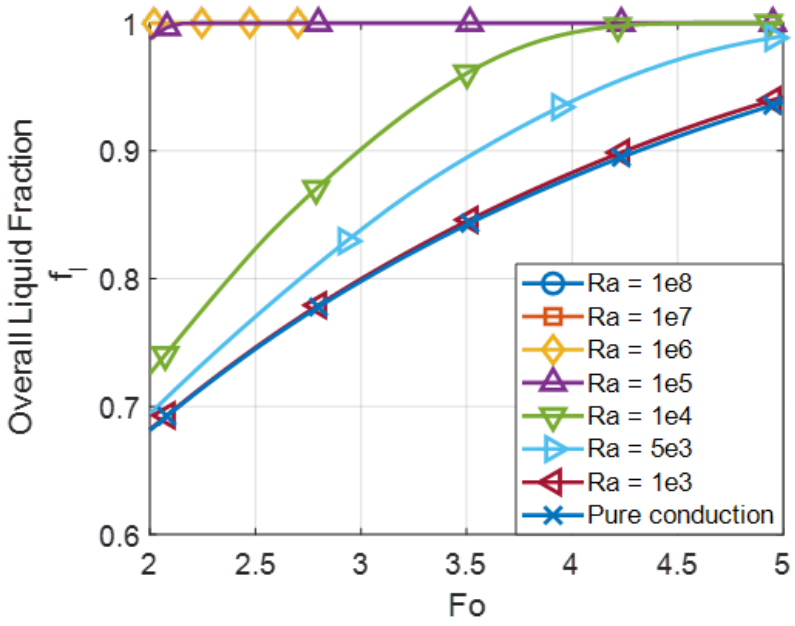

Figure 6.16: Overall liquid fraction f_l versus Fourier number (Fo) with aspect ratio $A = 1.0$ (zoomed).

As for the HX with an aspect ratio of 0.05, it is more difficult to overcome the adverse effect of uneven convection even for larger values of the Rayleigh number. A much higher level of convection is needed to compensate for the uneven distribution, as shown in Fig. 6.14. The streamlines and temperature field of the PCM HX at $Fo = 3$ are displayed in Fig. 6.15, where the difference of the temperature fields can be observed between a low Ra ($Ra = 1.3 \times 10^4$) which can barely offset the weakening of heat transfer at the bottom, and a moderate Ra ($Ra = 1.52 \times 10^5$) which is strong enough to further enhance the heat transfer.

The compensation for the weakening of the heat transfer caused by the uneven temperature distributions can explain the big jump of the threshold Ra_{dc} from $A = 0.25$ to $A = 0.05$. As the aspect ratio becomes smaller, the shape of the cylindrical HX becomes taller and thinner, which makes the conduction more significant under

the assumption of the fixed inlet temperature of the HTF and the constant total volume of the HX. And thus, higher Ra is needed to achieve the same acceleration effect of the melting compared with the larger aspect ratio. And for a larger aspect ratio, the weakening effect from the uneven distribution is almost negligible, according to Fig. 6.16. For the general PCM design, the Rayleigh numbers calculated based on the PCM types and working conditions should avoid the range where the thermal performance of the HX is degraded due to low Ra. The threshold Ra_{dc} in Table 6.1 based on the aspect ratios and the melting acceleration chart in Fig. 6.8 can then be utilized as references to determine the geometries and suitable PCM for a cylindrical HX under given working conditions.

6.2 Effect of the Porous Media on Convective Melting in Cylindrical HX

Based on the parametric study in Section 6.1, a simulation is conducted for the PCM melting with the porous media in the cylindrical HX, The HX with aspect ratio at 0.5 is chosen, the Ra is set to 10^8 and the rest of the settings are the same as the parametric study in Section 6.1. The porosity of the porous media is set to 0.9, and thus its corresponding effective thermal conductivity is calculated as 14.6 $W/(m\ K)$ based on Eq. (2.19), by setting $k_{p,m} = 170\ W/(m\ K)$.

The simulation results, shown in Fig. 6.17 and Fig. 6.18, are compared with the pure PCM melting of the HX at the same aspect ratio and Rayleigh number. From Fig. 6.17, adding porous media accelerates PCM melting as it enhances the thermal

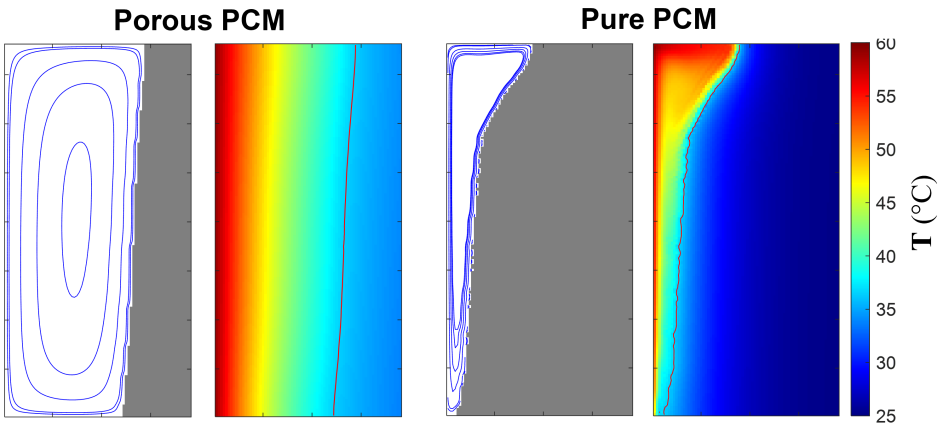

Figure 6.17: Streamlines and temperature field of the PCM HX with aspect ratio ($A = 0.5$) at $Fo = 0.027$ for $Ra = 1 \times 10^8$.

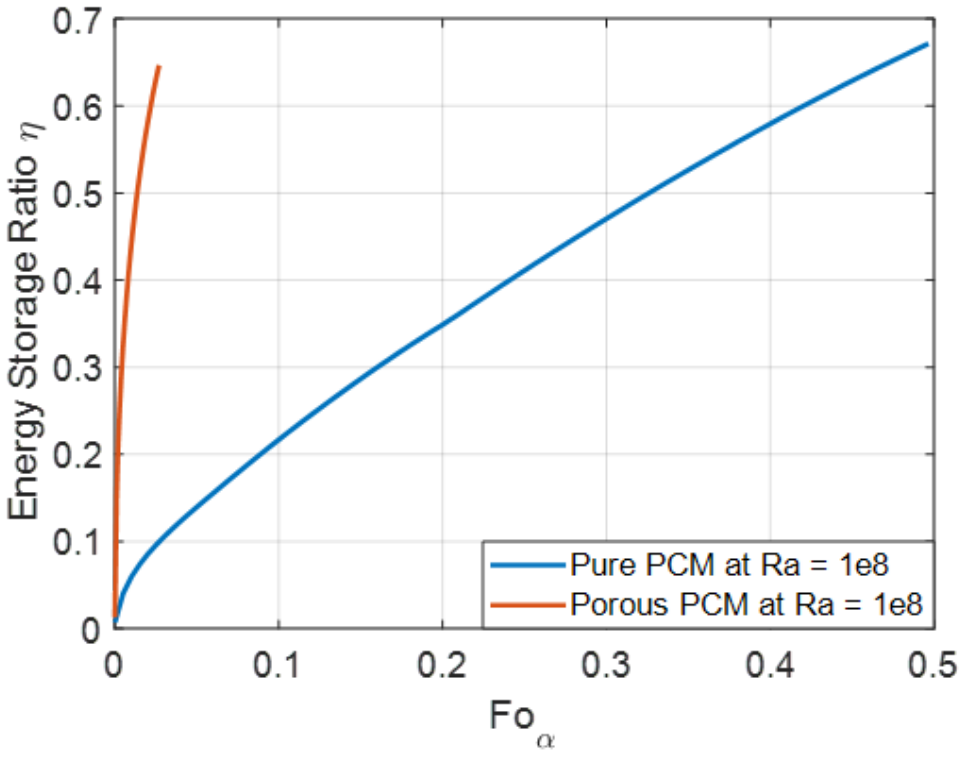

Figure 6.18: Comparison of energy storage ratios (η) versus Fourier number (Fo) at $Ra = 1 \times 10^8$, $A = 0.5$.

conductivity across the entire domain. According to Fig. 6.17, the acceleration of the porous melting at $\phi = 0.9$ could be up to 95 % for reaching the 60 % of total

energy storage.

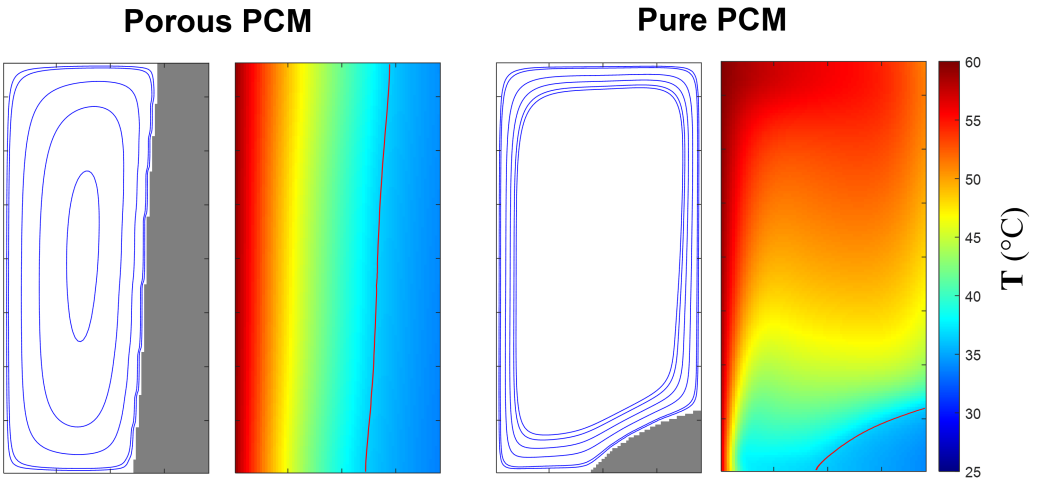

Figure 6.19: Streamlines and temperature field of the PCM HX with aspect ratio ($A = 0.5$) at $Fo = 2.0$ for $Ra = 1.37 \times 10^6$.

If calculating the Ra based on the effective thermal conductivity k_e instead of the thermal conductivity of the liquid PCM, the actual Ra for the porous PCM would be less, which is approximately 1.37×10^6 in this case study. Moreover, the Prandtl number should also change accordingly, which is about 1.2 based on the effective thermal diffusivity α_e in this case. Moreover, the drag force due to the presence of the porous media undermines the convection flow in the liquid zone, which further attenuates the impact of convection. From the streamlines in Fig. 6.17, it can be observed that the flow is more uniform and less uneven for the porous PCM. To further identify the flow regulation due to the presence of the porous media, a comparison with the pure PCM at $Ra = 1.37 \times 10^6$ is performed, and the results are shown in Fig. 6.19. The purpose of this comparison is that the porous media is modeled at the REV scale, where α_e is directly utilized in solving the energy equations. Therefore, the simulation of the porous PCM melting would be

equivalent to that of the pure PCM at $Ra = 1.37 \times 10^6$ if the drag force caused by the porous media is set equal to zero. By comparing the two, the effect of the porous media on the fluid flow becomes apparent, and the effect on the temperature field due to the specific characteristics of the flow field is also revealed.

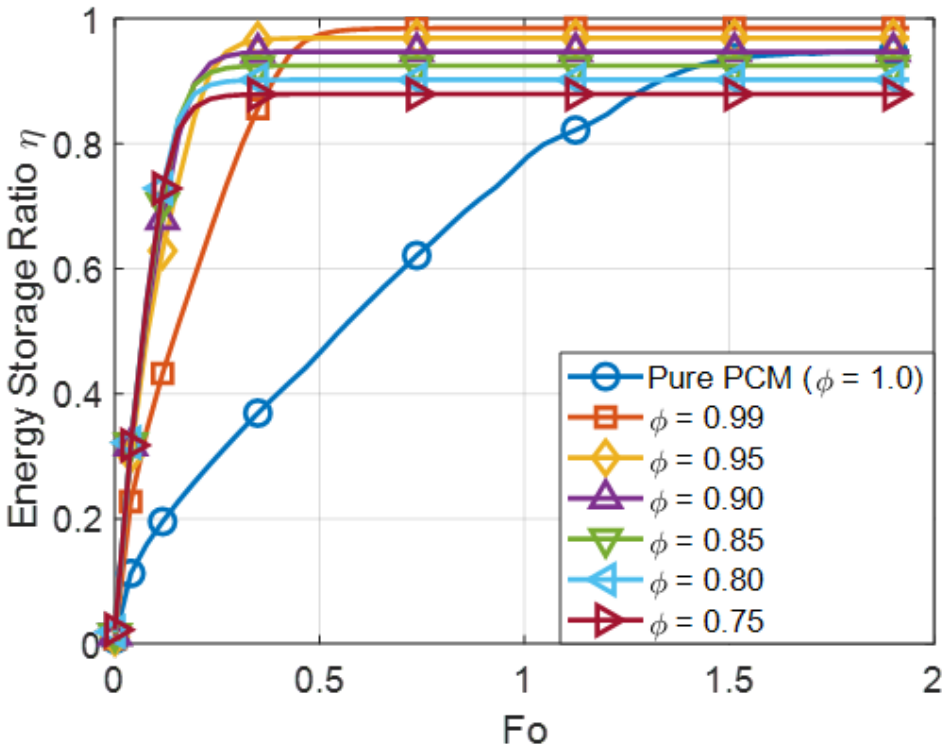

Figure 6.20: Comparison of energy storage ratios (η) versus Fourier number (Fo) for porous PCM HX with various porosities at $Ra = 1.25 \times 10^6$, $A = 0.5$.

To further investigate the effect of porous media on PCM melting, the simulations of cylindrical PCM HX with aspect ratio at 0.5 and Rayleigh number at 1.25×10^6 under various porosities are conducted, with other settings the same as those in Section 6.1. The results shown in Fig. 6.20 demonstrate the energy storage ratios of PCM HX along Fourier number for porous PCM with various porosities ($0.75 \leq \phi \leq 0.99$) compared with pure PCM ($\phi = 1.0$). As the porosity decreases,

the effective thermal conductivity increases due to the addition of porous media, which results in the acceleration of PCM melting. Meanwhile, the theoretical maximum energy storage ratio decreases as the porosity decreases because the PCM is taken up by the porous media. From Section 6.1, the melting acceleration rate a_c is calculated at each porosity by setting 80 % energy storage rate as the criterion. Table 6.2 summarizes the effective thermal conductivity (k_e), theoretical maximum energy storage ratio (η_{max}) and melting acceleration rate (a_c) for each porosity.

Porosity	1.0	0.99	0.95	0.90	0.85	0.80	0.75
k_e (W/(m K))	0.2	1.64	7.4	13	20	30	39
η_{max}	1.0	0.99	0.97	0.95	0.92	0.89	0.87
a_c	0	68%	82 %	86 %	86 %	86 %	86%

Table 6.2: Effective Thermal Conductivity k_e, Theoretical Maximum Energy Storage Ratio η_{max} and Melting Acceleration Rate a_c for Porous PCM Melting at Various Porosities.

From Table 6.2, the melting acceleration rate increases dramatically at high porosity ($\phi \geq 0.95$). The acceleration effect reaches its maximum at 86 % around $\phi = 0.90$ and it remains at 86 % if the porosity further decreases ($\phi \leq 0.90$). This stagnation of acceleration rate below a certain porosity is because of the negative effect of porous media on convective flow and maximum energy storage, which limits the heat transfer performance of PCM HX. The results from Table 6.2 indicate that there exists an optimal porosity where the maximum acceleration rate can be achieved at the cost of the least reduction in maximum energy storage. In this study, the porous media with high porosity ($\phi \geq 0.9$) is recommended for PCM HX to gain a high acceleration rate of melting and meanwhile maintain a small reduction in maximum energy storage.

6.3 Evaluation of the Modified Cylindrical HX for Enhancing PCM Melting

According to the parametric study in Section 6.1, there always exists a residual solid PCM that is hard to melt near the bottom left corner due to convection, which leads to uneven temperature distribution, and consequently, causes thermal performance to deteriorate. Many techniques have been developed to address this issue and improve the thermal efficiency of PCM HX. Among them, one of the methods is to modify the shape of the HX based on the concept that removing part of the PCM from the locations with poor heat transfer conditions to other locations where convective heat transfer is more effective in melting the PCM. In this section, simulations are conducted for a modified cylindrical HX as shown in Fig. 6.21.

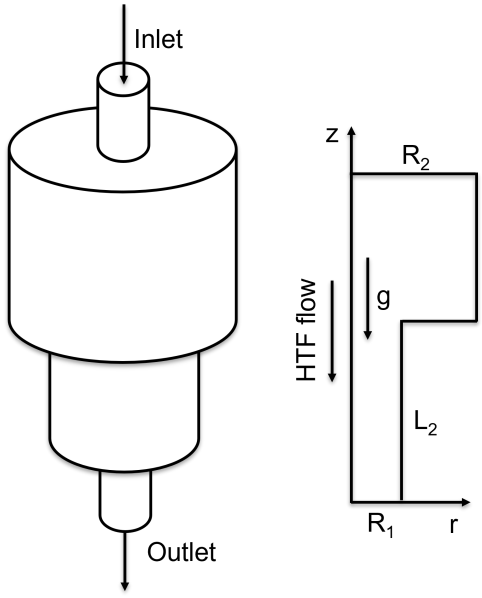

Figure 6.21: 3D modified cylindrical HX sketch (left) and its 2D half center-sliced sketch (right).

The modified cylinder is based on the normal cylinder with an aspect ratio of 0.5 by keeping the same total volume of the HX. The detailed geometric settings in LBM are listed in Table 6.3, where R_1 and R_2 are the radius gap. All the values are in LBM units, where the units are lu (length unit in LBM). Other settings are consistent with the parametric studies in Section 6.1.

Geometry	R_1	R_2	L_1	L
Straight cylinder	76	76	-	152
Modified geometry one	23	100	76	152
Modified geometry two	46	90	76	152

Table 6.3: Geometric Settings for the Modified Cylindrical HX.

The temperature fields are plotted in Fig. 6.22 at various Fourier numbers for modified geometry one ($R_1 = 23, R_2 = 100$) in (a), modified geometry two ($R_1 = 46, R_2 = 90$) in (b) and straight cylinder ($R = 76$) in (c). It can be observed that at each Fo, the melting of PCM is more rapid for the modified geometry compared with the basic straight cylinder. The acceleration rate for the modified geometry is dependent on the radius gap (R_1 and R_2). Generally, the acceleration of melting increases as the bottom radius gap R_1 narrows down and the top radius gap R_2 becomes larger, as shown by the comparison between (a) and (b) in Fig. 6.22. This indicates that shrinking R_1 and meanwhile enlarging R_2 under the same total volume, which results in the HX shape with a narrow bottom half and a wider top half, can enhance thermal performance by taking the advantages of convection heat transfer.

A more detailed comparison between the modified geometry and the basic

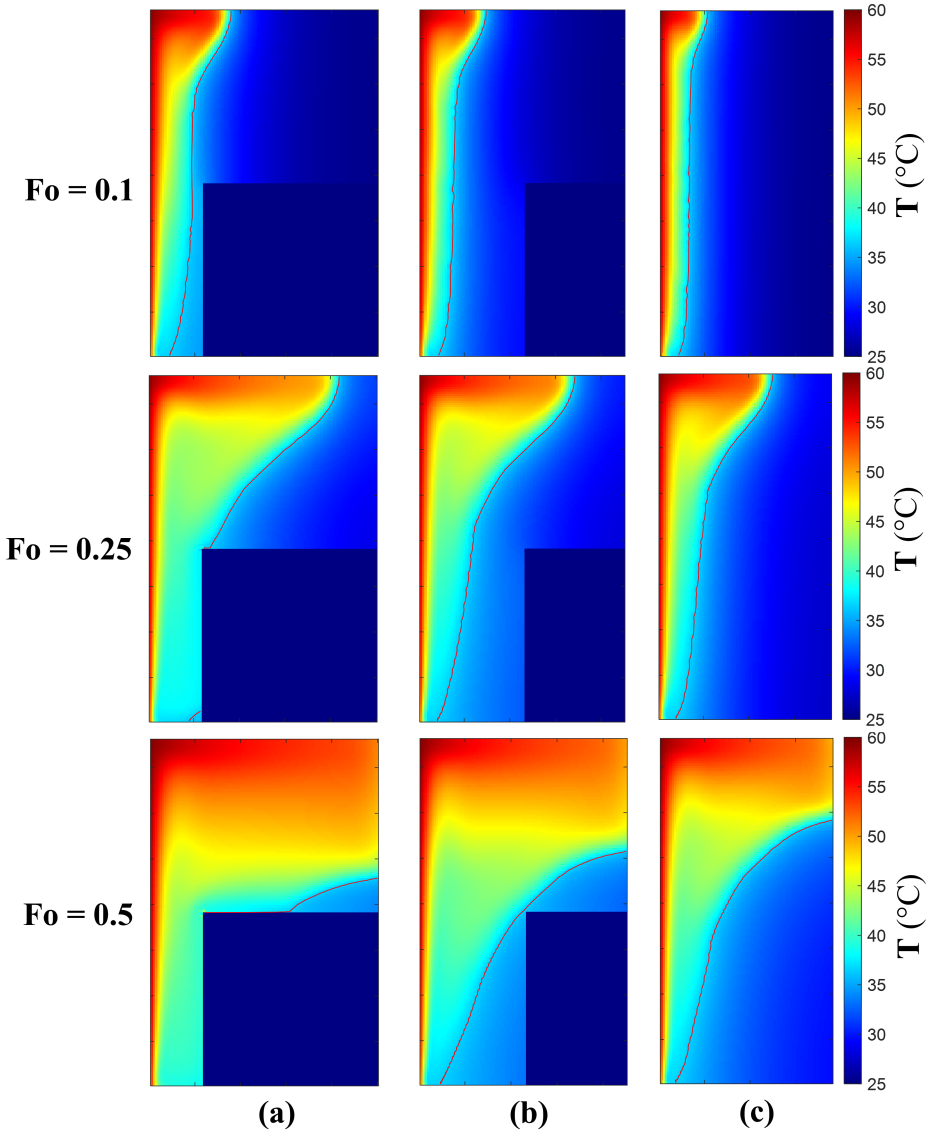

Figure 6.22: Streamlines and temperature field of the PCM HX with $A = 0.5$ and $Ra = 1.25 \times 10^6$ at $Fo = 0.1$, 0.25 and 0.5: (a) modified geometry one, (b) modified geometry two and (c) basic straight cylinder.

straight cylinder are demonstrated in Fig. 6.23, Fig. 6.24 and Fig. 6.25 in terms of the variations of the energy storage ratio (η), the overall liquid fraction (f_l) and the average temperature (T_{mean}) in the PCM HX. From Fig. 6.23, the acceleration rates of melting (a_c) at $\eta = 0.8$ could reach 45% for the modified geometry ($R_1 = 46, R_2 = 90$) and 57% for the modified geometry ($R_1 = 23, R_2 = 100$) compared with the

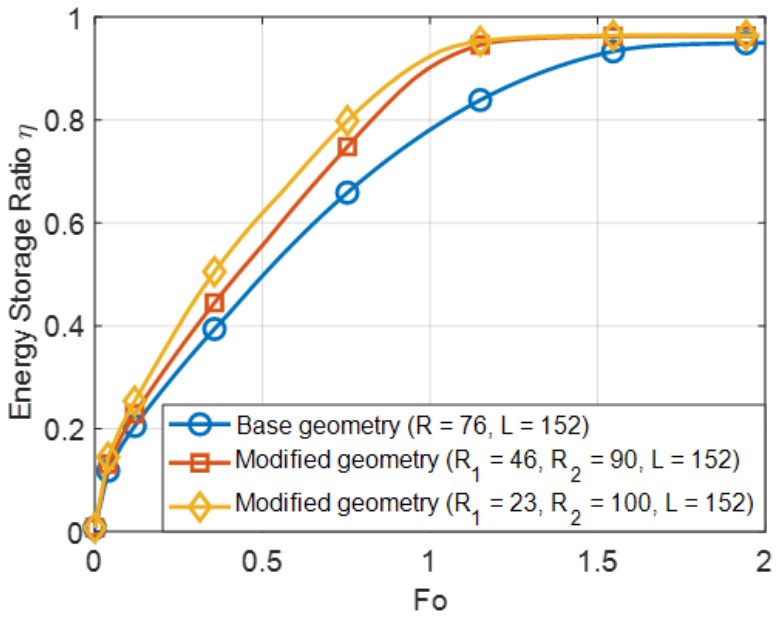

Figure 6.23: Comparison of energy storage ratios (η) versus Fourier number (Fo) at $Ra = 1.25 \times 10^6$, $A = 0.5$.

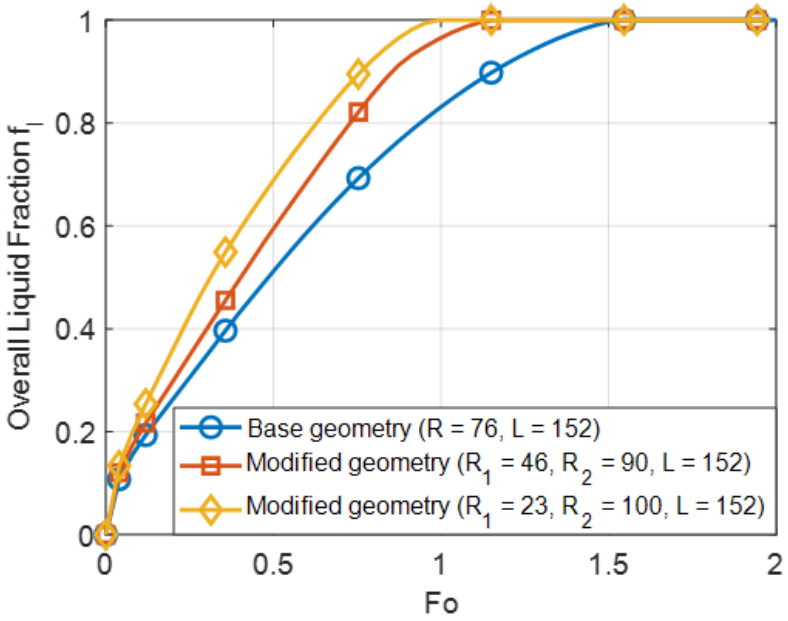

Figure 6.24: Comparison of overall liquid fraction f_l versus Fourier number (Fo) at $Ra = 1.25 \times 10^6$, $A = 0.5$.

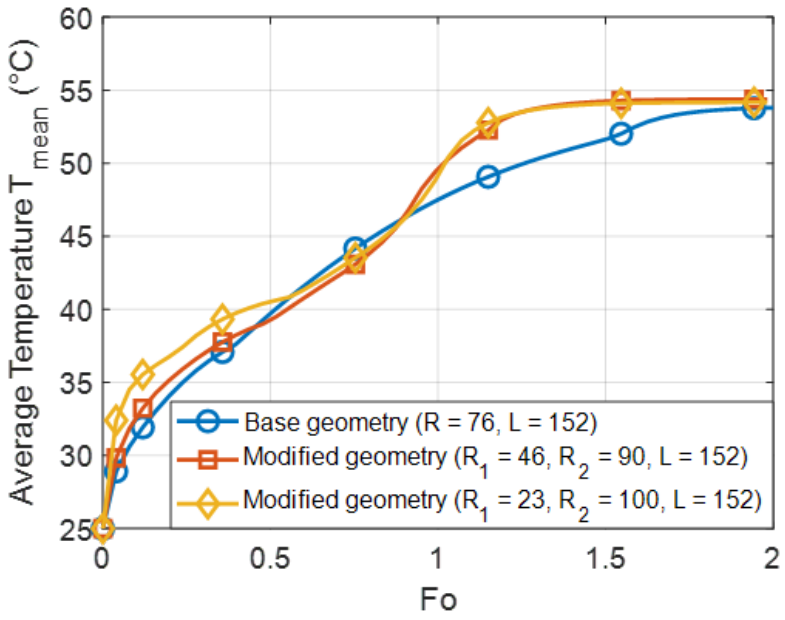

Figure 6.25: Comparison of average temperature T_{mean} versus Fourier number (Fo) at $Ra = 1.25 \times 10^6$, $A = 0.5$.

straight cylinder at $R = 76$. Moreover, complete melting of PCM ($f_l = 1.0$) occurs earlier for the modified geometry. According to Fig. 6.24, the time for complete melting of PCM is shortened by 25% for the geometry ($R_1 = 46, R_2 = 90$) and 33% for the geometry ($R_1 = 23, R_2 = 100$) compared with the basic straight cylinder.

Generally, for the energy storage and liquid fraction shown in Fig. 6.23 and Fig. 6.24, the average temperature for the modified geometry should also exceed that for the basic straight cylinder since the PCM takes more energy from the HTF flow. However, as Fig. 6.24 indicates, the average temperature of the PCM for the modified geometries can be lower than that in the basic cylinder between $Fo = 0.5$ and $Fo = 1$, which can also be explained by the uneven temperature distributions. By adopting the modified geometry, the entire PCM can melt within a relatively short time range, leading to a more uniform temperature field. Because of the latent

heat property of the PCM, the PCM can stay around the melting temperature when the liquid fraction is less than one. But for the liquid PCM, its temperature could rise quickly upon absorbing heat. Therefore, PCM melting with more even temperature distributions can prevent the occurrence of the extremely hot liquid PCM on the top, and thus the average temperature of PCM tends to be lower than the uneven case. The lower average temperature of the PCM, in general, leads to a larger temperature difference between the HTF flow and the PCM. Consequently, heat transfer can be further improved by this larger temperature difference, which benefits thermal performance of HX.

6.4 Chapter Summary

To conclude, the parametric study in Section 6.1 evaluates performance of the PCM HX with various aspect ratios and Rayleigh numbers. The variation of the aspect ratios and Rayleigh numbers represents the different shapes of the cylindrical HX and the changes in the intensity of convective heat transfer. The results from this parametric study provide quantified melting acceleration rates of the PCM HX with various aspect ratios and Rayleigh numbers. The threshold Rayleigh number (Ra_{dc}) is proposed to serve as a reference for the design of the cylindrical HX. Following that, the parametric study in Section 6.2 further investigates in detail one case of PCM melting with porous media. The results demonstrate the positive effect of adding porous media on heat transfer over the entire PCM domain, and the negative effect of porous media on convective flow in the liquid zone. Finally, the

parametric study performed in Section 6.3 evaluates the heat transfer enhancement by modifying the geometry of cylindrical HX. The concept is to fully take advantage of convective heat transfer by modifying the geometry to offset the negative effect of uneven temperature distributions caused by convection. The results indicate a significant improvement in thermal performance of the PCM HX by using the modified geometry.

Chapter 7: Conclusions and Future Work

7.1 Conclusions

Owing to the feature of the lattice Boltzmann method in parallel computing, lattice Boltzmann models using parallel schemes can perform numerical analysis more efficiently compared with conventional NS-based models. This dissertation focuses on the development and application of the lattice Boltzmann model for PCM HX. In terms of the development of the lattice Boltzmann model, the basic macroscopic governing equations are introduced in Chapter 2, where the modifications of the governing equations for the porous media, DSC correlated enthalpy equations, and conjugate heat transfer with conducting fins are proposed. The single-phase lattice Boltzmann models based on the macroscopic governing equations are demonstrated in Chapter 3, in which the single-phase LBM for fluid flow can be directly utilized to simulate the flow field in the liquid PCM zone. The thermal LBM is further developed based on the single-phase model to solve the temperature field of the solid-liquid phase change, as discussed in Chapter 4. The major conclusions for the development of the lattice Boltzmann model for the PCM HX are highlighted as follows:

1. The DSC correlated enthalpy equations were applied in the enthalpy-based LBM for a more accurate enthalpy modeling of the PCM HX. (Section 2.5)

2. The modified macroscopic governing equations based on enthalpy were proposed both in Cartesian and axisymmetric coordinates for the development of the enthalpy-based LBM with DSC correlated enthalpy equations. (Section 2.6)

3. A comprehensive lattice Boltzmann model based on the MRT scheme was proposed and developed for simulating the flow and temperature fields in PCM HX, which is capable of simulating the porous PCM under strong natural convection effect both in Cartesian and axisymmetric coordinates. The new model can be deconstructed as a single-phase MRT-LBM for the flow field in the liquid zone, a DSC correlated enthalpy-based thermal MRT-LBM for the temperature field across the entire PCM domain, and a scheme to automatically track the interface between the liquid and solid PCM based on the liquid fraction. (Section 4.1, Section 4.2, Section 4.3 and Section 4.4)

4. The conjugate heat transfer scheme was proposed and developed to model the HTF flow and the finned HX, where the HTF flow was solved by the developed 1D model, and the calculated temperatures on the surface between the HTF and PCM were applied to the boundary conditions in LBM, and the temperature field within the conducting fins are modeled separately based on a different enthalpy equation, with a boundary treatment for the surface between the conducting fins and the PCM. (Section 2.4, Section 4.4 and Section 4.5)

5. The parallel LBM scheme was proposed and developed for the enthalpy-based DDF-MRT lattice Boltzmann model. The decomposition of the entire domain can be either 1D or 2D. And the exchange of information between each related partial unit was achieved by the code developed based on Microsoft MPI (MSMPI) for Windows environment and OpenMPI for Linux environment. (Section 4.6)

In terms of the numerical simulation, several case studies are conducted to verify and validate the new model, as demonstrated in Section 5.1 and Section 5.2. Besides, scaling analyses of the parallel LBM scheme are performed by using the high performance computing (HPC) resources from University of Maryland, as demonstrated in Section 5.3. Parametric studies of the cylindrical PCM HX are then conducted based on the validated lattice Boltzmann model, as introduced in Chapter 6. The main conclusions for the numerical simulation based on the developed model are summarized as follows:

1. The enthalpy-based DDF-MRT LBM in Cartesian coordinates was verified by the porous PCM melting in a rectangle cavity. The simulation results were in good agreement and indicate that the basic Cartesian model is capable of solving the convective PCM melting with the porous media. (Section 5.1.2)

2. The enthalpy-based DDF-MRT LBM in axisymmetric coordinates was validated by PCM melting in cylindrical HX. The validation of pure PCM melting with the experimental data from CEEE indicated that the developed model successfully predicted the temperature variations in the PCM HX with the

errors confined within 10 % for the local temperatures and 5 % for average PCM temperature. The validation of porous PCM melting in cylindrical HX also indicated that the error of the temperature predictions was under 10 % for the developed model. (Section 5.2.2, Section 5.2.3 and Section 5.2.4)

3. A comprehensive parametric study was conducted for the cylindrical PCM HX with various aspect ratios and Rayleigh numbers. Based on the criterion ($\eta = 0.8$) proposed in this case, the accelerations of the PCM melting (a_c) at different Rayleigh numbers were quantified, and the threshold Rayleigh numbers Ra_{dc} at various aspect ratios were proposed to serve as references for the design of the cylindrical HX. It was observed that Ra_{dc} increases as the aspect ratio becomes smaller, which indicated that higher Rayleigh numbers are required for the PCM HX with smaller aspect ratios to reach the same acceleration rate of the melting. (Section 6.1)

4. A case study of the porous PCM melting was performed and compared with the pure PCM melting, which indicated that the acceleration of the melting could be up to 86 % for energy storage at $\eta = 0.8$ by adding the porous media. The porous media with high porosity $\phi \geq 0.9$ is recommended for PCM HX to obtain a high acceleration rate of melting at the cost of a reasonable reduction in maximum energy storage. (Section 6.2)

5. A parametric study was performed to evaluate the modified cylindrical HX designed based on the concept of taking the advantages of convection effect to offset the negative effect of the uneven temperature distributions caused by

convection heat transfer. The modified geometry in two variants were simulated, and the results indicated that the melting accelerations could reach 45 % and 57 % respectively compared with the straight cylinder under the same total volume. The acceleration rates were higher for the modified PCM HX with a more narrow bottom and wider top. Moreover, adopting the modified geometry could balance the uneven temperature distributions due to convection, which further benefits thermal performance of HX. (Section 6.3)

7.2 Future Work

7.2.1 Extensions and Improvements of the Developed 2D Enthalpy-Based DDF-MRT LBM

Following the validation of PCM melting with conducting fins introduced in Section 5.2.4, more validations should be conducted to further proves the capability of the model. Besides, the parametric studies of the finned HX, especially in combination with the porous media, are interesting topics that require further investigations.

Following the case study of porous PCM melting in Section 6.2, the melting with more settings of the porous media is expected to be performed by varying the porosity and permeability of the porous media. The complete study of this porous PCM melting can provide detailed data on HX performance with different porous media settings, which can serve as the reference for the design of the enhanced PCM HX.

Following the evaluation of PCM melting in modified cylindrical HX as discussed in Section 6.3, more solidification cases are expected to be conducted. In general, a PCM HX is evaluated by its performance of melting and solidification. Given the fact that convection heat transfer is more influential in PCM melting, and its effect becomes limited in the solidification case, conduction always dominates the heat transfer in PCM solidification. And therefore the modified HX, such as the one in Section 6.3, can have poor performance in the solidification process compared with the straight cylinder since the top part of modified geometry is wider which requires more time to solidify the PCM on the top. For the cases where the solidification process of the HX is performed at non-occupied hours, and melting performance is much more important, the modified geometry in Section 6.3 can be a good choice. However, solidification performance is still worth investigating in order to obtain a more comprehensive evaluation of the PCM HX. In general, the analysis of solidification process is expected to be conducted to complete the full evaluation of PCM HX.

7.2.2 3D Solid-Liquid Lattice Boltzmann Model

The new 2D model can only solve limited HX shapes, while more complicated geometries of the PCM HX, such as the shell and tube HX [92] and helical tube HX [93], require a 3D model. Therefore, the development of the 3D lattice Boltzmann model for solving the solid-liquid phase change can extend the application of LBM, and meanwhile benefit the design and analysis of the PCM HX.

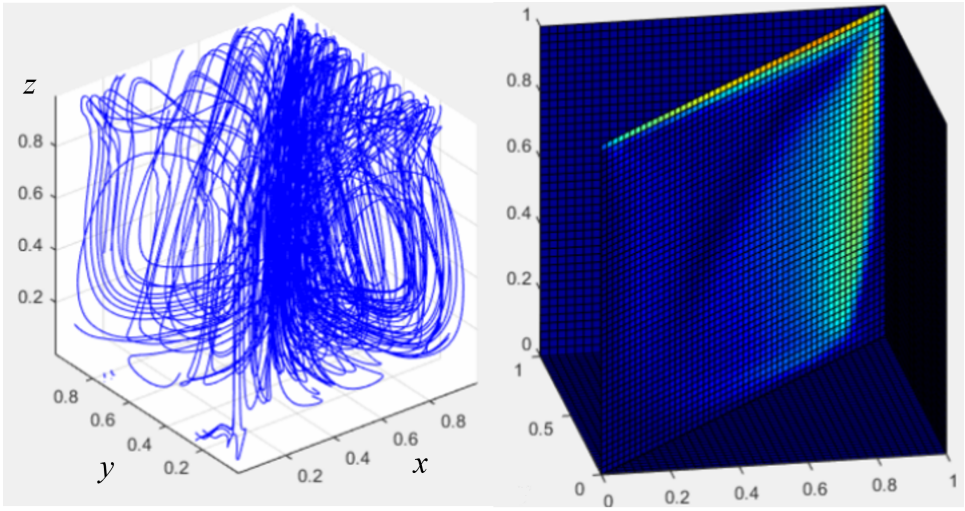

Figure 7.1: Streamlines (left) and velocity field (right) for a 3D lid-driven cavity with $(U, V) = (0.1, 0.1)$ at steady state.

The 3D LBM for isothermal fluid flow has been developed in Cartesian coordinates. A sample simulation is conducted for a 3D lid-driven cavity with its top lid moving along a diagonal direction at velocities $(U, V) = (0.1, 0.1)$. And Fig. 7.1 shows the streamlines and velocity contours near steady state.

Following that, the models introduced in Section 3.3 can be utilized to further develop the 3D enthalpy-based DDF-MRT LBM for the PCM HX, which could solve PCM phase change problems in more complicated geometries.

7.2.3 Development of Liquid-Gas Lattice Boltzmann Model

The motivation for developing a specific liquid-gas lattice Boltzmann model is to study the adiabatic two-phase flow in the microchannel header, analyze the maldistribution due to the two-phase flow and evaluate its effect on the performance of the microchannel HX (MCHX). MCHXs are widely used in HVAC&R because

of their ability to enhance heat transfer performance. The microchannel headers in MCHXs serve as the components to collect and distribute the working fluid to individual microchannels. However, the headers suffer from the maldistribution of the working fluid, which results in poor performance of MCHXs. The main causes of the flow maldistribution can be summarized as the geometry of the headers, the uneven heat transfer process, and liquid-gas flow in the headers [94]. To study this issue numerically, many models have been developed for the single-phase flow in the headers based on the conventional NS-based CFD methods [95–97]. While the studies of the effect of the liquid-gas flow on the maldistribution in the headers are limited due to the difficulties in the modeling and tracking of the phase interfaces in the NS-based methods. Liquid-gas LBM, on the other hand, can solve the phase behavior efficiently. Therefore it is considered to be one of the promising approaches to studying the maldistribution of the liquid-gas flow in the headers.

Several multiphase lattice Boltzmann models have been developed over the past three decades. Gunstensen et. al [98] developed the RK LB model which used color gradients to separate and model the interaction at the multiphase interfaces. Shan and Chen [99] proposed the pseudopotential LB model where a pseudopotential function was introduced to account for the non-local particle interactions. Swift et. al [100] developed the free-energy LB model which directly introduces the phase effects into the collision process. He et. al [101] then proposed the phase-field LB model based on the phase-field theory with a derived force term to describe the multiphase behavior. Later, Li et. al [102] developed the entropy LB model which utilizes the MRT scheme instead of the single-relaxation-time scheme (SRT)

to increase the stability and support a wider range of the surface tension.

Among these multiphase LB models, the pseudopotential LB model and the phase-field LB model are commonly adopted to simulate liquid-gas flow because of their successful application of two-phase flow at large density ratios ($\rho_l/\rho_g \sim 10^3$) and relatively high Reynolds numbers [103,104]. For the cases in HVAC&R, e.g., the two-phase refrigerant flow in the microchannel header, the pseudopotential LBM can be selected as the basis to develop the liquid-gas LB model, owing to its simplicity in development over the phase-field LB model and its ability to integrate with the phase change scheme [105–108]. Currently, the developed model has the ability to simulate the liquid-gas phase interactions, e.g., the bubble oscillation. However, the model is still in its infancy as the MRT and the phase change scheme have not been applied. And the model needs to be further developed to simulate the liquid-gas flow with temperature variations.

The discrete Boltzmann equation of pseudopotential LB model is given by

$$\mathbf{f}(\mathbf{x}+\mathbf{e}\delta_t,t+\delta_t)-\mathbf{f}(\mathbf{x},t)=-\frac{1}{\tau_v}\left[\mathbf{f}(\mathbf{x},t)-\mathbf{f}^{eq}(\rho,\mathbf{u})\right]+\mathbf{F}_{sc}. \tag{7.1}$$

It is similar with Eq. (3.1) but with different equilibrium density distribution functions $\mathbf{f}^{eq}$ and forcing term $\mathbf{F}_{sc}$. The forcing term $\mathbf{F}_{sc}$ in the pseudopotential LB model is named as Shan-Chen forcing term [108], which is given as

$$\mathbf{F}_{sc}=-\frac{1}{\tau_v}\left[\mathbf{f}^{eq}(\rho,\mathbf{u}^{eq})-\mathbf{f}^{eq}(\rho,\mathbf{u})\right], \tag{7.2}$$

where $\mathbf{u}^{eq} = \mathbf{u} + \tau_v \delta_t \mathbf{F}/\rho$, and then the term $\mathbf{f}^{eq}(\rho, \mathbf{u}^{eq})$ can be expressed as

$$\mathbf{f}^{eq}(\rho, \mathbf{u}^{eq}) = \mathbf{f}^{eq}(\rho, \mathbf{u}) + \rho\omega_i \left[\frac{\mathbf{e}_i \cdot \tau_v \delta_t \mathbf{F}}{\rho c_s^2} + \frac{(\mathbf{e}_i \cdot \tau_v \delta_t \mathbf{F})^2}{2(\rho c_s)^4} - \frac{\mathbf{u} \cdot \tau_v \delta_t \mathbf{F}}{\rho c_s^2} \right], \tag{7.3}$$

where $\mathbf{f}^{eq}(\rho, \mathbf{u})$ can be calculated by Eq. (3.3) and $\mathbf{F}$ can be obtained by

$$\mathbf{F} = -G\psi(\mathbf{x}) \sum_i \omega_i \psi(\mathbf{x} + e_i \delta_t) e_i, \tag{7.4}$$

where G is the strength factor which controls the interaction force and the weight coefficients ω_i for D2Q9 are given as

$$\omega_i = \begin{cases} \frac{1}{3}, & |e_i|^2 = 1, \\ \\ \frac{1}{12}, & |e_i|^2 = 2, \end{cases} \tag{7.5}$$

and the pseudopotential function $\psi(\mathbf{x})$ can be determined by

$$\psi = \sqrt{\frac{2(P_{EOS} - \rho c_s^2)}{G c^2}}, \tag{7.6}$$

where P_{EOS} is the pressure of the fluid calculated from its equation of state.

Refrigerants	Density ratio	Surface tension (mN/m)
R134	90	11.7
R1234yf	67	9.5
R1233zd(E)	500	17.0

Table 7.1: Properties of the Three Refrigerants at 0 °C.

A sample case is conducted to simulate the bubble oscillation of three different

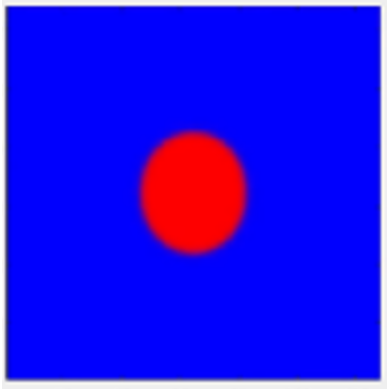

Figure 7.2: Initial gas bubble (red) in liquid region (blue).

Refrigerants	Calculation steps	Time (ms)
R134	14800	2.57
R1234yf	12600	2.19
R1233zd(E)	31700	5.51

Table 7.2: First Two Cycles of the Bubble Oscillations.

refrigerants: R134a, R1234yf, and R1233zd(E), as shown in Fig. 7.2. Table 7.1 lists the density ratios and the surface tensions of the three refrigerants at 0 °C [109,110], and the results are listed in Table 7.2. A clear trend can be observed from the results that higher surface tension leads to lower elasticity of the bubble and therefore results in higher time consumption to complete the first two cycles of the bubble oscillation. The simulation results indicate the developed basic pseudopotential LB model could simulate the phase interaction between liquid and gas. A more comprehensive liquid-gas LB model is expected to be established based on the current model by adding the following schemes: the MRT scheme, the DDF scheme for temperature variations, the phase change scheme, and the scheme for the treatment of the high-density ratios.

Chapter 8: Contributions

8.1 Summary of Contributions

Generally, this dissertation proposed and developed a comprehensive model for simulating the PCM HX based on the lattice Boltzmann method, by which the parametric studies of PCM HX were conducted to quantitatively evaluate the effect of natural convection, porous media, and HX geometries on PCM melting performance. The contributions from this dissertation aim to fill the research gaps summarized in Section 1.3. Correspondingly, the novelty and contributions of this dissertation can be divided into three categories: (A) Model development based on LBM, (B) Improvements of the developed model, and (C) Parametric studies and analyses of the PCM HX using the new model, which are discussed in detail as follows:

A. Model development based on LBM for solid-liquid phase change

A.1. Developed a comprehensive enthalpy-based lattice Boltzmann model for solid-liquid phase change (Chapter 2, Chapter 3 and Chapter 4)

The new DDF-LBM based on the enthalpy method, adopting the multi-relaxation-time (MRT) scheme, is capable of solving the thermal convec-

tive flow and phase change problems. By modeling the porous media at the REV scale, the new model can be used to simulate convective thermal flow and phase change with porous media. By modeling the HTF flow and conducting fins separately, the new model can be utilized to solve practical conjugate heat transfer problems, while the enthalpy-based lattice Boltzmann models that consider conjugate heat transfer are limited in the literature. By adapting the developed model to axisymmetric coordinates, the new model can be utilized to simulate the thermal flow and PCM phase change in axisymmetric geometries such as the cylinder and sphere efficiently.

Generally speaking, the new model in this dissertation is the first enthalpy-based LB model solving porous PCM phase change in axisymmetric coordinates, while there have been almost no axisymmetric LB models in the literature that simulate PCM phase change together with the porous media. For Cartesian coordinates, the new model embedding the HTF and fin schemes still excels the enthalpy-based LBM in the literature in terms of the conjugate heat transfer, which is supposed to be very common in PCM HX.

A.2. Developed a novel enthalpy-based thermal MRT-LBM for accurate enthalpy modeling (Section 2.5, Section 2.6 and Section 4.4.1)

The DSC correlated equations are commonly adopted in convectional CFD for modeling the enthalpy. However, the basic enthalpy-based LBM

in the literature models the enthalpy by step and linear functions, which can cause errors in the simulation results. Therefore, the DSC correlated enthalpy modeling was applied, and the new model was modified accordingly in this dissertation.

Generally, the new model in this dissertation is the first lattice Boltzmann model calculating the enthalpy based on DSC test data of the PCM, which improves the model accuracy of the LBM for the specific PCM. And owing to the adoption of the DSC correlation, the consideration of the variable specific heat capacity (c_p) is automatically achieved, while the most thermal LBM in the literature can not handle such a case.

B. Model improvements for better analyzing the PCM HX

B.1. Improved the LBM model for high Rayleigh number thermal flow ($Ra > 10^6$) (Section 4.4.2)

For the PCM melting, most of the studies focus on the cases where conduction and convection are balanced or conduction is dominated, especially when the porous media is considered. The corresponding Rayleigh numbers are usually below or around 10^6, and seldom exceed 10^8. However, for the actual PCM HX, the calculated Rayleigh numbers can easily go beyond 10^6 for the PCM such as paraffin wax and fatty acid, and even exceed 10^8 for some HX settings, which causes the numerical models to be unstable and inaccurate. Therefore, the developed model was further improved for high Rayleigh numbers in this dissertation by adding the ex-

plicit terms to the source term in moment space to eliminate the thermal flow errors at high Rayleigh numbers in LBM.

In general, the proposed treatment embedded in the MRT scheme forms a novel thermal MRT-LBM, which is capable of solving the thermal flow and phase change stably and accurately under strong convection.

B.2. Improved the LBM model with parallel scheme (Section 4.6 and Section 5.3)

Owing to the explicit streaming process and local collision process, LBM is ideal for parallel computing. And this is also one of the key features that makes the LBM competitive compared with the conventional CFD. Specifically, for the simulation of PCM HX, the developed lattice Boltzmann model with the parallel scheme can perform numerous parametric studies of the PCM HX in a time-efficient way, which benefits the design and analysis of the PCM HX.

In this dissertation, the parallel scheme was applied to further improve the enthalpy-based DDF-MRT model. The performance of the developed parallel lattice Boltzmann model was tested through the scaling analyses of a porous PCM melting simulation conducted on HPC resources. The parallel model could either be operated both in Windows and Linux systems. Given the fact that the detailed analysis of the parallel scheme in solid-liquid LBM is limited in the literature, the results of the scaling analyses in this dissertation can be served as the reference for choosing

the operating cores for the parallel simulation of the PCM HX.

C. Parametric studies of the PCM HX using the new model, providing insights into the physical mechanisms and the basis of the PCM HX design

C.1. Quantitatively evaluated the natural convection effect on PCM melting (Section 6.1)

Unlike the solidification cases where natural convection effect is always limited, PCM melting on contrary can be affected or even dominated by convection heat transfer. Consequently, quantitatively evaluation of natural convection effect on PCM melting is essential to the design and analysis of the PCM HX. Such a kind of evaluation is limited in the literature since it requires many cases conducted numerically concerning different HX geometries and Rayleigh numbers, which is very consuming in terms of time and computational costs. Owing to the developed parallel DDF-MRT LBM, this parametric study can be performed efficiently.

Generally, the parametric study in this dissertation evaluated thermal performance of the cylindrical PCM HX with various aspect ratios and Rayleigh numbers. The results provided the quantified melting acceleration rates of the PCM HX at various aspect ratios and Rayleigh numbers. And threshold Rayleigh numbers (Ra_{dc}) were proposed to serve as references for the design of the cylindrical HX at various aspect ratios.

C.2. Evaluated the enhanced PCM HX and analyzed the uneven temperature distribution issues (Section 6.2 and Section 6.3)

From the parametric studies in this dissertation, it can be observed that the uneven temperature distributions caused by convection heat transfer have a negative effect on thermal performance of the PCM HX. For pure PCM melting in a straight cylinder, the heat transfer enhanced by convection should be strong enough to offset its negative effect, which means the Rayleigh number that characterizes PCM melting should be above a certain value. And for common cylindrical HX under various aspect ratios, the provided Ra_{dc} can be served as the references, above which the PCM melting is guaranteed to be enhanced by convection heat transfer in the given PCM HX.

The PCM HX enhancements such as the porous media and the modified geometry of the HX were also evaluated in this dissertation. The results of porous PCM melting demonstrated the positive effect of adding porous media on heat transfer over the entire PCM domain, and the negative effect of porous media on convective flow in the liquid zone. And the results of the modified cylindrical HX indicated a significant improvement in the thermal performance of the PCM HX as it can address the uneven temperature distribution issues by taking the advantage of the positive effect of convection on heat transfer.

8.2 List of Related Publications

Based on the work in this dissertation, one conference paper and one journal paper were published, and two more journal papers are under development. They are listed as follows:

- Peer-Reviewed Conference Papers
  - Chen, D., Riaz, A. and Aute, V.C., and Radermacher, R., "A Lattice Boltzmann Model for Phase Change Material (PCM) Melting with Porous Media in Heat Exchanger" (2021). International Refrigeration and Air Conditioning Conference
- Journal Papers
  - Chen, D., Riaz, A., Aute, V.C. and Radermacher, R., 2022. A solid–liquid model based on lattice Boltzmann method for phase change material melting with porous media in cylindrical heat exchangers.Applied Thermal Engineering, p.118080.
  - Chen, D., Riaz, A., Aute, V.C. and Radermacher, R., Numerical analysis of PCM melting in cylindrical HX using a novel improved enthalpy-based LBM. (manuscript completed)
  - Chen, D., Riaz, A., Aute, V.C. and Radermacher, R., Numerical analysis of porous PCM melting with circular fins in cylindrical HX using a novel improved enthalpy-based LBM. (expected)

Bibliography

[1] S Pratap Vanka. Block-implicit multigrid solution of navier-stokes equations in primitive variables. *Journal of Computational Physics*, 65(1):138–158, 1986.

[2] Yiyuan Qiao, Anne Mallow, Jan Muehlbauer, Yunho Hwang, Jiazhen Ling, Vikrant Chandramohan Aute, Reinhard Radermacher, and Kyle Gluesenkamp. Experimental study on portable air-conditioning system with enhanced pcm condenser. 2018.

[3] Moritz Faden, Andreas König-Haagen, Stephan Höhlein, and Dieter Brüggemann. An implicit algorithm for melting and settling of phase change material inside macrocapsules. *International Journal of Heat and Mass Transfer*, 117(November):757–767, 2018.

[4] Martin Longeon, Adèle Soupart, Jean François Fourmigué, Arnaud Bruch, and Philippe Marty. Experimental and numerical study of annular PCM storage in the presence of natural convection. *Applied Energy*, 112:175–184, 2013.

[5] Soroush Ebadi, Manar Al-Jethelah, Syeda Humaira Tasnim, and Shohel Mahmud. An investigation of the melting process of rt-35 filled circular thermal energy storage system. *Open Physics*, 16(1):574–580, 2018.

[6] J. Yang, J. Muehlbauer, D. Bacellar, J. Ling, V. Aute, and Y. Hwang. Experimental investigation of a phase change material charged finned-tube heat exchanger. *19th Int. Refrig. Air Cond. Conf. Purdue[Manuscripted Accepted]*.

[7] W. Youssef, Y. T. Ge, and S. A. Tassou. CFD modelling development and experimental validation of a phase change material (PCM) heat exchanger with spiral-wired tubes. *Energy Conversion and Management*, 157(October 2017):498–510, 2018.

[8] Renkun Dai, Wei Li, Javad Mostaghimi, Qiuwang Wang, and Min Zeng. On the optimal heat source location of partially heated energy storage process using the newly developed simplified enthalpy based lattice Boltzmann method. *Applied Energy*, 275(May):115387, 2020.

[9] Ya Ling He, Qing Liu, Qing Li, and Wen Quan Tao. Lattice Boltzmann methods for single-phase and solid-liquid phase-change heat transfer in porous media: A review. *International Journal of Heat and Mass Transfer*, 129:160–197, 2019.

[10] Baojie Zhu, Yifei Guan, and Jian Wu. Two-relaxation time lattice Boltzmann models for the ion transport equation in electrohydrodynamic flow: D2Q5 vs D2Q9 and D3Q7 vs D3Q27. *Physics of Fluids*, 33(4), 2021.

[11] C Beckermann and R Viskanta. Natural convection solid/liquid phase change in porous media. *International journal of heat and mass transfer*, 31(1):35–46, 1988.

[12] V. Prasad and F. A. Kulacki. Natural Convection in Porous Media Bounded by Short Concentric Vertical Cylinders. *Journal of Heat Transfer*, 107(1):147–154, 02 1985.

[13] Fang Wang, Jean Damascene Harindintwali, Zhizhang Yuan, Min Wang, Faming Wang, Sheng Li, Zhigang Yin, Lei Huang, Yuhao Fu, Lei Li, Scott X. Chang, Linjuan Zhang, Jörg Rinklebe, Zuoqiang Yuan, Qinggong Zhu, Leilei Xiang, Daniel C.W. Tsang, Liang Xu, Xin Jiang, Jihua Liu, Ning Wei, Matthias Kästner, Yang Zou, Yong Sik Ok, Jianlin Shen, Dailiang Peng, Wei Zhang, Damià Barceló, Yongjin Zhou, Zhaohai Bai, Boqiang Li, Bin Zhang, Ke Wei, Hujun Cao, Zhiliang Tan, Liu bin Zhao, Xiao He, Jinxing Zheng, Nanthi Bolan, Xiaohong Liu, Changping Huang, Sabine Dietmann, Ming Luo, Nannan Sun, Jirui Gong, Yulie Gong, Ferdi Brahushi, Tangtang Zhang, Cunde Xiao, Xianfeng Li, Wenfu Chen, Nianzhi Jiao, Johannes Lehmann, Yong-Guan Zhu, Hongguang Jin, Andreas Schäffer, James M. Tiedje, and Jing M. Chen. Technologies and perspectives for achieving carbon neutrality. *The Innovation*, 2(4):100180, 2021.

[14] Paris agreement, Dec. 2015. UNTC XXVII 7.d.

[15] Jing M. Chen. Carbon neutrality: Toward a sustainable future. *The Innovation*, 2(3):100127, 2021.

[16] Federal sustainability plan, Dec. 2021. The Office of the Federal Chief Sustainability Officer (CSO).

[17] Zhu Liu, Zhu Deng, Gang He, Hailin Wang, Xian Zhang, Jiang Lin, Ye Qi, and Xi Liang. Challenges and opportunities for carbon neutrality in China. *Nature Reviews Earth and Environment*, 3(2):141–155, 2022.

[18] Grégory Claeys, Simone Tagliapietra, Georg Zachmann, et al. *How to make the European Green Deal work*. JSTOR, 2019.

[19] Gang Li and Xuefei Zheng. Thermal energy storage system integration forms for a sustainable future. *Renewable and Sustainable Energy Reviews*, 62:736–757, 2016.

[20] Abdelrahman Azzuni and Christian Breyer. Energy security and energy storage technologies. *Energy Procedia*, 155:237–258, 2018.

[21] Vineet Veer Tyagi and D. Buddhi. PCM thermal storage in buildings: A state of art. *Renewable and Sustainable Energy Reviews*, 11(6):1146–1166, 2007.

[22] Jisoo Jeon, Jung Hun Lee, Jungki Seo, Su Gwang Jeong, and Sumin Kim. Application of PCM thermal energy storage system to reduce building energy consumption. *Journal of Thermal Analysis and Calorimetry*, 111(1):279–288, 2013.

[23] Sarada Kuravi, Jamie Trahan, D. Yogi Goswami, Muhammad M. Rahman, and Elias K. Stefanakos. Thermal energy storage technologies and systems for concentrating solar power plants. *Progress in Energy and Combustion Science*, 39(4):285–319, 2013.

[24] M. H. Mahfuz, M. R. Anisur, M. A. Kibria, R. Saidur, and I. H.S.C. Metselaar. Performance investigation of thermal energy storage system with Phase Change Material (PCM) for solar water heating application. *International Communications in Heat and Mass Transfer*, 57:132–139, 2014.

[25] Muriel Iten, Shuli Liu, and Ashish Shukla. A review on the air-PCM-TES application for free cooling and heating in the buildings. *Renewable and Sustainable Energy Reviews*, 61:175–186, 2016.

[26] Hussein Akeiber, Payam Nejat, Muhd Zaimi Abd Majid, Mazlan A. Wahid, Fatemeh Jomehzadeh, Iman Zeynali Famileh, John Kaiser Calautit, Ben Richard Hughes, and Sheikh Ahmad Zaki. A review on phase change material (PCM) for sustainable passive cooling in building envelopes. *Renewable and Sustainable Energy Reviews*, 60:1470–1497, 2016.

[27] Ying-Che Weng, Hung-Pin Cho, Chih-Chung Chang, and Sih-Li Chen. Heat pipe with pcm for electronic cooling. *Applied energy*, 88(5):1825–1833, 2011.

[28] Jungwook Shon, Hyungik Kim, and Kihyung Lee. Improved heat storage rate for an automobile coolant waste heat recovery system using phase-change material in a fin-tube heat exchanger. *Applied Energy*, 113:680–689, 2014.

[29] Akanksha Mishra, A Shukla, and Atul Sharma. Latent heat storage through phase change materials. *Resonance*, 20(6):532–541, 2015.

[30] N. H.S. Tay, F. Bruno, and M. Belusko. Experimental validation of a CFD model for tubes in a phase change thermal energy storage system. *International Journal of Heat and Mass Transfer*, 55(4):574–585, 2012.

[31] Adèle Caron-Soupart, Jean François Fourmigué, Philippe Marty, and Raphaël Couturier. Performance analysis of thermal energy storage systems using phase change material. *Applied Thermal Engineering*, 98:1286–1296, 2016.

[32] S. Bakhshipour, M. S. Valipour, and Y. Pahamli. Analyse paramétrique de réfrigérateurs domestiques utilisant un échangeur de chaleur à matériau à changement de phase. *International Journal of Refrigeration*, 83:1–13, 2017.

[33] Yiyuan Qiao, Yilin Du, Jan Muehlbauer, Yunho Hwang, and Reinhard Radermacher. Experimental study of enhanced PCM exchangers applied in a thermal energy storage system for personal cooling. *International Journal of Refrigeration*, 102:22–34, 2019.

[34] Yiyuan Qiao, Tao Cao, Jan Muehlbauer, Yunho Hwang, and Reinhard Radermacher. Experimental study of a personal cooling system integrated with phase change material. *Applied Thermal Engineering*, 170(October 2019):115026, 2020.

[35] S. F. Hosseinizadeh, F. L. Tan, and S. M. Moosania. Experimental and numerical studies on performance of PCM-based heat sink with different configurations of internal fins. *Applied Thermal Engineering*, 31(17-18):3827–3838, 2011.

[36] A. Felix Regin, S. C. Solanki, and J. S. Saini. Heat transfer characteristics of thermal energy storage system using PCM capsules: A review. *Renewable and Sustainable Energy Reviews*, 12(9):2438–2458, 2008.

[37] Jahar Sarkar and Souvik Bhattacharyya. Application of graphene and graphene-based materials in clean energy-related devices Minghui. *Archives of Thermodynamics*, 33(4):23–40, 2012.

[38] Huanpei Zheng, Changhong Wang, Qingming Liu, Zhongxuan Tian, and Xianbo Fan. Thermal performance of copper foam/paraffin composite phase change material. *Energy Conversion and Management*, 157(September 2017):372–381, 2018.

[39] Refat Al-Shannaq, Brent Young, and Mohammed Farid. Cold energy storage in a packed bed of novel graphite/PCM composite spheres. *Energy*, 171:296–305, 2019.

[40] Francis Agyenim, Neil Hewitt, Philip Eames, and Mervyn Smyth. A review of materials, heat transfer and phase change problem formulation for latent heat thermal energy storage systems (lhtess). *Renewable and sustainable energy reviews*, 14(2):615–628, 2010.

[41] E. Osterman, V. V. Tyagi, V. Butala, N. A. Rahim, and U. Stritih. Review of PCM based cooling technologies for buildings. *Energy and Buildings*, 49:37–49, 2012.

[42] Q. Li, K. H. Luo, Q. J. Kang, Y. L. He, Q. Chen, and Q. Liu. Lattice Boltzmann methods for multiphase flow and phase-change heat transfer. *Progress in Energy and Combustion Science*, 52:62–105, 2016.

[43] Qing Liu, Xiang Bo Feng, Ya Ling He, Cai Wu Lu, and Qing Hua Gu. Multiple-relaxation-time lattice Boltzmann model for simulating axisymmetric thermal flows in porous media. *International Journal of Heat and Mass Transfer*, 137:1301–1311, 2019.

[44] Abduljalil A. Al-abidi, Sohif Bin Mat, K. Sopian, M.Y. Sulaiman, and Abdulrahman Th. Mohammed. Cfd applications for latent heat thermal energy storage: a review. *Renewable and Sustainable Energy Reviews*, 20:353–363, 2013.

[45] W. Miller, I. Rasin, and S. Succi. Lattice boltzmann phase-field modelling of binary-alloy solidification. *Physica A: Statistical Mechanics and its Applications*, 362(1):78–83, 2006. Discrete Simulation of Fluid Dynamics.

[46] Roberto Rojas, Tomohiro Takaki, and Munekazu Ohno. A phase-field-lattice boltzmann method for modeling motion and growth of a dendrite for binary alloy solidification in the presence of melt convection. *Journal of Computational Physics*, 298:29–40, 2015.

[47] Rongzong Huang, Huiying Wu, and Ping Cheng. A new lattice Boltzmann model for solid-liquid phase change. *International Journal of Heat and Mass Transfer*, 59(1):295–301, 2013.

[48] Dongyan Gao, Zhenqian Chen, Dongliang Zhang, and Linghai Chen. Lattice Boltzmann modeling of melting of phase change materials in porous media with conducting fins. *Applied Thermal Engineering*, 118:315–327, 2017.

[49] Dong Li, Qinlong Ren, Zi Xiang Tong, and Ya Ling He. Lattice Boltzmann models for axisymmetric solid–liquid phase change. *International Journal of Heat and Mass Transfer*, 112:795–804, 2017.

[50] Rongzong Huang and Huiying Wu. Total enthalpy-based lattice Boltzmann method with adaptive mesh refinement for solid-liquid phase change. *Journal of Computational Physics*, 315:65–83, 2016.

[51] Qing Liu and Ya Ling He. Double multiple-relaxation-time lattice Boltzmann model for solid-liquid phase change with natural convection in porous media. *Physica A: Statistical Mechanics and its Applications*, 438:94–106, 2015.

[52] Qinlong Ren, Fanlong Meng, and Penghua Guo. A comparative study of PCM melting process in a heat pipe-assisted LHTES unit enhanced with nanoparticles and metal foams by immersed boundary-lattice Boltzmann method at pore-scale. *International Journal of Heat and Mass Transfer*, 121:1214–1228, 2018.

[53] Zuo Wang, Yan Liu, and Jiazhong Zhang. Double MRT lattice Boltzmann model for axisymmetric convective flow in porous media. *International Journal of Heat and Mass Transfer*, 112:810–813, 2017.

[54] Carolin Körner, Thomas Pohl, Ulrich Rüde, Nils Thürey, and Thomas Zeiser. Parallel lattice Boltzmann methods for CFD applications. *Lecture Notes in Computational Science and Engineering*, 51:440–466, 2006.

[55] C. Beckermann and R. Viskanta. Natural convection solid/liquid phase change in porous media. *International Journal of Heat and Mass Transfer*, 31(1):35–46, 1988.

[56] Zhaoli Guo and T. S. Zhao. Lattice Boltzmann model for incompressible flows through porous media. *Physical Review E - Statistical Physics, Plasmas, Fluids, and Related Interdisciplinary Topics*, 66(3):1–9, 2002.

[57] Xiao Hu Yang, Jia Xi Bai, Hong Bin Yan, Jiu Jie Kuang, Tian Jian Lu, and Tongbeum Kim. An Analytical Unit Cell Model for the Effective Thermal Conductivity of High Porosity Open-Cell Metal Foams. *Transport in Porous Media*, 102(3):403–426, 2014.

[58] J Buschle, W D Steinmann, and R Tamme. Analysis of steam storage systems using Modelica. *Modelica 2006, September 4th – 5th*, pages 235–242, 2006.

[59] Rongzong Huang and Huiying Wu. Phase interface effects in the total enthalpy-based lattice Boltzmann model for solid-liquid phase change. *Journal of Computational Physics*, 294:346–362, 2015.

[60] Zhenhua Chai, Baochang Shi, and Zhaoli Guo. A multiple-relaxation-time lattice boltzmann model for general nonlinear anisotropic convection–diffusion equations. *Journal of Scientific Computing*, 69(1):355–390, 2016.

[61] Prabhu Lal Bhatnagar, Eugene P Gross, and Max Krook. A model for collision processes in gases. i. small amplitude processes in charged and neutral one-component systems. *Physical review*, 94(3):511, 1954.

[62] Shiyi Chen, Hudong Chen, Daniel Martnez, and William Matthaeus. Lattice boltzmann model for simulation of magnetohydrodynamics. *Physical Review Letters*, 67(27):3776, 1991.

[63] YH Qian. Simulating thermohydrodynamics with lattice bgk models. *Journal of scientific computing*, 8(3):231–242, 1993.

[64] A critical evaluation of force term in lattice Boltzmann method, natural convection problem. *International Journal of Heat and Mass Transfer*, 53(5-6):990–996, 2010.

[65] Xiaoyi He, Xiaowen Shan, and Gary D Doolen. Discrete boltzmann equation model for nonideal gases. *Physical Review E*, 57(1):R13, 1998.

[66] Zhaoli Guo, Chuguang Zheng, and Baochang Shi. Discrete lattice effects on the forcing term in the lattice boltzmann method. *Physical review E*, 65(4):046308, 2002.

[67] Pierre Lallemand and Li-Shi Luo. Theory of the lattice boltzmann method: Dispersion, dissipation, isotropy, galilean invariance, and stability. *Phys. Rev. E*, 61:6546–6562, Jun 2000.

[68] Dominique d'Humières. Generalized lattice-boltzmann equations. *Rarefied gas dynamics*, 1992.

[69] Michael E. McCracken and John Abraham. Multiple-relaxation-time lattice-boltzmann model for multiphase flow. *Phys. Rev. E*, 71:036701, Mar 2005.

[70] He Xiaoyi and Luo Li-Shi. Lattice Boltzmann Model for the Incompressible Navier-Stokes Equation. *Journal of Statistical Physics*, 884(3):927–944, 1997.

[71] Qing Liu, Ya Ling He, Dong Li, and Qing Li. Non-orthogonal multiple-relaxation-time lattice Boltzmann method for incompressible thermal flows. *International Journal of Heat and Mass Transfer*, 102:1334–1344, 2016.

[72] Q. Li, Y. L. He, G. H. Tang, and W. Q. Tao. Improved axisymmetric lattice boltzmann scheme. *Phys. Rev. E*, 81:056707, May 2010.

[73] Liang Wang, Zhaoli Guo, and Chuguang Zheng. Multi-relaxation-time lattice boltzmann model for axisymmetric flows. *Computers Fluids*, 39(9):1542–1548, 2010.

[74] Zhaoli Guo, Haifeng Han, Baochang Shi, and Chuguang Zheng. Theory of the lattice boltzmann equation: Lattice boltzmann model for axisymmetric flows. *Phys. Rev. E*, 79:046708, Apr 2009.

[75] Zhaoli Guo and TS Zhao. Lattice boltzmann model for incompressible flows through porous media. *Physical review E*, 66(3):036304, 2002.

[76] Pierre Lallemand and Li-Shi Luo. Hybrid finite-difference thermal lattice boltzmann equation. *International Journal of Modern Physics B*, 17(01n02):41–47, 2003.

[77] Olga Filippova and Dieter Hänel. A novel lattice bgk approach for low mach number combustion. *Journal of Computational Physics*, 158(2):139–160, 2000.

[78] Y Peng, C Shu, and YT Chew. Simplified thermal lattice boltzmann model for incompressible thermal flows. *Physical Review E*, 68(2):026701, 2003.

[79] Zhaoli Guo, Baochang Shi, and Chuguang Zheng. A coupled lattice bgk model for the boussinesq equations. *International Journal for Numerical Methods in Fluids*, 39(4):325–342, 2002.

[80] Dong Li, Zi Xiang Tong, Qinlong Ren, Ya Ling He, and Wen Quan Tao. Three–dimensional lattice Boltzmann models for solid–liquid phase change. *International Journal of Heat and Mass Transfer*, 115:1334–1347, 2017.

[81] Dominique d'Humières. Multiple–relaxation–time lattice boltzmann models in three dimensions. *Philosophical Transactions of the Royal Society of London. Series A: Mathematical, Physical and Engineering Sciences*, 360(1792):437–451, 2002.

[82] Kannan N Premnath and John Abraham. Three-dimensional multi-relaxation time (mrt) lattice-boltzmann models for multiphase flow. *Journal of Computational Physics*, 224(2):539–559, 2007.

[83] Hiroaki Yoshida and Makoto Nagaoka. Multiple-relaxation-time lattice boltzmann model for the convection and anisotropic diffusion equation. *Journal of Computational Physics*, 229(20):7774–7795, 2010.

[84] Bastien Chopard, Jean L Falcone, and Jonas Latt. The lattice boltzmann advection-diffusion model revisited. *The European Physical Journal Special Topics*, 171(1):245–249, 2009.

[85] Donald P Ziegler. Boundary conditions for lattice boltzmann simulations. *Journal of statistical physics*, 71(5):1171–1177, 1993.

[86] Shiyi Chen, Daniel Martinez, and Renwei Mei. On boundary conditions in lattice boltzmann methods. *Physics of fluids*, 8(9):2527–2536, 1996.

[87] Kannan N. Premnath and Sanjoy Banerjee. Incorporating forcing terms in cascaded lattice Boltzmann approach by method of central moments. *Physical Review E - Statistical, Nonlinear, and Soft Matter Physics*, 80(3), 2009.

[88] Sydney Chapman, Thomas George Cowling, and David Burnett. *The mathematical theory of non-uniform gases: an account of the kinetic theory of viscosity, thermal conduction and diffusion in gases*. Cambridge university press, 1990.

[89] Like Li, Renwei Mei, and James F. Klausner. Multiple-relaxation-time lattice boltzmann model for the axisymmetric convection diffusion equation. *International Journal of Heat and Mass Transfer*, 67:338 – 351, 2013.

[90] Zuo Wang, Wenfan Zhang, and Jiazhong Zhang. Lattice boltzmann simulations of axisymmetric natural convection with anisotropic thermal diffusion. *International Journal of Heat and Mass Transfer*, 101:1304 – 1315, 2016.

[91] Matthieu Martinelli, Fabrice Bentivoglio, Adèle Caron-Soupart, Raphaël Couturier, Jean François Fourmigue, and Philippe Marty. Experimental study of a phase change thermal energy storage with copper foam. *Applied Thermal Engineering*, 101:247–261, 2016.

[92] Mehdi Esapour, Arash Hamzehnezhad, A Ali Rabienataj Darzi, and Mahmoud Jourabian. Melting and solidification of pcm embedded in porous metal foam in horizontal multi-tube heat storage system. *Energy conversion and management*, 171:398–410, 2018.

[93] Mustafa S Mahdi, Hameed B Mahood, Jasim M Mahdi, Anees A Khadom, and Alasdair N Campbell. Improved pcm melting in a thermal energy storage system of double-pipe helical-coil tube. *Energy Conversion and Management*, 203:112238, 2020.

[94] AC Mueller and JP Chiou. Review of various types of flow maldistribution in heat exchangers. *Heat transfer engineering*, 9(2):36–50, 1988.

[95] Zhe Zhang and YanZhong Li. Cfd simulation on inlet configuration of plate-fin heat exchangers. *Cryogenics*, 43(12):673–678, 2003.

[96] Frédéric Poggi, André Bontemps, Hélène Macchi-Tejeda, Alain Maréchal, and Denis Leducq. Experimental and numerical study of the distribution of a single-phase flow in a small channel heat exchanger. 2009.

[97] Long Huang, Moon Soo Lee, Khaled Saleh, Vikrant Aute, and Reinhard Radermacher. A computational fluid dynamics and effectiveness-NTU based co-simulation approach for flow mal-distribution analysis in microchannel heat exchanger headers. *Applied Thermal Engineering*, 65(1-2):447–457, 2014.

[98] Andrew K Gunstensen, Daniel H Rothman, Stéphane Zaleski, and Gianluigi Zanetti. Lattice boltzmann model of immiscible fluids. *Physical Review A*, 43(8):4320, 1991.

[99] Xiaowen Shan and Hudong Chen. Lattice boltzmann model for simulating flows with multiple phases and components. *Physical review E*, 47(3):1815, 1993.

[100] Michael R Swift, WR Osborn, and JM Yeomans. Lattice boltzmann simulation of nonideal fluids. *Physical review letters*, 75(5):830, 1995.

[101] Xiaoyi He, Shiyi Chen, and Raoyang Zhang. A lattice boltzmann scheme for incompressible multiphase flow and its application in simulation of rayleigh–taylor instability. *Journal of computational physics*, 152(2):642–663, 1999.

[102] Q. Li, K. H. Luo, Y. J. Gao, and Y. L. He. Additional interfacial force in lattice boltzmann models for incompressible multiphase flows. *Phys. Rev. E*, 85:026704, Feb 2012.

[103] T Inamuro, Tajima Ogata, S Tajima, and N Konishi. A lattice boltzmann method for incompressible two-phase flows with large density differences. *Journal of Computational physics*, 198(2):628–644, 2004.

[104] Yan Wang, Chang Shu, HB Huang, and CJ Teo. Multiphase lattice boltzmann flux solver for incompressible multiphase flows with large density ratio. *Journal of Computational Physics*, 280:404–423, 2015.

[105] Raoyang Zhang and Hudong Chen. Lattice boltzmann method for simulations of liquid-vapor thermal flows. *Phys. Rev. E*, 67:066711, Jun 2003.

[106] Gabor Hazi and Attila Markus. On the bubble departure diameter and release frequency based on numerical simulation results. *International Journal of Heat and Mass Transfer*, 52(5-6):1472–1480, 2009.

[107] Attila Márkus and Gábor Házi. Simulation of evaporation by an extension of the pseudopotential lattice boltzmann method: A quantitative analysis. *Phys. Rev. E*, 83:046705, Apr 2011.

[108] Li Chen, Qinjun Kang, Yutong Mu, Ya-Ling He, and Wen-Quan Tao. A critical review of the pseudopotential multiphase lattice boltzmann model: Methods and applications. *International journal of heat and mass transfer*, 76:210–236, 2014.

[109] RH Perry and DW Green. Perry's chemical engineers' handbook, 7th intl. ed, 1998.

[110] Xiaoming Zhao, Wenhao Duan, Xiaoyang Zeng, and Yu Liu. Measurements of surface tension of r1234yf and r1234ze (e). *Journal of Chemical & Engineering Data*, 63(1):21–26, 2018.